Migrating Target Detection in Wideband Radars

Important note
To cite this publication, please use the final published version (if applicable).
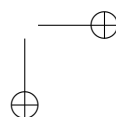Please check the document version above.

Migrating Target Detection in Wideband Radars
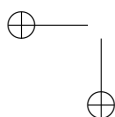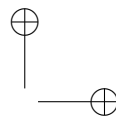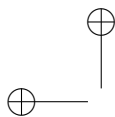
Migrating Target Detection in Wideband Radars

Dissertation

for the purpose of obtaining the degree of doctor
at Delft University of Technology
by the authority of the Rector Magnificus, Prof.dr.ir. T.H.J.J. van der Hagen,
chair of the Board for Doctorates,
to be defended publicly on
Friday, 21 June 2019 at 10:00 o'clock

by

Nikita PETROV

Engineer (Radio-Electronic Systems),
Baltic State Technical University "Voenmeh" named after D.F.Ustinov, Russia
born in Gatchina, Russia

This dissertation has been approved by the promotors.

Composition of the doctoral committee:

Rector Magnificus,   chairperson
Prof.ir. F. Le Chevalier,   Delft University of Technology, promotor
Prof.dr. A.G. Yarovoy,   Delft University of Technology, promotor

Independent members:
Prof.dr. S. Bidon   Institut Supérieur de l'Aéronautique et de l'Espace, France
Prof.dr. M. Greco   Universitá di Pisa, Italy
Prof.dr. C.S. Vaucher   Delft University of Technology / NXP Semiconductors
Prof.dr.ir. G.J.T. Leus   Delft University of Technology
Dr.ir. J.N. Driessen   Delft University of Technology

Author e-mail: Nekit1003@gmail.com
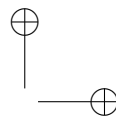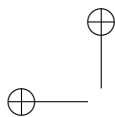
To my family and friends

Contents

Summary

Modern surveillance radars are designed to detect moving targets of interest in an adverse environment, which can encompass strong unwanted reflections from ground or sea surface, clouds, precipitation, etc. Detection of weak and small moving targets in environmental clutter remains, however, a challenging task for the existing radar systems.

One of the main directions for modern radar performance improvement is the application of wideband high-resolution waveforms, which provide detailed range information of objects in the observed scene. Together with such inherent advantages of wideband waveforms as multi-path separation, clutter reduction and improved target classification, additional benefits can be obtained by exploiting target range migration (range walk), essential for fast moving targets in the high-resolution mode.

This thesis aims at the development of novel signal processing techniques for migrating target detection in wideband radars. It involves both resolving range-velocity ambiguities and improvement in target discrimination from ground clutter by accounting for target range migration.

It is demonstrated that wideband radars can resolve range-velocity ambiguity by transmitting a single long pulse burst with low pulse repetition frequency (PRF) and exploring target range walk phenomena during the burst. The ambiguity function of such waveform still has strong residuals at the locations of ambiguities, called ambiguous sidelobes, which have to be considered in the processing of wideband data.

The presence of ground clutter in the observation scene has a detrimental effect on the wideband radar performance. The impact of the clutter Doppler spectrum and waveform parameters on target detection at clutter ambiguities has been investigated. The improvement over the conventional waveform is demonstrated for narrow clutter Doppler spectrum; in the presence of clutter with a wide Doppler spectrum, the conventional staggered-PRF waveform is preferable. Performance degradation at ambiguous-to-clutter velocities is validated on the real data sets.

Modern high-resolution parametric-free spectrum estimators IAA (Iterative Adaptive Approach) and SPICE (Semi-Parametric Iterative Covariance-based Estimator)

are proposed for the reconstruction of the observed scene from wideband radar measurements with no velocity ambiguities. These algorithms demonstrate significant improvement in rejection of ambiguous sidelobes over the conventional techniques. For clutter-limited case, the covariance-aware SPICE is introduced with improved capability to discriminate targets from clutter. The advantages of the proposed methods are demonstrated in numerical simulations and real data processing.

The ambiguous sidelobes can cause severe problems for detection of multiple targets located at similar ranges. A dedicated detector for a dense target scenario has been introduced. It can detect multiple closely spaced targets and mitigate false detections due to their ambiguous sidelobes, holding false alarm probability at the required level. The improvement over conventional processing is demonstrated.

Special attention is then devoted to clutter suppression in the high range resolution mode. In meter or sub-meter range resolution, the observed ground clutter, modeled by a compound-Gaussian process, may have significant fluctuations over the range interval, elapsed by the target. An advanced detector for range-migrating targets in compound-Gaussian clutter is developed. It performs two-dimensional clutter filtering in Doppler frequency and in the range and benefits from clutter spatial diversity, obtained for a target passing over different patches of clutter. A significant improvement in the detection of fast moving targets in spiky clutter is achieved in comparison to the existing methods. The attained gain depends on clutter characteristics and target velocity: fast moving targets are easier to detect than slow ones with equal signal-to-clutter ratio. The generalized approach for detection of range-extended migrating targets is provided.

The performed research provides some fundamental insight for implementation of new radar architectures with the utilization of wideband waveforms.

Samenvatting

Moderne surveillance radars zijn ontworpen om gewenste bewegende doelen te detecteren in een lastige omgeving die bestaat uit sterke ongewenste reflecties van land of zee, wolken, neerslag, enzovoort. Het detecteren van kleine zwakke bewegende objecten in omgevingsclutter blijft nog steeds een uitdagende taak voor conventionele radar systemen

Een van de belangrijke richtingen voor de verbetering van moderne radar, is de toepassing van breedbandige, hoge resolutie golfvormen, welke een gedetailleerde range informatie van het object verschaffen op de plaats van observatie. Tezamen met de inherente voordelen van breedbandige golfvormen, zoals multipad separatie, clutter reductie en verbeterde doelsdetectie, aanvullende voordelen kunnen worden verkregen door het benutten van range migratie, die essentieel is voor snel bewegende doelen in de hoge resolutie mode.

Dit proefschrift focusseert op de ontwikkeling van nieuwe signaalverwerkingstechnieken ten behoeve van het detecteren van doelen in breedbandige radars. Aandacht wordt voornamelijk gegeven aan het resolveren van afstand-snelheid ambiguiteiten en het verbeteren van doelsdiscriminatie ten opzichte van grond clutter.

Aangetoond wordt dat breedbandige radars een lage pulsherhalingsfrequentie n burst pulse kunnen gebruiken, zodanig dat het fenomeen range-walk gedurende de hele burst significant genoeg is om de ambiguiteit in snelheid op te lossen. De ambiguiteitsfunctie van dergelijke golfvormen hebben nog steeds sterke residuen op de plaats van de ambiguiteit, genaamd ambigue zijlobben, die moeten worden meegenomen in de verwerking van de breedband data.

De aanwezigheid van grond clutter in het observatie beeld heeft een nadelig effect op de werkzaamheid van een breedband radar. De invloed van het clutter Doppler spectrum en de parameters van de golfvorm op de bepaling van het doel met clutter ambiguiteit is onderzocht. De verbetering met betrekking tot de conventionele golfvorm wordt aangetoond voor smallbandige Doppler clutter spectrum; in de aanwezigheid van clutter met een breedbandig Doppler spectrum verdient de conventionele staggerde-PRF golfvorm de voorkeur. De vermindering van de prestatie voor

ambigue in relatie tot clutter snelheden wordt gevalideerd aan de hand van gemeten data.

Moderne hoge resolutie parameter-vrije spectrum schatters IAA (Iterative Adaptive Approach) and SPICE (Semi-Parametric Iterative Covariance-based Estimator) worden voorgesteld voor het verwijderen van ambigue residuen van de aanwezige doelen. Deze algorithmen laten een verbeterde prestatie zien met betrekking tot de onderdrukking van ambigue zijlobben in verhouding met conventionele technieken. In het geval van beperkte clutter wordt covariantie gevoelige SPICE geintroduceerd met een verbeterde mogelijkheid om doelen van clutter te onderscheiden. De voordelen van de voorgestelde methoden worden aangetoond met numerieke simulaties en met gemeten data verwerking.

De ambigue zijlobben kunnen enorme problemen veroorzaken bij de detectie van meerdere doelen die gelocaliseerd zijn op gelijke afstand van het punt van observatie. Een aangepaste detector wordt geintroduceerd voor omstandigheden met dicht op elkaar geplaatste doelen. Deze detector kan meerdere dicht op elkaar geplaatste doelen onderscheiden en onderdrukt valse waarnemingen ten gevolge van ambigue zijlobben van het doel, waarbij de vals alarm waarschijnlijkheid op het gewenste niveau wordt gehouden. De verbetering met betrekking tot conventionele verwerkingsmethoden wordt aangetoond.

Speciale aandacht wordt besteed aan de clutter onderdrukking in hoge range resolutie mode. In meter of sub-meter range resolutie, de waargenomen grond clutter, die gemodelleerd wordt door een samengesteld-Gaussisch proces, kan significante fluctuaties hebben over het range interval, dat is afgelegd door het doel. Een geavanceerde detector voor range-migrerende doelen onder invloed van samengestelde-Gaussische clutter is ontwikkeld. Deze detector voert twee-dimensionale clutter filtering uit met betrekking tot de Doppler frequentie en de range en profiteert van de ruimtelijke clutter diversiteit, die verkregen is door een doel dat over verschillend stukjes clutter is gepasseerd. Een significante verbetering met betrekking tot de detectie van snel bewegende doelen onder invloed van naaldvormige clutter is bereikt in vergelijking met de bestaande methoden. De bereikte winst hangt af van de karakteristieken van de clutter en de snelheid van het doel: snel bewegende doelen zijn makkelijker te detecteren dan langzaam bewegende, bij gelijkblijvende signaal-clutter verhouding. De algemene benadering met betrekking tot detectie van doelen met uitgebreide range migratie wordt voorgesteld.

Het uitgevoerde onderzoek verschaft enkele basis inzichten voor de implementatie van nieuwe radar ontwerpen die gebruik maken van breedbandige golfvormen.

Chapter 1

Introduction

1.1   Surveillance radars

The basic function of a radar (RAdio Detection And Ranging) is to detect objects and estimate their position and velocity. In the operational mode a radar transmits electromagnetic waves into the scene, then captures the echo reflected from the target and analyzes it to retrieve target location and motion parameters. The primary focus of this research is a surveillance radar, which is intended to provide situational awareness for security and defense applications. Such radar has to detect all moving targets present in the surrounding area and measure their range, velocity and bearings in azimuth and elevation. Range and velocity of the target can be estimated from the measured time delay and Doppler shift of the received signal respectively; the angular location of the target is obtained by scanning the outer space with a narrow beam: either mechanically with a standard fixed beam antenna, or electronically if a phased array antenna is employed. Therefore, for target range and velocity estimation in a single beam, the angular dimension is usually ignored [1].

Surveillance radars are designed to detect moving targets of interest in presence of strong unwanted echoes from ground, sea, clouds, precipitation, etc., referred to as clutter, or intentional interference called jammer. The presence of such parasitic signals can significantly reduce radar capability to detect the desired echoes. Consequently, the overall aim of the radar system design, including the selection of the antenna beamwidth, waveform parameters, power budget, signal processing, etc., is to improve visibility of weak targets against clutter and jammer. This implies enhancement of a target response and simultaneous suppression of a clutter echo and jammer, by exploiting the essential distinction of these signals. An interference of the latter class is usually concentrated in a narrow angle sector. Modern radars with

phased array antennas can mitigate the impact of jammers by creating an antenna radiation pattern with nulls in the directions of the interferers.

A clutter response in a surveillance radar, being the echo of multiple stationary or quasi-stationary (vegetation, sea surface, clouds) objects, is typically characterized by its large extension in space and narrow Doppler spectrum, concentrated around zero. Thus, to improve target visibility against clutter, a radar should, on one hand, transmit a short pulse to obtain a fine range resolution and, on the other hand, send a signal with a long duration for accurate estimation of the Doppler frequency shift, providing high velocity resolution. In order to meet these two contradictory requirements conventional surveillance radars transmit periodic sequences of pulses or sweeps (bursts or trains) as sounding signals. In order to decrease peak transmitting power modern radars typically send frequency or phase modulated pulses of longer duration. Each received pulse then passes through a pulse compression filter, which recovers the range profile of the scene with the range resolution:

$$\delta_R = \frac{c}{2B},\tag{1.1}$$

where B is the coherent bandwidth (bandwidth over which range compression is performed) of a transmitted pulse. The coherent bandwidth of conventional surveillance systems is typically small compared to the carrier frequency. Doppler analysis is performed by measuring the phase variation of the received signal from pulse to pulse, independently of the range measurement. The velocity resolution of a pulse burst depends on the number of pulses M as:

$$\delta_v = \frac{\lambda_c}{2(M-1)T_r},\tag{1.2}$$

where T_r is the pulse repetition interval (PRI) of the transmitted pulse train.

A single pulse train waveform however is rarely used in surveillance radars because of two limiting factors: ambiguities and fluctuations.

Ambuguities The essential limitation of the pulse train waveform comes from the range-Doppler ambiguities of such signals:

- Range ambiguities occur when the m-th transmitted pulse is reflected by a distant target and received after the pulses number $m + 1$, or $m + 2$ etc. have been transmitted by the radar. The received echo then can be assigned to any of the pulses transmitted already, creating ambiguities in target range estimation. The ambiguous range of a pulse radar:

$$R_a = \frac{cT_r}{2}\tag{1.3}$$

is controlled by the choice of the PRI T_r of the transmitted pulse train; c is the speed of light.

- Radar measures target Doppler frequency shift by estimating the phase variation of the targets echo in the successive pulses. The fundamental modulo 2π uncertainty of the phase measurements leads to ambiguous estimation of the targets Doppler frequency $f_D = 2v_0 f_c/c$ and therefore of its velocity v_0; here f_c stands for the radar carrier frequency. The ambiguity of target Doppler frequency estimation is therefore equal to the pulse repetition frequency (PRF) F_r of the burst and leads to velocity ambiguity:

$$v_a = \frac{\lambda_c}{2T_r},\tag{1.4}$$

where $\lambda_c = c/f_c$ is the wavelength at the radar carrier frequency.

Range and velocity ambiguities are related one to another as:

$$R_a v_a = \frac{c\lambda_c}{4}\tag{1.5}$$

and usually tuned by the selection of PRI (or PRF) according to (1.3), (1.4), assuming small variation of the radar carrier frequency (f_c) in the burst. For surveillance radars, operating at frequencies $f_c \in (1, 30)$ GHz ($\lambda_c \in (0.01, 0.3)$ m), the presence of multiple ambiguities, either in range, or in velocity, or both, must be considered.

Fluctuations The other limitation of a pulse train waveform arises due to fluctuation of the target and clutter responses. The targets of interest are complex objects with many surfaces, which have different range and angle towards the radar. The signal reflected from all these surfaces is summed coherently in the receiver, creating interfering picture of target reflection in angle and frequency. As a result the target may provide very weak signals for certain observation angles or frequencies of illumination (a phenomenon called target fading in the literature) [2]. The clutter response arises similarly, but the shape of the reflecting area is limited by the beamwidth and range resolution of the radar, instead of the physical dimensions of the object.

The effects of target fading and clutter fluctuation can be mitigated by observing the scene either from multiple directions, or at various frequencies. The former approach is realized in a multi-static radar, which is beyond the scope of this study. The latter method implies changing of radar carrier frequency within target observation time, called frequency agility and realized in most of modern radars.

Radar waveform and signal processing should consider the presence of ambiguities and exploit target and clutter fluctuations for better target visibility. The conventional approach to design a surveillance radar leads to the selection of narrowband

waveforms of the special form, described in the next section. Then, an emerging approach, which consists of using wideband waveforms for surveillance, is introduced. A wideband surveillance radar is demonstrated to provide the required means to resolve ambiguities and obtain diversity gain, with improved range and velocity resolution.

1.2   Narrowband radars

Narrowband radars are defined as radars with a fractional bandwidth (B/f_c) of less than 1%. They are mostly used for air and weather surveillance at long distances, with the target information being extracted from the base-band signal with a bandwidth of a few MHz. The targets of interest are located in the far field of the antenna and typically have dimensions smaller than radar resolution cell, which is of an order of $\delta_R \in \left(10^1, 10^3\right)$ m in range.

Most of conventional surveillance radars are narrowband. In order to overcome range-velocity ambiguities, they sequentially transmit a few bursts (pulse trains) with different PRFs [1], commonly referred to as a staggered PRF waveform. Then, clutter filtering, Doppler processing and target detection are performed in each burst separately and combined by some logical processor. The efficiency of such processing is often demonstrated in the noise-limited scenario, where fusion of detections in 2-3 bursts provides a unique estimation of targets range and velocity [2, 3].

In a complex environment scenario a moving target can be missed in some bursts. This happens when the folded over PRF Doppler frequency shift of the target is low, and, thus, the target echo cannot be discriminated from the clutter. The repetitive notches of a clutter filter create so-called "blind speeds" in the Doppler processing output. To diminish the impact of "blind speeds" on target detection, the operational radars transmit 3-6 bursts and process the outputs by means of "K-out-of-N" rule or other logic [1]. The selection of PRFs of the staggered waveform affects the velocity sensitivity of such processing and usually requires some compromise between clutter rejection, maximum velocity of a target and observation time [1, 3, 4]. In addition, modern radars can vary carrier frequency from burst to burst (frequency hopping) to mitigate fading effects due to the fluctuation of targets and clutter [2].

Surveillance radars usually transmit staggered waveforms with low PRF for unambiguous estimation of range. This design avoids clutter folding in range and thus prevents the situation when a weak response of ambiguous in range target has to be detected against a strong clutter response from nearby [1]. The procedure for ambiguities removal poses additional limitations on the range resolution of such systems. Namely, target extent and range migration during the observation time should be smaller than the radar range resolution δ_R for correct ambiguities removal, which implies typical $\delta_R \in \left(10^1, 10^3\right)$ m.

The need to transmit a few different bursts is detrimental to overall radar performance: the surveillance radar scans the outer space with the limited update rate of the system which poses strict limitations on the time-on-target. This finite time-on-target should be divided into a few bursts for ambiguities removal, which directly implies low coherent integration gain and limited Doppler resolution of such systems - both being crucial for detection of moving targets in clutter.

Therefore, detection of small and weak targets in a heavy environment is still a challenging task for existing radar systems. One way to improve detection of moving targets in clutter is to exploit high resolution waveforms and associated signal processing. Radar systems, exploiting such waveforms for target detection, are referred here as wideband radars.

1.3   Wideband radars

The term *wideband radar* appeared in the literature during the last decades to represent a new class of emerging technology, compared to the well-established narrowband and ultra-wideband (UWB) radars. Such radar systems serve for similar tasks, as the narrowband radars, and operate in the same frequency bands. But they have fractional bandwidth between 1% and 20%, over which the coherent processing can be performed, providing fine range resolution $\delta_R \in \left(10^{-1}, 10^1\right)$ m. Therefore, such systems are also called high resolution radars. In addition to target detection and position estimation, they can provide complementary information about the target shape and dimensions by means of accurate range profiling. This information can be used for separation of closely spaced targets and their classification by means of range profile analysis [5].

Wideband radars are essentially different from the *UWB* ones. The latter systems have fractional bandwidth greater than 20% [6]. The spectrum of the UWB systems is often wide enough to measure simultaneously the response of the target in different reflection regions - optical, resonance and low-frequency (or Rayleigh). These systems have low frequency component of the spectrum, which gives UWB radars unique capabilities of subsurface visibility and target shape identification from the frequency response of the target [5,6].

Fine range resolution makes wideband radars a promising technology for surveillance application. The detailed range measurement of the scene provides a number of direct benefits for the surveillance radar. Among them:

- Improved signal-to-clutter ratio (SCR) for detection of small targets at low altitude by reduction of the clutter patch;

- On-the-fly pre-classification of the targets from their high range resolution (HRR) profile;
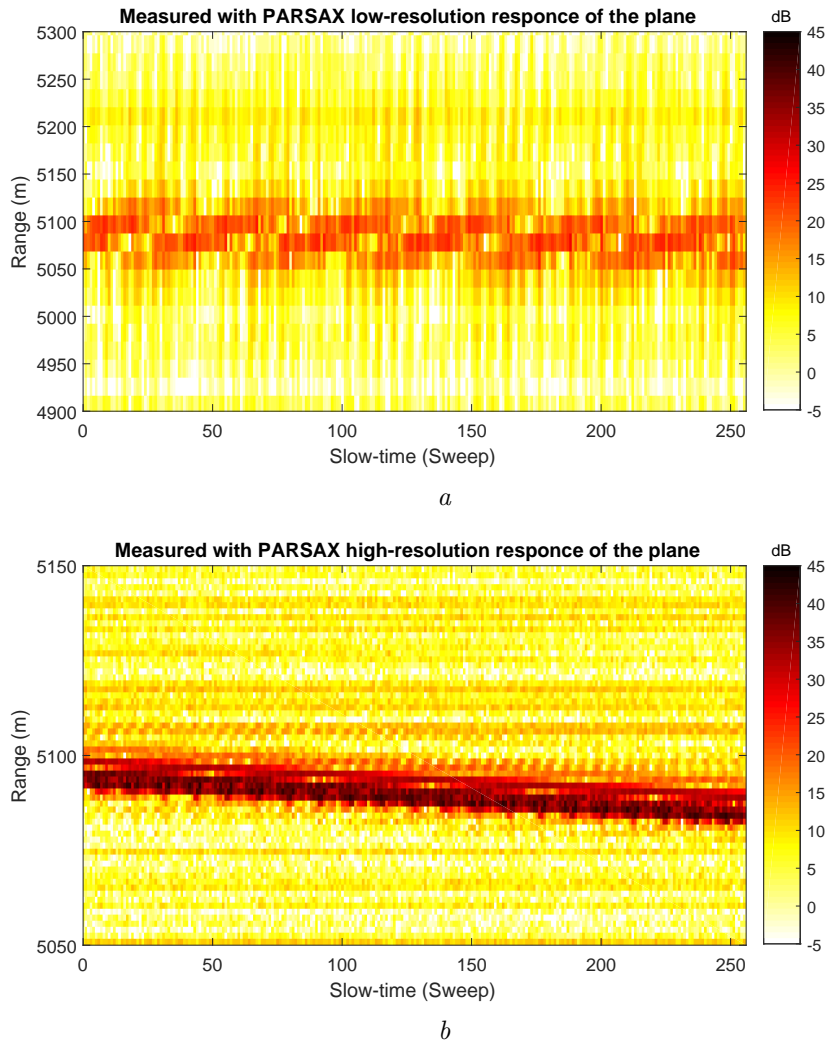
Figure 1.1: Response of a moving plane (Cessna 150), measured with PARSAX radar: a - Narrow-band mode, $B = 7.9$ MHz, $\delta_R \approx 19$ m; b - Wideband mode, $B = 95$ MHz, $\delta_R \approx 1.6$ m.

- Resolving multi-path reflections of low-altitude targets by separation of the direct and multi-path signals in range.

The direct benefits can be obtained when the signal bandwidth is increased, but the radar structure and processing gain are identical to conventional narrowband surveillance radars.

Wideband radars provide alternative solution to resolve velocity ambiguity. If the

Measured with PARSAX CNR in two resolution modes
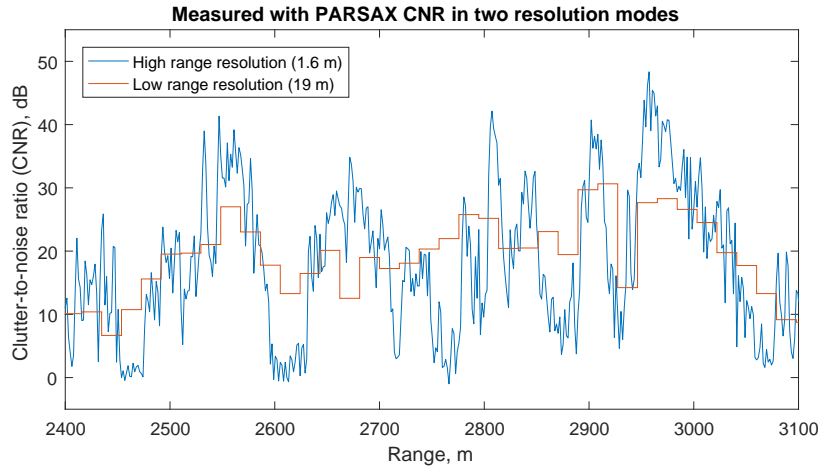
Figure 1.2: Clutter response, measured with PARSAX in two resolution modes: high range resolution ($\delta_R \approx 1.6$) and low range resolution ($\delta_R \approx 19$ m)

range resolution is high enough to observe target range variation during the coherent processing interval (CPI), then target's velocity can be measured using target range migration (also called range-walk) from pulse to pulse, demonstrated in Fig. 1.1, *b*. This coarse measurements of target velocity should be complemented with the Doppler information to obtain high velocity resolution. The coherent bandwidth and the total duration of the burst are then defined by the condition that the range migration per velocity ambiguity is large enough to select the correct velocity of the target:

$$v_a M T_r \gg \delta_R. \tag{1.6}$$

When the condition is satisfied, *a single burst of high-resolution pulses with low PRF can provide unambiguous measurement of the target's range and velocity simultaneously*, as demonstrated in e.g. [2, 7–9]. Moreover, it implies that in one burst a fast-moving target of interest ($|v_0| > v_a$) can compete with the clutter in a few adjacent range cells. In the HRR mode, the response of clutter is typically non-Gaussian and may have significant fluctuations over the range interval, elapsed by the target during the CPI. In that way, *target migration provides the means to exploit clutter diversity in one coherent pulse burst.* Measured range profile of ground clutter is presented in Fig. 1.2 in two resolution modes, showing rapid and large variation of clutter power over range in the HRR mode.

In meter or sub-meter range resolution, provided by a wideband radar, the size of

a range resolution cell is small compared to target dimensions, or:

$$B \gg \frac{c}{2\Delta_R}. \tag{1.7}$$

where Δ_R is target range extent. Thus, the typical targets of interest become extended in range. High resolution range response of a target provides equivalent information about the target to multiple measurements of the target response in frequency domain [2]. Therefore, *a wideband radar can provide target diversity by observing its high resolution range profile in one burst*, as demonstrated in [10–13].

An example of the target response, observed with a low range resolution (LRR) ($\delta_R \approx 19$ m) and with a HRR ($\delta_R \approx 1.6$ m), is demonstrated with the data record of PARSAX radar[1]. An observed target is a small plane Cessna 150, approaching the radar. Range migration of the target is clearly observed in the wideband mode, contrary to the narrowband case. Moreover, the target signature has fewer fluctuations in the high-resolution mode, because of splitting the response into multiple range cells. In fact, the reflection from the rotating propeller affects only the leading range cells of the target in the HRR mode, while in the LRR mode it results in fluctuation of the whole target response.

High range and velocity resolution, together with the ability to resolve velocity ambiguity and exploit target and clutter diversity in one burst make *a single burst of high resolution pulses an attractive option for modern surveillance radars*. The properties of such a waveform, including its efficiency for clutter rejection and target detection in complex scenario, are however poorly studied in the literature. In this thesis, that waveform is considered for application in surveillance radars and its advantages and challenges are investigated.

1.4   Challenges and selected approach

The waveform proposed here for a wideband surveillance radar significantly differs from the ones used in the conventional surveillance radars. The received signal is better interpreted with the HRR models of a target and clutter, which appropriately describe the phenomena, mentioned above. In order to benefit from the advantages of the wideband waveform, the appropriate techniques to resolve range-velocity ambiguities and to extract weak targets of interest from clutter should be developed. The proposed solution should be stable in difficult scenarios: when a few targets of interest are present in the vicinity of each other or clutter response has rapid fluctuations in range.

The resolution of velocity ambiguity using target migration observed in one long burst of high-resolution pulses is a challenging problem, because the difference in the

---

[1]The detailed description of PARSAX radar is given in Appendix A

target migration per velocity ambiguity (1.6) is often just a few range cells, depending on the waveform parameters. Testing every velocity hypothesis allows integrating coherently the response of a point-like target in all the pulses together at the correct velocity. However, at the hypotheses a few ambiguities apart, the response is also integrated coherently over a part of the CPI, which creates so-called ambiguous sidelobes[1]. The interpretation of the coherent processing output then becomes complicated due to the presence of multiple ambiguous sidelobes of the present targets and clutter. The existing non-parametric [8, 14] techniques provide limited improvement in suppression of ambiguous responses, while the parametric ones [9] require tuning of some parameters to reconstruct the scene. Moreover, these techniques provide only reconstructed target scene and do not solve the detection problem. In order to alleviate these limitations, novel high-resolution parametric-free spectrum estimation algorithms, namely Iterative Adaptive Approach (IAA) [15, 16] and Semi-Parametric (sparse) Iterative Covarince-based Estimator (SPICE) [17, 18] are proposed for unambiguous scene reconstruction. Then a detector, which can minimize the effect of ambiguous sidelobes, is proposed.

The ambiguous sidelobes of the wideband waveform arise not only for target response but also the clutter replica. The clutter response typically combines the response of multiple objects, present in the ground patch, observed by the radar, which can slowly move and thus have a spread spectrum. The diffuse spectrum of the clutter usually limits visibility of targets with small Doppler frequency shift and thus can affect the detection of the targets around ambiguous velocities. The degradation of target detection at the ambiguous-to-clutter velocities has been observed in some examples, e.g. [8, 19]; however, the overall study of the impact of the clutter spectrum on target detection with a wideband waveform is missing. The efficiency of diffuse clutter suppression in the proposed radar mode should therefore be evaluated for different parameters of clutter and target velocities. Such evaluation should be done assuming some shape of clutter Doppler spectrum, e.g. the model of Billingsley defined for vegetation clutter [20], and validated on real data records.

Target range migration during the CPI can be used to perform clutter filtering not only in Doppler frequency, but also in range dimension. This can provide certain benefits for detection of migrating targets against high resolution ground clutter, which is typically non-Gaussian and whose intensity distribution function generally has longer tail than the exponential one [21, 22]. Most distributions used to describe spiky clutter (including Weibull, K, Student and Gaussian distributions) can be shown in the form of the compound-Gaussian (CG) model [21–23], which provide separation of clutter spectrum characteristics from its power probability density function (PDF). Accounting for the clutter variation along the target range-walk and also for the target

---

[1]More details are given in Chapter 2

response variation over its range profile should help to mitigate the low SCR zones. In order to get these benefits, the detector providing clutter filtering in slow-time and range simultaneously should be developed.

The applicability of the proposed approaches will be evaluated in simulations and validated on real data records, collected with the HRR polarimetric radar system PARSAX, available at TU Delft [24, 25]. The overview of PARSAX radar is given in Appendix A.

1.5 Outline of the thesis

The remainder of the thesis is organized as follows:

Chapter 2 describes the data model for the received signal when the coherent bandwidth of the radar is increased. The mathematical model of a moving scatterer, which considers possible range migration of the target within the CPI, is presented. Target range migration is demonstrated to provide the unambiguous measurement of its range and velocity using a single burst with HRR. The advantages and challenges for the signal processing of wideband signals are analyzed using the ambiguity function of a wideband burst. The provided models for clutter and targets in the HRR mode demonstrate the benefits, which can be obtained with the use of wideband coherent waveforms.

Chapter 3 analyzes the effect of clutter Doppler spectrum on the performance of the wideband waveform at the ambiguous-to-clutter velocities. The influence of the waveform parameters and clutter characteristics on moving target detection at the ambiguous-to-clutter velocities is investigated and compared to the conventional staggered PRF waveform. Based on this, some recommendations for waveform design are formulated to improve target visibility against diffuse clutter in a wideband radar.

The publications related to this chapter are the following:

- N. Petrov, F. Le Chevalier, and A. Yarovoy, "Performance prediction of wideband unambiguous target detection in diffuse ground clutter," in *European Radar Conference (EuRAD)*. IEEE, 2016, pp. 97—100 ;

- F. L. Chevalier and N. Petrov, "Diversity considerations in wideband radar detection of migrating targets in clutter," *Science China Information Sciences*, vol. 62, no. 4, 2019.

Chapter 4 investigates the possibility to resolve velocity ambiguities and reconstruct the observed scene in the range-velocity plane using a single burst of HRR pulses as a sounding signal. The major challenge of the processing arises due to strong ambiguous sidelobes in the wideband ambiguity function: thus, in presence of ground clutter and possibly multiple targets in the data set, weak targets can

be masked by an ambiguous sidelobe of clutter or of another target. The proposed solution consists of applying high-resolution parametric-free spectrum estimators for unambiguous estimation of the scene, which are demonstrated to improve rejection of ambiguous sidelobes over the existing methods.

The publications related to this chapter are the following:

- N. Petrov and F. Le Chevalier, "Iterative adaptive approach for unambiguous wideband radar target detection," in *European Radar Conference (EuRAD)*. IEEE, 2015, pp. 45 — 48 ;

- N. Petrov and F. Le Chevalier, "Wideband spectrum estimators for unambiguous target detection," in *16th International Radar Symposium (IRS)*. IEEE, 2015, pp. 676—681 ;

- N. Petrov and F. Le Chevalier, "Fast implementation of iterative adaptive approach for wideband unambiguous radar detection" in *23rd European Signal Processing Conference (EUSIPCO)*. IEEE, 2015, pp. 1207—1211 .

Chapter 5 considers the problem of detecting moving targets with the wideband waveform. Due to range-migration effect, the detection is performed in the block of adjacent range cells, in which more than one target can be present, together with clutter. It is demonstrated that conventional radar detectors are not capable to detect the presence of multiple targets in a data set. Two approaches to detect multiple targets in the scene are proposed, which preserve the probability of false alarm at the required level and minimize false detections due to ambiguous sidelobes of the present targets. The performance of the proposed techniques is evaluated via numerical simulations.

The publication related to this chapter is the following:

- N. Petrov, F. Le Chevalier, and A. Yarovoy, "Unambiguous detection of migrating targets with wideband radar in Gaussian clutter," in *CIE International Conference on Radar (RADAR)*. IEEE, 2016, pp. 1—5.

Chapter 6 considers the detection of fast moving targets at the ambiguous-to-clutter velocities, in presence of non-homogeneous ground clutter, described by the compound-Gaussian (CG) model. Due to target migration, fast-moving targets compete with the clutter response from a few adjacent range cells during the CPI. In the high-resolution mode, the clutter power can vary significantly in these range cells. A detector of a range migrating target, which adapts to the clutter power variation along its path in range, is developed. The benefits of considering clutter variation in range for fast-moving target detection are presented and discussed.

The publications related to this chapter are the following:

- N. Petrov, F. Le Chevalier, and A. G. Yarovoy, "Detection of range migrating targets in compound-Gaussian clutter," *IEEE Transactions on Aerospace and Electronic Systems*, vol. 54, no. 1, pp. 37—50, 2018;

- N. Petrov, F. Le Chevalier, N. Bogdanović, and A. Yarovoy, "Range migrating target detection in correlated compound-Gaussian clutter," in *25th European Signal Processing Conference (EUSIPCO)*. IEEE, 2017, pp. 2216—2220 ;

- F. L. Chevalier and N. Petrov, "Diversity considerations in wideband radar detection of migrating targets in clutter," Science China Information Sciences, vol. 62, no. 4, 2019.

Chapter 7 summarizes the achievements obtained in the previous chapters and describes some open challenges, left for the future research.

Chapter 2

Theory of wideband coherent radars

This chapter explains the phenomena, which arise and become important if the coherently processed bandwidth of the radar increases. In the first section, the response of a moving point-like target, being observed by a wideband radar is investigated with an emphasis on the range migration effect. It is demonstrated that with a sufficiently large time-bandwidth product of the transmitted burst, it becomes possible to resolve velocity ambiguities in a single low PRF mode. The advantages and challenges for the signal processing in such a mode are analyzed with the corresponding wideband ambiguity function. In the second section, the description of the received radar data in a high-resolution mode is presented, with emphasis on the signature of extended targets and clutter modeling. The provided models of targets and clutter, that will be used throughout the text, demonstrate the benefits, which can be obtained with the use of a wideband coherent waveform.

2.1 Signature of a moving target

2.1.1 Response of a moving scatterer

Assume a moving point-like target (scatterer) is illuminated by the wideband radar and define the response of this target acquired by the radar, following the lines of [8]. The wideband radar, whose processing chain is depicted in Fig. 2.1, transmits a coherent burst of M wideband pulses in the CPI, which can be described over time
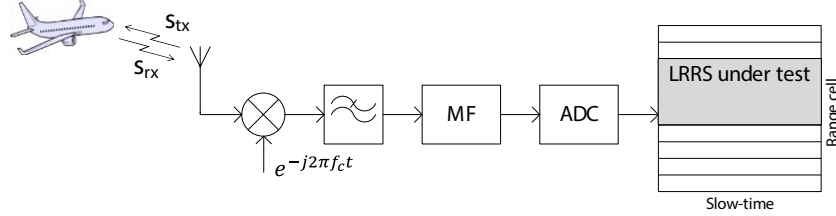
Figure 2.1: Block diagram of signal processing in a wideband radar

$t \in [0, T]$ as:

$$s_{\mathrm{tx}}(t) = \sum_{m=0}^{M-1} s(t - mT_r)e^{j2\pi f_c t},$$ (2.1)

where $s(t)$ is the complex envelope of a single pulse defined on $t \in [0, T_r]$ and $m = 0 \ldots M - 1$ is the pulse (slow-time) index. To simplify the notations, assume that the transmitted signal occupies frequencies $f \in [f_c, f_c + B]$.

Assume a single point-like target is present in the angle sector, illuminated by the radar. The transmitted signal reflects from the target and arrives back to the radar as the scaled and delayed copy of the transmitted waveform:

$$s_{\mathrm{rx}}(t) = \alpha s_{\mathrm{tx}}(t - \tau(t)),$$ (2.2)

where α is a complex amplitude proportional to the target radar cross section (RCS) and propagation effects. The time delay of the received signal depends on the target range in the beginning of CPI R_0 and its radial velocity v_0 as:

$$\tau(t) = \frac{2(R_0 - v_0 t)}{c} = \tau_0 - \frac{2v_0}{c}t.$$ (2.3)

Combining (2.1), (2.2) and (2.3) together, the received signal becomes:

$$s_{\mathrm{rx}}(t) = \alpha \sum_{m=0}^{M-1} s(t - mT_r - \tau(t))e^{j2\pi f_c(t-\tau(t))}.$$ (2.4)

The received signal is down-converted to the baseband (bb) for subsequent matched filtering and sampling. Define the fast-time as $t' = t - mT_r$, then the baseband signal obeys the conventional fast-time / slow-time representation [2]:

$$s_{\mathrm{bb}}(t', m) = \alpha s\left(t' - \tau(mT_r + t')\right) e^{-j2\pi f_c \tau(mT_r + t')}$$
$$= \alpha s\left(t' - \tau_0 + \frac{2v_0}{c}mT_r + \frac{2v_0}{c}t'\right) e^{-j2\pi f_c\left(\tau_0 - \frac{2v_0}{c}mT_r - \frac{2v_0}{c}t'\right)}.$$ (2.5)

For a wideband pulse radar, the radial displacement of the target within one pulse duration $T_p \leq T_r$ can be assumed negligible compared to the range resolution: $|v_0 T_p| \ll \delta_R$. However, during the whole CPI, the target can move over a radial distance exceeding radar range resolution: $v_0 T > \delta_R$, which is called target range migration or range-walk. Thus, the received baseband signal can be shown as:

$$s_{\text{bb}}(t', m) \approx \alpha s\left(t' - \tau_0 + \frac{2v_0}{c} m T_r\right) e^{j 2\pi f_c \frac{2v_0}{c}(m T_r + t')}, \qquad (2.6)$$

where the constant terms are (and will be) incorporated in the constant α with no loss of generality.

Since the low PRF mode is considered, it is assumed that no range ambiguities occur: $R_0 + |v_0 M T_r| < R_a$. Then, the matched filter (mf) can be applied to the rearranged signal (2.6) pulse by pulse:

$$s_{\text{mf}}(t', m) = \int s_{\text{bb}}(\xi, m) s(t' - \xi) d\xi = \int S_{\text{bb}}(f, m) S^*(f) e^{j 2\pi f t'} df, \qquad (2.7)$$

where f denotes fast-frequency, conjugated with fast-time by Fourier transform (FT), $(\cdot)^*$ stands for the complex conjugate and $S_{\text{mf}}(f, m), S_{\text{bb}}(f, m), S(f)$ are the spectrum representations of $s_{\text{mf}}(t', m), s_{\text{bb}}(t', m), s(t')$ accordingly. The spectrum of the received signal (2.6) is:

$$S_{\text{bb}}(f, m) = \int s_{\text{bb}}(t', m) e^{-j 2\pi f t'} dt'$$

$$= \alpha e^{j 2\pi f_c \frac{2v_0}{c} m T_r} \int s\left(t' - \left(\tau_0 - \frac{2v_0}{c} m T_r\right)\right) e^{j 2\pi f_c \frac{2v_0}{c} t'} e^{-j 2\pi f t'} dt'$$

$$= \alpha e^{j 2\pi f_c \frac{2v_0}{c} m T_r} e^{-j 2\pi \left(f - f_c \frac{2v_0}{c}\right)\left(\tau_0 - \frac{2v_0}{c} m T_r\right)} S\left(f - f_c \frac{2v_0}{c}\right) \qquad (2.8)$$

$$\approx \alpha e^{j 2\pi f_c \frac{2v_0}{c} m T_r} e^{-j 2\pi f \left(\tau_0 - \frac{2v_0}{c} m T_r\right)} S\left(f - f_c \frac{2v_0}{c}\right),$$

where the term $e^{-j 2\pi (2v_0/c)^2 f_c m T_r}$ for typical air and ground targets ($v_0 \ll c$) can be neglected.

Substitution of (2.8) into (2.7) and applying inverse FT over fast-frequency gives the output of the matched filter:

$$s_{\text{mf}}(t', m) = \int S_{\text{bb}}(f, m) S^*(f) e^{j 2\pi f t'} df$$

$$= \alpha e^{j 2\pi f_c \frac{2v_0}{c} m T_r} \int e^{-j 2\pi f \left(\tau_0 - \frac{2v_0}{c} m T_r\right)} S\left(f - f_c \frac{2v_0}{c}\right) S^*(f) e^{j 2\pi f t'} df \qquad (2.9)$$

$$= \alpha e^{j 2\pi f_c \frac{2v_0}{c} m T_r} \chi_{\text{p}}\left(t' - \left(\tau_0 - \frac{2v_0}{c} m T_r\right), f_c \frac{2v_0}{c}\right),$$

where

$$\chi_{\mathrm{p}}\left(\tau, f_D\right) = \int s(t - \tau)e^{-j2\pi f_D t}s^*(t)dt = \int S(f - f_D)e^{j2\pi f\tau}S^*(f)df \qquad (2.10)$$

is the complex-valued ambiguity function of the basic pulse $s(t)$ [2]; the degree of ambiguity is usually measured with $\left|\chi_{\mathrm{p}}\left(\tau, f_D\right)\right|^2$.

The output of the matched filter (2.9) demonstrates that the radial movement of the target affects the received signal in three ways: first, the phase of the received signal varies from pulse-to-pulse with the Doppler frequency $f_D = 2v_0 f_c/c$; second, the target has range migration proportional to its velocity over slow-time and, third, the response of each pulse in the burst is distorted due to Doppler shift of the returned signal. The last factor can be diminished by selecting a Doppler-tolerant waveform [26] as a primitive pulse $s(t)$, which satisfies:

$$\chi_{\mathrm{p}}\left(t - \tau, f_D\right) \approx \chi_{\mathrm{p}}\left(t - \tau, 0\right) = u_{\mathrm{p}}\left(t - \tau\right), \qquad (2.11)$$

and $u_{\mathrm{p}}\left(t\right)$ is called point spread function or impulse response of the pulse $s(t)$.

The output of the matched filter (2.9) is sampled by the analog-to-digital converter with the rate $1/B$ and becomes a function of the range cell (of fast-time index) $k' = t'B$ and slow-time index m:

$$s_{\mathrm{ft,st}}(k', m) = \alpha e^{j2\pi f_D T_r m}u_{\mathrm{p}}\left(k' - \left(\tau_0 B - \frac{v_0 T_r}{\delta_R}m\right)\right), \qquad (2.12)$$

where the subscript shows that the signature is defined in fast-time (ft) / slow-time (st) samples.

2.1.2 Interpretation of the target signature

The signature of a moving target (2.12) demonstrates a moving target has the range-walk of $v_0 T_r(M - 1)/\delta_R$ range cells during the CPI. This effect can be neglected for slow targets, but should be considered for processing the responses of fast moving targets, whose range displacement during CPI is much larger than the radar range cell. The coherent processing of these targets should be performed over the block of K adjacent range cells, large enough to encompass the response of the target during the whole CPI. Hereinafter, such block of range cells is called a low range resolution segment (LRRS).

Define by $k'_0 = \tau_0 B$ the range cell of the target at the beginning of CPI. Assume that during the observation time the target is present in the LRRS occupying the range cells $k' = k_{\mathrm{beg}}, \ldots, k_{\mathrm{beg}} + K - 1$, where:

$$\begin{cases} k_{\mathrm{beg}} \leq \min\left(k'_0, \ k'_0 + \frac{v_0 M T_r}{\delta_R}\right); \\ k_{\mathrm{beg}} + K - 1 \geq \max\left(k'_0, \ k'_0 + \frac{v_0 M T_r}{\delta_R}\right). \end{cases} \qquad (2.13)$$

The number of range cells K in the LRRS is selected according to the maximum expected velocity of a target $v_{\max}$ and its maximum expected range extent $\Delta_{R,\max}$:

$$K \geq \frac{|v_{\max}|T_r M + \Delta_{R,\max}}{\delta_R}. \qquad (2.14)$$

Concentrating on the LRRS segment including the target response during CPI, the bi-dimensional structure of the wideband target signature can be alternatively represented after applying FT over fast-time or slow-time dimension, or after applying both. The target signature in the four domains demonstrates the difference between the responses of a moving target with wideband and narrowband waveforms and defines the wideband modification of the standard Doppler processing.

To concentrate on the phase relation in the received signal, the spectrum of the transmitted pulse is assumed to be flat within the occupied frequency band:

$$|S(f)|^2 = \text{const}, \ \forall f \in [f_c, f_c + B], \qquad (2.15)$$

and impulse response satisfies: $u_{\mathrm{p}}(0) = 1$. An example of the wideband point target signature is depicted in Fig. 2.2. Herein the wideband radar with parameters $f_c = 10$ GHz, $B = 0.5$ GHz, $T_r = 1$ ms, $M = 64$ is assumed and the target has velocity is $v_0 = 45$ m/s and its range at the beginning of CPI corresponds to $k_0 = 13$.

Fast-time / slow-time signature

Concentrating on the range cells in the LRRS under test and denoting $k = k' - k_{\mathrm{beg}}$ and $k_0 = k_0' - k_{\mathrm{beg}}$, the received signal (2.12) can be shown as the product of the constant term α and the target signature in the LRRS:

$$T_{\mathrm{ft,st}}(k,m) = e^{j2\pi f_D T_r m} u_{\mathrm{p}}\left(k - \left(k_0 - \frac{v_0 T_r}{\delta_R}m\right)\right), \qquad (2.16)$$

with $k = 0, \ldots, K-1$.

The target signature combines the phase variation from pulse to pulse due to Doppler frequency shift with the displacement of the impulse response of the transmitted pulse along the target trajectory, which is defined in the LRRS by the line $k(m) = k_0 - \frac{v_0 T_r}{\delta_R}m$. The fast-time / slow-time signature of the moving target is demonstrated in Fig. 2.2, a.

Fast-frequency / slow-time signature

Considering a flat spectrum of the transmitted waveform (2.15) and Doppler tolerance of a transmitted pulse by means of $S(f - f_D) \approx S(f)$, the target signature in the fast-frequency / slow-time domain becomes (see derivations in Appendix B.1):

$$T_{\mathrm{ff,st}}(l,m) = \frac{1}{K} e^{j2\pi f_D T_r m} e^{-j2\pi \frac{k_0}{K} l} e^{j2\pi \frac{v_0 T_r}{\delta_R K} lm}, \qquad (2.17)$$
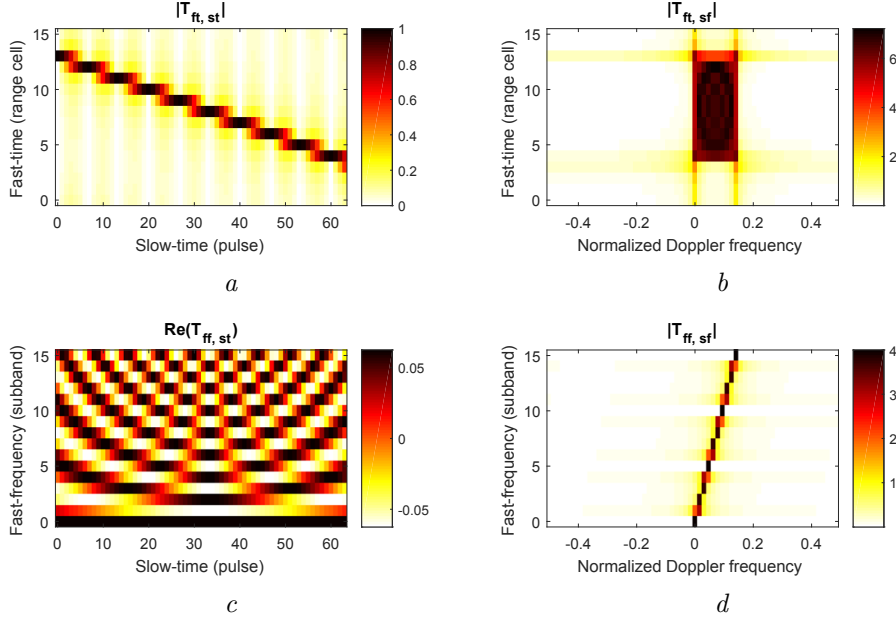
Figure 2.2: Wideband signature of a moving target in: a - fast-time / slow-time; b - fast-time / normalized Doppler frequency; c - fast-frequency/ slow-time; d - fast-frequency / normalized Doppler frequency.

where $l = 0, \ldots, K - 1$ is the fast-frequency index. The real part of (2.17) is demonstrated in Fig. 2.2, c.

According to (2.17), the fast-frequency / slow-time target signature is a product of three exponential terms. The first exponential term defines the phase variation from pulse-to-pulse according to the Doppler frequency. The second one models the range frequency of the target at the range cell k_0. The last term is called the coupling term due to its dependence on l and m together; it models the range migration, observed by the wideband radar for fast targets.

Fast-frequency / Doppler frequency signature

The fast-frequency/Doppler (slow) frequency representation of the target response is derived in Appendix B.2 and shown as:

$$
\begin{aligned}
T_{\text{ff,sf}}(l, f_d) = \frac{M}{K} e^{-j2\pi \frac{k_0}{K} l} e^{-j2\pi \left(f_d - f_D \left(1 + \frac{B}{K f_c} l \right) \right) \frac{M-1}{2} T_r} \\
\cdot \operatorname{sinc} \left(\left(f_d - f_D \left(1 + \frac{B}{K f_c} l \right) \right) M T_r \right),
\end{aligned}
\tag{2.18}
$$

where f_d is unfolded Doppler frequency and $\mathrm{sinc}(x) = \frac{\sin(\pi x)}{\pi x}$. The folded Doppler frequency $f'_d \in [-F_r/2, F_r/2]$ can be obtained using transformation: $f'_d = F_r \mathrm{frac}\left(\frac{f_d}{F_r}\right)$, where $\mathrm{frac}(x) = x - [x]$ gives $\mathrm{frac}(x) \in [-0.5, 0.5)$ and $[x]$ is rounding towards nearest integer operator.

This representation demonstrates the variation of the Doppler frequency in the frequency band according to $f_d(l) = f_D\left(1 + \frac{B}{K f_c}l\right)$, $\forall l = 0, \ldots, K-1$. The Doppler spectrum of the target is therefore concentrated (the main lobe of the Doppler processing is located in) the frequency interval: $f_d(l) \in \left[f_D, f_D\left(1 + \frac{B}{f_c}\right)\right]$. The fast-frequency/slow-frequency target signature in the folded Doppler domain is depicted in Fig. 2.2, d.

Fast-time / Doppler frequency signature

Starting from (2.18), the fast-time / Doppler frequency target signature is obtained by applying inverse FT over fast-frequency (for details see Appendix B.3):

$$T_{\mathrm{ft,sf}}(k, f_d) \approx \left|\frac{\delta_R}{v_0 T_r}\right| \Pi_{[k_0, k_0 - \frac{v_0 M T_r}{\delta_R}]}(k)\, e^{j2\pi(f_d - f_D)\left(\frac{f_c}{B f_D}(k - k_0) + \frac{T_r}{2}\right)} \tag{2.19}$$

and assuming that target range-walk withing one PRI is small compared to the radar range resolution. Here

$$\Pi_{[t_1, t_2]}(t) = \begin{cases} 1, & t \in (t_1, t_2); \\ \frac{1}{2}, & (t = t_1) \vee (t = t_2); \\ 0, & t \notin [t_1, t_2]. \end{cases} \tag{2.20}$$

Herein the limits of $\Pi_{[t_1, t_2]}(t)$ are set assuming $v_0 < 0$ and so increasing range of the target with time. In case $v_0 > 0$ the limits should be flipped.

According to (2.19), the target signature in the range / Doppler domain is spread approximately over the rectangle. The size of this rectangle in range is defined by the target range migration in range cells during the CPI, and the spread in Doppler is proportional to the variation of the Doppler frequency of the received signal over the coherently processed bandwidth. The shape of the target signature in range/Doppler domain is shown in Fig. 2.2, b

To sum up, a response of a moving target in a wideband radar experiences the range-migration phenomenon, which can be alternatively interpreted as widening of the target Doppler spectrum, proportionally to the target velocity and the bandwidth of the transmitted signal. It was demonstrated that both the range cell variation of the target during the CPI and the widening of the Doppler spectrum depends on the actual target velocity, but not on its ambiguous measurement via Doppler frequency

shift, and thus can be used for discrimination of the moving targets of interest from the quasi-stationary clutter.

2.1.3   Wideband ambiguity function

Knowing the response of the wideband burst to a moving scaterrer, the matched filter processing for the wideband burst can be determined. The output of such processing is characterized by the ambiguity function of the wideband pulse burst (referred hereinafter by wideband ambiguity function):

$$\chi_{WB}(\tau_0, v_0) = \alpha_1 \int s_{\mathrm{rx}}(t; \tau_0, v_0) s_{\mathrm{rx}}^*(t; 0, 0) dt. \tag{2.21}$$

Here $s_{\mathrm{rx}}(t; \tau_0, v_0)$ is the response of the moving target (2.2) with the target time delay τ_0 and velocity v_0 of (2.3) being tackled as extra parameters; α_1 is a normalization constant, which ensures the ambiguity function property: $\chi_{WB}(0,0) = 1$.

Applying the transformations (2.2) - (2.16) to both signals in (2.21) and focusing on the LRRS with the target, the wideband ambiguity function can be written as:

$$\chi_{WB}(\tau_0, v_0) = \alpha_1 \sum_{k=0}^{K-1} \sum_{m=0}^{M-1} T_{\mathrm{ft,st}}(k, m; \tau_0, v_0) T_{\mathrm{ft,st}}^*(k, m; 0, 0). \tag{2.22}$$

Herein, the target signature in slow-time/fast-time domain (2.16) is considered. However, the other descriptions of the target signature (2.16) - (2.19) can be used to obtain the same ambiguity function.

Let $\mathbf{T}(\tau, v)$ be the $K \times M$ matrix, whose elements are defined by the target signature in the LRRS: $\mathbf{T}_{k,m}(\tau, v) = T_{\mathrm{ft,st}}(k, m; \tau, v)$, $\forall k = 0, \ldots, K-1, m = 0, \ldots, M-1$. The vectorization of $\mathbf{T}(\tau, v)$ gives $KM \times 1$ steering vector of a moving target:

$$\mathbf{a}(\tau, v) = \mathrm{vec}\left(\mathbf{T}^T(\tau, v)\right). \tag{2.23}$$

With these notations, the signature of a moving target in the LRRS (2.16) can be written as: $\mathbf{s} = \alpha \mathbf{a}(\tau_0, v_0)$. Note that the signature of a non-migrating target at the range cell k_0 of the LRRS is fully described by M adjacent elements of: $\mathbf{a}_{(k_0-1)M, \ldots, k_0 M - 1}(\tau, v)$ which is a standard one dimensional Doppler signature in absence of range migration.

Using the steering vector notation (2.23), the wideband ambiguity function can be obtained by:

$$\chi_{WB}(\tau_0, v_0) = \frac{1}{M} \mathbf{a}(\tau_0, v_0) \mathbf{a}^H(0, 0). \tag{2.24}$$

The examples of a narrowband (conventional Doppler processing) and of a wideband ambiguity function are depicted in Fig. 2.3 for a burst of $M = 32$ coherent
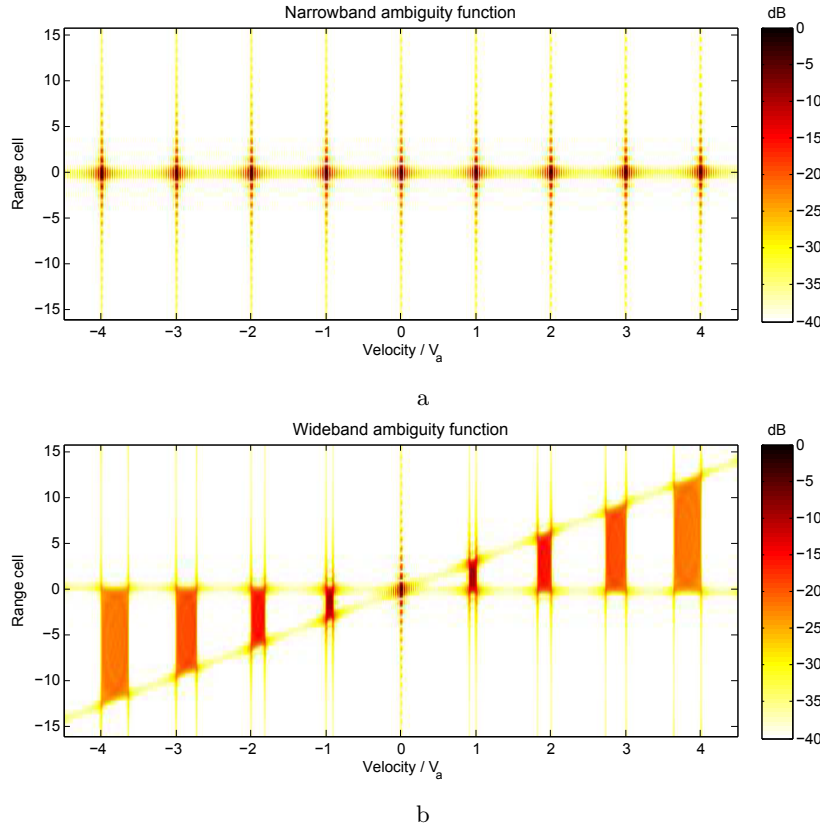
Figure 2.3: *a* - Narrowband ambiguity function, $B/f_c = 0.001$, $M = 32$, *b* - Wideband ambiguity function, $B/f_c = 0.1$, $M = 32$,

pulses with impulse response $u_p(t) = \text{sinc}(t)e^{-j\pi t}$. The velocity axis is plotted in terms of velocity ambiguities v_a and the range grid is normalized to the range resolution cell δ_R and limited to the vicinity of the target - so no range ambiguities appear. The shape of the wideband ambiguity function in Fig. 2.3 is notably different from the narrowband one. The narrowband ambiguity function has repetitive ambiguities (alike grating lobes) in velocity, essential for a low-PRF pulse train. On the contrary, the wideband ambiguity function has one distinct main lobe, located at the origin, and multiple responses around ambiguous velocities, called therefore ambiguous sidelobes. Therefore, *a burst of wideband pulses at low PRF provides a unique possibility to measure target range and velocity unambiguously (without ambiguities) simultaneously in one CPI.*

The n-th ambiguous sidelobe is placed around the velocity $v_0 + nv_a$, where $n \in \mathbb{Z}, -v_{\max}/v_a \leq n \leq v_{\max}/v_a, n \neq 0$. The range spread of the sidelobe is defined by the target range-walk at the examined velocity: thus, the n-th sidelobe spreads the energy of the target over $|n|v_a MT_r$ meters or equivalently, $|n|MB/f_c$ range cells. Similarly, the ambiguous response is spread in velocity over $|n|v_a B/f_c$ m/s, which is equal to $|n|MB/f_c$ velocity resolution cells. Therefore, the $|n|$-th sidelobe is spread in both domains over $|n|MB/f_c$ resolution elements and has the level of approximately:

$$\mathrm{SL}_n \approx \left(\frac{f_c}{|n|MB} \right)^2 . \tag{2.25}$$

Evidently, the ambiguous sidelobe at $|n| = 1$ is the strongest and for typical parameters of the burst it is between -20 to -5 dB. For example, the ambiguity function plotted in Fig. 2.3, $\mathrm{SL}_1 \approx -10.1$ dB. Such high level of the sidelobes is typically not accepted in surveillance radars, aimed to detect weak targets in a strong clutter. Typical surveillance radars require the sidelobe level of -30 dB or lower [3, 6, 27], achieved with the weighting applied with range compression and Doppler processing. Therefore, the presence of ambiguous sidelobes in the wideband ambiguity function should be considered in processing of wideband data.

2.1.4 Effects of target acceleration and cross-range movement

The target signature (2.16) has been derived assuming constant radial movement of the target during the CPI. However, the real targets rarely move along such an ideal trajectory and often have moderate radial acceleration (a_0) or cross-range velocity v_c during the CPI. As a result, the target range becomes non-linear function of time, contrary to (2.3). The effect of non-linear movement can be neglected as soon as the induced variation of the Doppler frequency does not exceed one half of the velocity (or Doppler) resolution: $\delta_v = v_a/M = \lambda_c/(2T)$.

The strongest echo of the target is expected to be the reflection from a non-deformable part of the target, and the detection of the target and its parameters estimation is performed on this signal. The signal reflected from the deformable parts of the target (rotating blades, wheels, jets) is therefore neglected for the analysis here.

The radial acceleration of the target can be neglected with the proposed wideband waveform as long as:

$$a_0 < \frac{\lambda_c}{4T^2} . \tag{2.26}$$

For radar operating at high carrier frequencies the condition (2.26) is rather strict: e.g. for $T = 50$ ms and $\lambda_c = 3$ cm it becomes $a_0 < 3$ m/s^2, and might be violated by rapidly maneuvering targets. In that case, target motion parameters can be extracted

from the data after detection, using one of the available approximations of the target motion [28–31]. However, target detection is usually performed ignoring possible target acceleration, to avoid additional dimension (in addition to range and velocity) of the target search.

To derive similar condition to the target cross-range velocity, recall that a target observed at distance R_0 during time duration MT_r and moving with velocity v_c oriented perpendicular to the radar line of sight, generated the velocity spread of the received signal over $\Delta_v = v_c^2 MT_r / R_0$. This cross-range movement can be neglected if:

$$v_c^2 < \frac{\lambda_c R_0}{4T^2}, \tag{2.27}$$

which strongly depends on the range to the target. For typical parameters of the surveillance radar (range of tens or hundreds of km and CPI less then 100 ms) the effect of its cross-range movement is negligible.

2.2   A model of received data

The received data of a wideband radar to be analyzed is a LRRS segment under test. It commonly contains the reflections from all the objects present in the volume, limited by the radar beam-width and the ranges of interest, which might include the target of interest, but also the reflections from the stationary and slowly moving objects (as vegetation), referred to as clutter. Considering also inevitable presence of noise, the general model of the radar data can be written as:

$$\mathbf{y} = \sum_{s=1}^{S} \alpha_s \mathbf{a}(\tau_s, v_s) + \mathbf{c} + \mathbf{n}, \tag{2.28}$$

where $\mathbf{c}$ and $\mathbf{n}$ are vectorized versions of the clutter and noise responses in the LRRS under test and $\alpha_s, \forall s = 1, \dots, S$ are the complex back-scattering coefficients of the present scatterers building up a physical target, as explained shortly. To make clear the phenomena observed by a wideband radar in presence of extended targets and clutter in the scene, their models are briefly described here.

2.2.1   Extended targets

Surveillance radars are designed to detect and locate moving objects of interest. Typical targets of a surveillance radar are therefore planes, aircraft, small gliders, etc. These objects have dimensions of $d = 5$ meters or larger, although some modern drones can be much smaller. Most of these targets, when observed by a wideband radar with the meter range resolution $\delta_R \approx 1$ m become extended in range. Therefore,

a point-like model of the target, widely used for narrowband radars, is not applicable for wideband data description anymore.

Alternatively, an extended non-deformable target can be modeled as a composition of multiple isotropic non-interacting scatterers located within the physical extent of the target $\mathcal{D}$ [2, 32]. Denoting the distribution of the complex back-scattering coefficient withing $\mathcal{D}$ by $I(x, y, z)$[1], the target response can be expressed as:

$$\mathbf{s} = \int_{\mathcal{D}} I(x, y, z) \, \mathbf{a} \left(\frac{2}{c} \sqrt{x^2 + y^2 + z^2}, v_0 \right) dx \, dy \, dz. \tag{2.29}$$

With no loss of generality assume that the radar is pointed along the x axis, so $x = R$. Moreover, consider the case of small target cross range extent compared to the radar cross-range resolution and write the response of an extended target as:

$$\mathbf{s} = \int_{\mathcal{D}_x} \left(\int_{\mathcal{D}_{y,z}} I(x, y, z) \, dy \, dz \right) \mathbf{a} \left(\frac{2x}{c}, v_0 \right) dx, \tag{2.30}$$

where the inner integral denotes the cross range extent of the target at the range x. Thus, the response of an extended target is the convolution of its projection on the line of sight with the signature of a point like target [2].

The model (2.30) describes accurately the reflection phenomenon of extended target, but has limited applicability because of no knowledge of $I(x, y, z)$ in practice. To obtain a practical model, usually some assumptions about the structure of $I(x, y, z)$ are imposed. The most often used are the sparse structure of $I(x, y, z)$, according to which the target is modeled by a few point-like scatterers with various back-scattering coefficients [32], and the statistical model, which describes $I(x, y, z)$ as a random process with known distribution (usually Gaussian) and correlation properties. Both models are very general and give possibility to describe targets with different shapes and RCS distribution in $\mathcal{D}$, providing feasible models over large frequency bands [2, 33].

The ability of a wideband coherent radar to observe physical objects as extended targets gives it valuable advantages over the narrowband radars. As follows from (2.30), the wideband radar can observe the variation of the target RCS in the range, and thus *provide the way to exploit target diversity within one burst*. It means that within one burst, by combining the target response from multiple range cells, the wideband radar can decrease the probability to be trapped in the low RCS response of the target. A narrowband radar cannot provide such information in one burst (for typical targets) and delivers a few independent measurements of the target response in frequency domain by shifting the carrier frequency from one burst to another.

---

[1]Scatterers location $I(x, y, z)$ corresponds to the beginning of CPI

2.2.2 Clutter

In a typical scenario, clutter results from the returns of ground or sea surface, clouds, precipitation (rain, snow, hail). These returns can significantly exceed the level of the noise, inevitable in any real system, and usually have a narrow Doppler spectrum, concentrated around zero. However, the presence of clutter can significantly affect the detection of moving targets of interest. Thus, clutter is essentially the limiting factor for detection of targets with small Doppler frequency, namely the targets with the radial velocity close to $nV_a, n \in \mathbb{Z}$.

The crucial task of the radar is to decide if the target is present in the scene, or the returned signal contains the clutter response only. The development of a detector, which should answer this question, requires some assumptions on the statistical model of clutter. With the LRR radars, the clutter is usually assumed to obey complex multivariate Gaussian distribution, which arises by considering the number of scatterers in the observed resolution cell to be infinitely large and therefore justified by the central limit theorem [2, 21].

When the radar resolution increases, the number of scatterers per resolution cell cannot be assumed infinitely large anymore, which makes the application of the central limit theorem and the following assumption on Gaussian clutter not valid anymore. Moreover, the analysis of multiple data sets including sea and ground observations demonstrated that the HRR clutter does not follow Gaussian model and the intensity distribution have larger tails than the exponential distribution, which is the intensity distribution of the Gaussian model [21, 34–37]. The physical interpretation of the observed scattering phenomenon in HRR radar has been given in [38], where the authors demonstrated that random but finite number of scatterers in a range cell leads to K distribution of the observed clutter intensity, which can be obtained as a mixture of exponential distributions [39]. Moreover, it has been demonstrated that clutter representation by the mixture of exponential distributions is valid for a wide class of distributions, including Weibull, K, Student and Gaussian ones [21–23]. The extension of intensity distribution models to the multivariate models of the complex returns led to the compound clutter models (CG process, spherically invariant random vectors (SIRV)), which are the modern trend for high-resolution clutter modeling and analysis [21, 22]. The compound representation of clutter allows separating its spectrum characteristics from the power PDF, which provides useful tools for clutter analysis and modeling.

In a general way, a complex CG vector $\mathbf{c}$ can be written as a product of the square root of the positive scalar quantity τ, referred to as texture, and zero-mean complex Gaussian vector $\mathbf{g}$ with unit variance, called speckle [21]. The speckle component $\mathbf{g}$ models clutter spectrum characteristics and the texture defines the local power. The texture describes the variation of the clutter power in space and time - the fluctuation
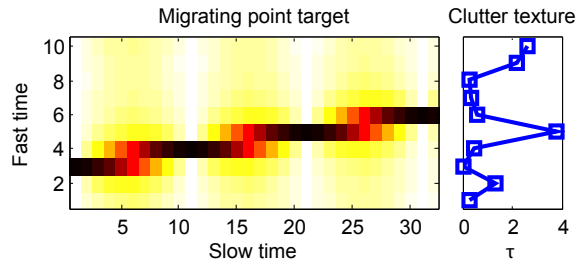
Figure 2.4: Migrating target in a spiky clutter

in time, essential for sea clutter, being slow and usually assumed negligible within a dwell time (or burst time of the proposed waveform) [40]. On the other hand, texture alteration in space depends on the observed scene and radar range resolution and thus can exhibit continuous variations of the local power in space, with the spatial correlation interval down to a range resolution cell [40].

Most of the existing studies on CG clutter focus on a single range cells scenario, encompassing an expected point-like target during the whole CPI (e.g. [21, 23]). Obviously, this scenario is not adequate for the proposed waveform, which allows target migration to be observed during CPI, and thus requires coherent processing of a whole LRRS. The model of CG clutter in a block of range cells requires making an assumption on the texture variations with range. The existing studies (mostly aimed at detection of extended but non-migrating targets) are based on one of two assumptions: either texture changes from one LRRS to another and constant within a LRRS (completely correlated texture) [13], or it has a cell to cell variation within a LRRS [11, 12]. For detection of range migrating targets, the first assumption has no physical meaning since it makes clutter spatial correlation be a function of the LRRS dimension, which, in turn, depends on the target parameters (2.14).

Then, if clutter texture variation from one range cell to another is considered, the clutter response in the LRRS can be represented by $K \times M$ matrix $\mathbf{C}$, with

$$\mathbf{C}_{k,*} = \sqrt{\tau_k} \mathbf{g_k}^T, \quad \forall k = 0, \ldots, K-1. \tag{2.31}$$

Here $\mathbf{C}_{k,*}$ stands for the k-th row of matrix $\mathbf{C}$, $\mathbf{g_k} \sim \mathcal{CN}(0, \mathbf{S})$ is $M \times 1$ speckle vector and τ_k is the texture in the k-th range cell. Vectorization of $\mathbf{C}$ similarly to the target response (2.23) gives $KM \times 1$ vector $\mathbf{c} = \text{vec}(\mathbf{C}^T)$ with elements $\mathbf{c} = [c_0, c_1 \ldots c_{KM-1}]^T$. The clutter response in the k-th range cell is the sub-vector of length M: $\mathbf{c_k} = [c_{kM}, \ldots, c_{(k+1)M-1}]^T$, so $\mathbf{c} = [\mathbf{c_0}^T, \mathbf{c_1}^T, \ldots, \mathbf{c_{K-1}}^T]^T$. In this setting, high-resolution clutter can exhibit continuous variations of the local power from one range cell to another. *Accounting for such clutter power variation within the coherent processing of a migrating target response provide a novel way to exploit clutter spatial*

diversity, as demonstrated in Fig. 2.4. Somewhat similarly, clutter range diversity is exploited in the radar modes with high or medium PRF. There, a target at a long distance competes with the range ambiguous response of different clutter patches in each burst, which allows improving target detection against strong clutter nearby [1].

2.3   Conclusion

The aim of this chapter was to investigate the properties of the radar return signal when the coherently bandwidth of the transmitted waveform is large and provide the adequate models of a moving target and clutter for such a case. Attention has been given to the range-migration phenomenon of moving targets, which allows resolving velocity ambiguities in a single low PRF mode and thus obtain unambiguous estimation of range and velocity in one burst. However, the ambiguity function of such waveform has strong ambiguous sidelobes, which have to be considered in the processing. Moreover, it was established that point-like target assumption and Gaussian clutter model, commonly used in narrowband radars are no longer applicable for the high resolution radars, and should be substituted with the extended target model and compound-Gaussian clutter in the high range resolution mode. These models are demonstrated to provide novel ways to exploit diversity on targets and clutter, which can improve target detection in a heavy clutter scenario, as will be demonstrated in the following chapters.
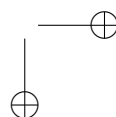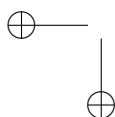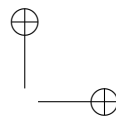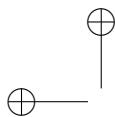
Chapter 3

Performance prediction of migrating target detection in diffuse ground clutter

In this chapter the impact of clutter Doppler spectrum on wideband radar detection performance at the ambiguous-to-clutter velocities is investigated. The power spectrum of ground clutter is modeled as the sum of diffuse and stationary components. The exponential decay model of diffuse clutter spectrum [20] is considered to demonstrate radar detection performance at the ambiguous-to-clutter velocities. The analysis of the waveform parameters and clutter characteristics on target detection performance at the ambiguous-to-clutter velocities is performed. Based on this, some recommendations for waveform design are formulated, which aim at improvement of moving discrimination from diffuse clutter with the wideband waveform. Numerical analysis is validated on the real data measurements, which shows accurate prediction of radar performance at ambiguous-to-clutter velocities using the clutter model with a few parameters.

3.1 Introduction

The main task of surveillance radars is to detect and measure the position and motion parameters of moving targets. Radar clutter is defined as the response from the objects, which are not of interest to the radar mission. Thus, air surveillance radars, aimed at detecting flying objects at low altitude, such as drones, aircraft, cars, etc. consider the reflection from ground objects and clouds as clutter [3, 27]. The perfor-

mance of the surveillance radars operating at centimeter and decimeter wavelength is essentially limited by the reflections from the ground terrain, which is called ground or surface clutter. The reflection of the sounding signal from the stationary objects on the ground is superimposed with the reflections from slowly moving vegetation, such as grass, bushes, trees etc., which results in a widening of clutter Doppler spectrum and poses additional challenges for targets detection. The spectrum of windblown ground clutter is a limiting factor of the radar performance in a wide range of Doppler frequencies. Careful modeling of the clutter spectral characteristics is an essential part of the radar design and performance prediction.

Together with the conventional Doppler processing, modern wideband coherent radars provide additional possibility for clutter rejection, namely, by accounting for the range migration of the moving targets of interest. Range migration is proportional to unambiguous velocity of the target, and therefore it does not exist for stationary or slowly-moving scatterers of the ground surface, recognized by the surveillance radar as clutter. The use of target range-migration for clutter rejection has been proposed in [7, 41, 42]. The idea of that approach is to divide the signal into two delayed bursts, possibly overlapping, and subtract the modulus of coherent processing output of these bursts. The stationary clutter component then will be efficiently rejected, while fast moving targets would produce the "doublet", corresponding to the result of the subtraction of two pulse trains. The procedure, optimized against stationary ground clutter, has limited performance against wind-induced fluctuation of the clutter response.

However, the overall study on the impact of the ground clutter spectrum on target detection at ambiguous velocities is missing. The question to be answered in this chapter is:

- How much ground clutter can be suppressed by accounting for target range migration during coherent processing interval?

The analysis in this chapter therefore aims at investigation of how the waveform parameters and the clutter spectrum affect radar ability to detect targets at various velocities, including those, where the residual ambiguous responses of clutter appear. The analysis is based on the migrating targets model, described in Chapter 2 and satisfying the condition of target presence in the LRRS under test (2.14).

In this chapter it is assumed that clutter can be modeled by complex Gaussian distribution with zero mean, then it is fully characterized by its correlation properties or power spectral density (PSD). If its spectral characteristics are known, it becomes possible to design an optimal Doppler filter for clutter rejection and, therefore, predict detection performance of a model target as a function of its velocity. For the high-resolution radar clutter the assumption of Gaussian clutter model are not applicable anymore. However, the modern models for radar clutter in the HRR

mode allow separating clutter spectral characteristics from the PDF of its magnitude [21]. Detection performance of a target embedded in CG clutter can be obtained by considering jointly the impact of the clutter spectrum and magnitude distribution [3, 21]. So, the analysis given in this chapter on the impact of clutter spectrum on radar performance is applicable for the CG clutter as well, taking into account the additional factors due to deviation of the clutter PDF from Gaussian.

Clutter spectrum modeling has been of interest for radar designers for decades, since detection of moving targets in a system with high dynamic range and low noise floor is essentially clutter limited. The early attempts to fit experimental data with parametric models led to adaptation of the power-law [43] and Gaussian [44] PSDs of the ground clutter. These models were supported by the experimental data of the early radars with low dynamic range, with 35-40 dB clutter peak to noise level. However, they have been found not representative for the clutter recorded by an equipment with a high dynamic range [20]. An extensive analysis of the measured data in different frequency bands led to validation of the exponentially decay clutter power spectrum [20, 45, 46]. Later, the model has been verified theoretically assuming multiscale model of the windblown vegetation [47]. The parameters of the windblown radar ground clutter were demonstrated to be a function of the wind-speed and radar carrier frequency; the empirical equations for clutter PSD prediction have been derived [20]. Moreover, it was observed that apart from the diffuse clutter component, discussed above, a steady component is present in the ground clutter, which results in a direct current (DC) term of the clutter spetrum. The ratio of the DC to diffuse clutter has been also derived empirically for vegetation patches of clutter [20].

In what follows the effect of clutter power spectrum on unambiguous target detection with wideband radar is analyzed. To do that, the model of clutter is introduced in Section 3.2 and the metrics describing radar performance degradation due to the presence of clutter are given in Section 3.3. Comparative analysis of performance degradation due to the presence of clutter for the wideband and the conventional narrowband waveform is presented in Section 3.4. The analysis of real data, performed in Section 3.5, validates the predicted performance degradation of the wideband waveform in the clutter-limited scenario.

3.2 Clutter model

3.2.1 Scenario

The measurement scenario is depicted in Fig. 3.1. Here R_0 defines the distance to the clutter patch, ψ defines grazing angle and θ_{3a} is the azimuth beam width of the
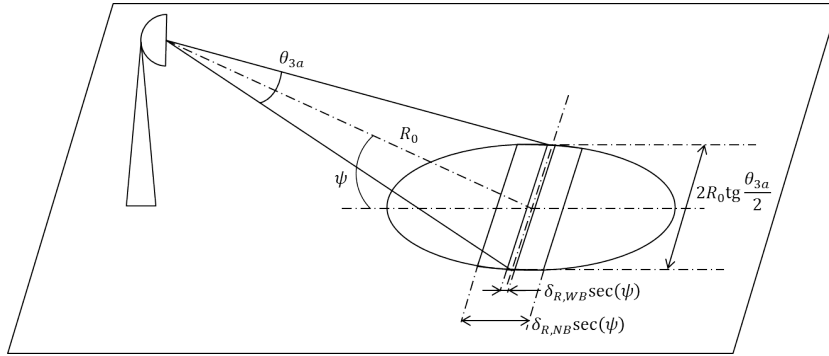
Figure 3.1: Ground area illuminated by a surveillance radar in the pulse limited case

radar antenna. The area of the ground patch, observed by the radar for small θ_{3a}, is:

$$A \approx R_0 \theta_{3a} \delta_R \sec(\psi), \tag{3.1}$$

where δ_R is the radar range resolution, denoted in Fig. 3.1 by $\delta_{R,WB}$ and $\delta_{R,NB}$ for the wideband and the narrowband radar accordingly. In both configurations of the radar, the ground patch is limited by the radar range resolution; the case, in which the radar path is limited by the antenna beamwidth in elevation is not considered here [3, 27].

Clutter response in a range cell arises as a coherent summation of multiple primitive scatterers and therefore modeled by a random process, whose PDF and spectral characteristics depend on the radar parameters and observed scene. When the observed ground patch is large, central limit theorem gives rise to the Gaussian model of clutter, which is fully characterized by its power and correlation properties. The power of clutter response can be obtained from the radar equation in the form:

$$\sigma_c^2 = C_0 \tilde{\sigma}_0 A, \tag{3.2}$$

where C_0 is the constant including all the parameters in the radar equation, except of target RCS. The observed ground surface is characterized by the radar RCS per unit area $\tilde{\sigma}_0$. The observed ground patch therefore has RCS $\tilde{\sigma} = \tilde{\sigma}_0 A$. The value of $\tilde{\sigma}_0$ depends on the radar carrier frequency, terrain type and grazing angle of the terrain; typical levels $\tilde{\sigma}_0$ can be found in various textbooks, e.g. [1].

The further analysis in this chapter compares the performance of the narrowband and wideband radars in the clutter-limited scenario. For this analysis, it is assumed that both radars have equal parameters, except for the range resolution (or bandwidth), for which it is assumed that $\delta_R^{NB} = F \delta_R^{WB}$. Thus, the term C_0 is the same for the two radars under consideration. According to the definition of the RCS per unit

area (3.2) and definition of the clutter patch (3.1), the clutter power per range cell in the wideband radar is F times less of that in the narrowband radar. The reduction of the clutter level per range cell can therefore be exploited to improve detection of target, hidden in clutter.

In this chapter, the clutter in the range cell is modeled by a complex Gaussian random process. This model is verified in the low-resolution radars by the central limit theorem, assuming that the number of primitive scatterers in the observed ground patch is large. The response of clutter in the range cell i is given by zero-mean complex Gaussian random vector $\mathbf{c_i} \sim \mathcal{CN}\left(\mathbf{0}_M, \sigma_c^2 \mathbf{S}\right)$, where σ_c^2 is defined by (3.2), M is the number of coherently processed pulses in the burst. The normalized clutter covariance matrix (CM) $\mathbf{S}$ defines temporary correlation properties of the clutter.

3.2.2 Clutter spectrum

Clutter power spectral density in each range is assumed to have normalized PSD including stationary and diffuse terms [20, 45]:

$$P_{\mathrm{cl}}(f_{\mathrm{d}}) = \frac{r}{r+1}\delta(f_{\mathrm{d}}) + \frac{1}{r+1}P_{\mathrm{ac}}(f_{\mathrm{d}}), \qquad (3.3)$$

where f_{d} if the Doppler frequency in Hz $-F_r/2 < f_{\mathrm{d}} < F_r/2$, $F_{\mathrm{r}} = 1/T_{\mathrm{r}}$, $\delta(\cdot)$ is the delta function and r is the ratio between powers of stationary and diffuse components of the clutter. The normalization is applied such that: $\int_{-F_r/2}^{F_r/2} P_{\mathrm{cl}}(f_{\mathrm{d}})df_{\mathrm{d}} = 1$. The diffuse component has exponential decay PSD:

$$P_{\mathrm{ac}}(f_{\mathrm{d}}) = \frac{\beta\lambda_c}{4}\exp\left(-\frac{\beta\lambda_c}{2}|f_{\mathrm{d}}|\right) \qquad (3.4)$$

with the shape parameter β, depending on wind speed; $\lambda_c = c/f_c$ is the wavelength at the radar carrier frequency.

The normalized clutter correlation function can be defined via FT of (3.3) and can be expressed:

$$r_{\mathrm{st}}(\tau) = \frac{r}{1+r} + \frac{1}{1+r}\frac{(\beta\lambda_{\mathrm{c}})^2}{(\beta\lambda_{\mathrm{c}})^2 + (4\pi\tau)^2}, \qquad (3.5)$$

where τ is the time argument. Modeling of the Doppler spectrum of the received signal is then performed over the slow-time dimension. The slow-time clutter CM $\mathbf{S}$ is a Toeplitz matrix defined by its first column $\mathbf{s}_m = r_{\mathrm{st}}(mT_r)$, $m = 0 \ldots M-1$.

The real clutter can be rarely described by the diffuse or coherent clutter component only. Typically the ratio r lies between 0 and $+\infty$. For a high resolution radar, providing meter or even sub-meter range resolution, the clutter is expected to be less diffuse, so it is expected to have higher values of r. In the limiting case with $r \to +\infty$,

clutter is modeled by a set of discrete scatterers with zero velocity e.g. [28, 48]. That allows to significantly simplify the model with the price of worse data representation, especially for the ground patches with vegetation.

For the wideband waveform analysis clutter spatial correlation in a LRRS is modeled by the Toeplitz CM $\mathbf{D}$ with its first column $\mathbf{d}_k = \exp{(-\gamma k)}, \ k = 0 \ldots K-1$. The value $\gamma = +\infty$ corresponds to uncorrelated over range clutter and $\gamma = 0$ corresponds to fully correlated over range clutter.

3.3   Performance metrics

The performance of the receiver is generally characterized by the detection characteristics of the corresponding detection algorithm. The detector can have different forms, depending on the assumed clutter characteristics and the target fluctuation model, commonly described by the Swerling models [1]. Nevertheless, the detection performance of any detector is known to be non-decreasing function of the target signal-to-noise ratio (SNR) in the noise-limited case, or of the target signal-to-clutter-plus-noise ratio (SCNR) in case of clutter-limited scenario [49].

By the above, a possible approach to evaluate the influence of clutter presence in the scene on radar performance is to evaluate the expected target SCNR at the output of the clutter rejection filter and compare it to the filter output in the noise-limited scenario. This metric is called SCNR loss due to the presence of clutter [27]. The noise limited performance is considered as the benchmark for the given radar parameters. Alternatively, improvement factor of the Doppler filters or its inverse can be used as in [45, 48]. The improvement factor is defined as the ratio of the SCNR at the output of the Doppler processing (application to a migrating target would consider the output of the velocity-based coherent integration) to the SCNR at a single pulse . Both metrics are closely related and often used in the literature together [27]. For the analysis here SCNR loss is considered.

The coherently processed signal in the noise limited scenario for both systems is modeled by vector $\mathbf{y} = \alpha\mathbf{a} + \mathbf{n}$, where $\mathbf{n}$ is the thermal noise vector, $\mathbf{a}$ is the target signature, such that $\mathbf{a}^H\mathbf{a} = M$, α is the complex amplitude, proportional to the target RCS. In the clutter-plus-noise limited scenario $\mathbf{y} = \alpha\mathbf{a} + \mathbf{c} + \mathbf{n}$, where $\mathbf{c}$ is the vector of clutter.

3.3.1   Wideband waveform

The data of the wideband radar is modeled in the LRRS under test composed of K adjacent range cells, satisfying the constraint (2.14). The noise is modeled by $KM \times 1$ zero mean white Gaussian vector with the noise power σ_n^2, so $E\{\mathbf{n}\mathbf{n}^H\} = \sigma_n^2\mathbf{I}_{KM}$. Similarly, the clutter is modeled by $KM \times 1$ zero mean Gaussian vector

with the normalized CM $\mathbf{Q} = \mathbf{D} \otimes \mathbf{S}$, which comprises temporal and spatial CM. The normalization of $\mathbf{Q}$ is such that $\mathbf{Q}_{i,i} = 1, \forall i = 1, \ldots, KM$. Clutter power is modeled by setting σ_c^2 and thus $E\{\mathbf{c}\mathbf{c}^H\} = \sigma_c^2 \mathbf{Q}$.

For the single burst the optimal radar detector is implemented by the whitening matched filter $\mathbf{w}$, which depends on the clutter parameters. Consider the performance metrics of the noise limited scenario and clutter-plus-noise limited scenario. In the noise limited scenario, the detection performance is a function of the target SNR at the output of the matched filter $\mathbf{w}_n = C_0 \mathbf{a}$, where $C_0 \neq 0$ is an arbitrary scale factor:

$$\text{SNR} = \frac{\left|\mathbf{w}_n^H \alpha \mathbf{a}\right|^2}{\mathbf{w}_n^H (\sigma_n^2 \mathbf{I}) \mathbf{w}_n} = \frac{|\alpha|^2}{\sigma_n^2} \mathbf{a}^H \mathbf{a} = \frac{M |\alpha|^2}{\sigma_n^2}. \tag{3.6}$$

In the clutter limited scenario, the detection performance is a function of the SCNR at the output of the whitening filter $\mathbf{w}_{cn} = k_0 (\sigma_n^2 \mathbf{I} + \sigma_c^2 \mathbf{Q})^{-1} \mathbf{a}$, defined as:

$$\begin{aligned}\text{SCNR} &= \frac{\left|\mathbf{w}_{cn}^H \alpha \mathbf{a}\right|^2}{\mathbf{w}_{cn}^H (\sigma_n^2 \mathbf{I} + \sigma_c^2 \mathbf{Q}) \mathbf{w}_{cn}} = |\alpha|^2 \, \mathbf{a}^H \left(\sigma_n^2 \mathbf{I} + \sigma_c^2 \mathbf{Q}\right)^{-1} \mathbf{a} \\ &= \frac{|\alpha|^2}{\sigma_n^2} \mathbf{a}^H \left(\mathbf{I} + \frac{\sigma_c^2}{\sigma_n^2} \mathbf{Q}\right)^{-1} \mathbf{a},\end{aligned} \tag{3.7}$$

where σ_c^2 / σ_n^2 is the clutter-to-noise ratio (CNR). Clearly, the SCNR is bounded from above by the SNR and depends on the target signature $\mathbf{a}$, CNR and clutter correlation properties via $\mathbf{Q}$. Referring to the target model, it is easy to observe that in homogeneous Gaussian clutter SCNR does not depend on the range position of the target. But, similarly to non-migrating target detection, it depends on target velocity. Consequently, the analysis below focuses on the velocity-dependent factors imposed by the presence of clutter. The SCNR can be seen as a product of the signal SNR in a singe pulse $|\alpha|^2 / \sigma_n^2$ and the normalized response of the clutter rejection filter to the target signature at velocity v:

$$F(v) = \mathbf{a}^H(v) \left(\mathbf{I} + \frac{\sigma_c^2}{\sigma_n^2} \mathbf{Q}\right)^{-1} \mathbf{a}(v). \tag{3.8}$$

The performance degradation due to clutter presence in the scene can be characterized by SCNR loss factor, which is defined as the ratio of SCNR in clutter limited scenario to SNR in the noise limited case:

$$\text{L}(v) = \frac{\text{SCNR}(v)}{\text{SNR}(v)} = \frac{\mathbf{a}^H(v) \left(\mathbf{I} + \frac{\sigma_c^2}{\sigma_n^2} \mathbf{Q}\right)^{-1} \mathbf{a}(v)}{\mathbf{a}^H(v) \mathbf{I}^{-1} \mathbf{a}(v)} = \frac{1}{M} \mathbf{a}^H(v) \left(\mathbf{I} + \frac{\sigma_c^2}{\sigma_n^2} \mathbf{Q}\right)^{-1} \mathbf{a}(v). \tag{3.9}$$

3.3.2   Narrowband waveform

The reference radar is assumed narrowband, which implies negligible range-walk within each coherent burst and small target range extent compared to the range resolution. Herein the staggered PRF waveform with $N_s = 4$ staggered PRFs is considered [1]. The staggered ratio is $11 : 16 : 13 : 17$; it gives velocity unfolding factor $n_{av} = 14.25$. The staggered PRIs are therefore $T_r^n|_{n=1,\dots,4} = \left\{ \frac{11}{n_{av}} : \frac{16}{n_{av}} : \frac{13}{n_{av}} : \frac{17}{n_{av}} \right\} T_r$, where T_r is the average PRI on the staggered waveform, equal to the single PRI employed in the wideband radar.

The received signal of the narrowband signal is obtained in a single range cell containing the target, over N_s bursts, which are processed jointly for ambiguities removal. It is assumed that the received signal is processed coherently in each burst an then an "extractor" combines the obtained detections for ambiguity removal. This "extractor" is usually implemented as the "K out of N" rule, applied to the detections in each burst. The performance of the staggered PRF waveform against clutter can be characterized by the average over bursts response of the clutter rejection filter to the target signature:

$$F_{\text{stag}}(v) = \frac{1}{N_s} \sum_{n=1}^{N_s} F_n(v) = \frac{1}{N_s} \sum_{n=1}^{N_s} \mathbf{a}_n^H(v) \left(\mathbf{I} + \frac{\sigma_{cl}^2}{\sigma_n^2} \mathbf{S}_n \right)^{-1} \mathbf{a}_n(v), \qquad (3.10)$$

where the steering vector of the target in each burst is modeled by $\mathbf{a}_n(v) = \exp(j2\pi f_D(v) T_r^n m)$, $m = 0 \dots M_s - 1$, where $f_D = 2v f_c / c$ is the Doppler frequency of the target and M_s is the number of coherently processed pulses in each PRF. The total number of transmitted pulses is therefore $\tilde{M} = M_s N_s$. Accordingly, the normalized slow-time CM in each burst $\mathbf{S}_n$ is the Toeplitz matrix, defined by its first column $\mathbf{s}_m = r_{\text{st}}(m T_r^n)$, see (3.5). Note that the clutter power observed per range cell with the narrowband radar is:

$$\sigma_{cl}^2 = \frac{\delta_R^{\text{NB}}}{\delta_R^{\text{WB}}} \sigma_c^2, \qquad (3.11)$$

which accounts for the different range resolutions of the systems.

The average gain of the target response at the output of the clutter rejection filter (3.10) relates SNR at the output of the Doppler filters to target SNR in one pulse. This metric can be used to define the probability of target detection in each burst and the overall system performance.

For the staggered-PRF waveform the SCNR loss is defined as the average loss in the bursts:

$$\text{L}_{\text{stag}}(v) = \frac{1}{N_s} \sum_{n=1}^{N_s} \text{L}_n(v) = \frac{1}{N_s M_s} \sum_{n=1}^{N_s} \mathbf{a}_n^H(v) \left(\mathbf{I} + \frac{\sigma_{cl}^2}{\sigma_n^2} \mathbf{S}_n \right)^{-1} \mathbf{a}_n(v), \qquad (3.12)$$

which estimates the degradation of system because of the clutter presence in the scene.

Table 3.1: Parameters of considered wideband and narrowband waveforms

Parameters		Narrowband waveform	Wideband waveform
Carrier frequency	f_c	10 GHz	10 GHz
Bandwidth	B	5 MHz	500 MHz
PRI	T_r	1 ms	1 ms
Ambiguous velocity	v_a	15 m/s	15 m/s
Pulses (in all bursts)	$M, \tilde{M}$	64	64

3.4 Simulations

The ability of the radar to detect moving target in presence of ground clutter is compared for two systems:

- Narrowband radar using staggered-PRF waveform;

- A wideband coherent radar operating in a single low-PRF mode.

The noise levels of both radars under consideration are assumed equal, and the clutter power is proportional to the radar range resolution (3.11). The parameters of the wideband and the narrowband radars are listed in Table 3.1. Higher range resolution of the wideband waveform results in 20 dB lower clutter level of the wideband signal compared to the narrowband one. This difference is accounted in all the simulations of this section.

According to the parameters listed in Table 3.1, the maximum unambiguous velocity of the staggered waveform is $v_{\max} = 14.25 v_a = 213.75$ m/s. To coherently process the migrating target at $v_{\max}$, the wideband signal should be coherently integrated over $K = 48$ range cells, as defined by (2.14). The unambiguous range of the wideband waveform is $cT_r/2 = 150$ km; the narrowband waveform provides unambiguous target detection up to the range, defined by the shortest PRI: $cT_r^{\min}/2 \approx 115$ km.

The analysis below evaluates first the impact of the diffuse and coherent clutter components on the system separately, and then the performance in presence of both components is analyzed. Due to the mirror symmetry of the clutter power spectrum and the filter responses of both processing schemes, only the positive velocities are considered.

3.4.1 Diffuse clutter component

Assume $r = 0$ and therefore clutter is represented by the diffuse component only (3.5). The responses of the narrowband and the wideband clutter filters as the function of expected target velocity are shown in Fig. 3.2. In the demonstrated scenario $\beta = 8$, which is a typical value of clutter shape parameter for breezy air [20,45]. The scenario
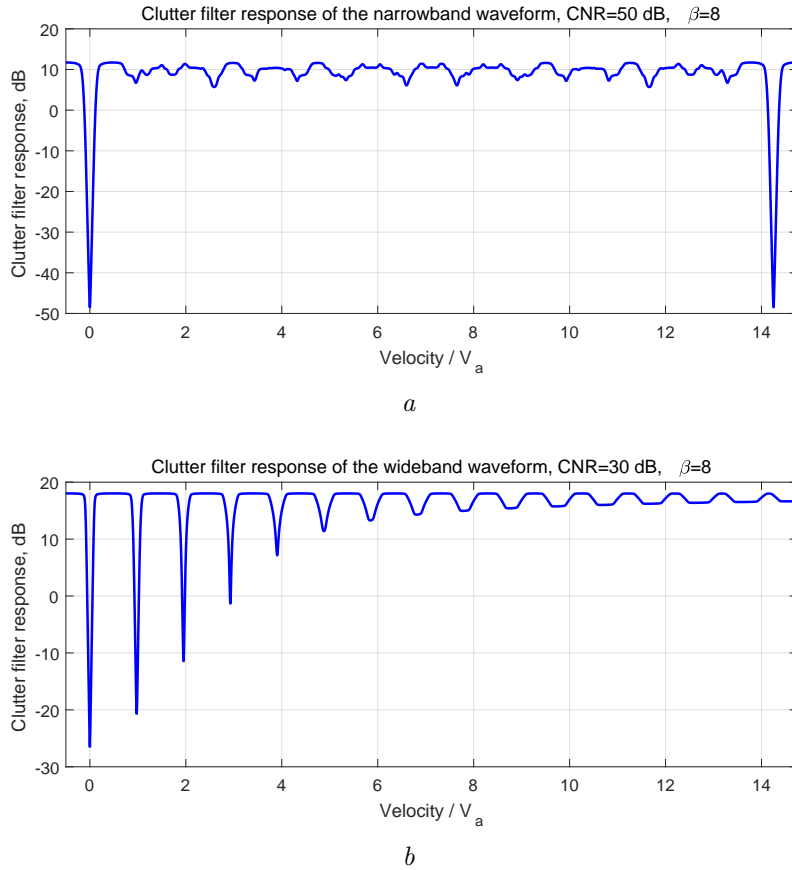
Figure 3.2: Velocity response curve in clutter with $\beta = 8$: a - narrowband (staggered PRF) waveform, CNR = 50 dB; b - wideband (single-low PRF) waveform, CNR = 30 dB.

with strong clutter is considered, in which the wideband waveform provides CNR = 30 dB and the narrowband one yields CNR = 50 dB. For the wideband scenario, clutter is assumed non-correlated in range, $\gamma = +\infty$.

The comparison demonstrates that in presence of strong clutter, the staggered PRF waveform with the appropriate clutter filter provides more uniform response over the velocities below $v_{\max}$. At the same time, the wideband waveform provides about 6 dB better gain for the clutter-free velocities due to longer CPI. Moreover, the wideband processing provides overall better result for high-speed targets (above $v_0 > 4v_a \approx 60$ m/s for the given clutter and radar parameters).

The curves in Fig. 3.2 demonstrate the response of the clutter filter for all possible velocities. To obtain a compact representation of the radar performance around

Figure 3.3: Maximum SCNR loss vs velocity ambiguity for different clutter shape: a - narrowband waveform, CNR = 50 dB; b - wideband waveform, CNR = 30 dB .

Figure 3.4: Maximum SCNR loss vs velocity ambiguity for different CNR, $\beta = 8$: a - narrowband waveform; b - wideband waveform.

ambiguous velocities, the maximum SCNR loss for every velocity ambiguity index is evaluated:

$$L^{max}(n_a) = \min(L(v)), v \in (n_a - 0.5)v_a \ldots (n_a + 0.5)v_a. \qquad (3.13)$$

The maximum SCNR loss vs velocity ambiguity number for the wideband and the narrowband waveform is shown in Fig. 3.3 for three forms of the clutter spectrum shape: $\beta = \{4.8, 8, 12\}$. These values of β are referred in [45] as the typical values for the gale force, breezy and light air conditions accordingly. CNR for both waveforms is the same as was used in the previous simulation. Simulation results shown in Fig. 3.3 demonstrate that performance of the wideband waveform is sensitive to the shape of the clutter spectrum, especially at the first clutter ambiguities. For the high velocities this dependency diminishes and the wideband processing provides lower SCNR loss than the narrowband radar. Widening of the clutter spectrum also reduces the performance of the staggered PRF waveform, albeit uniformly for all ambiguities by a few dBs.

Fig. 3.4 represents the maximum SCNR loss at the velocity ambiguities for different values of the CNR. Clutter spectrum shape is $\beta = 8$ is considered, which
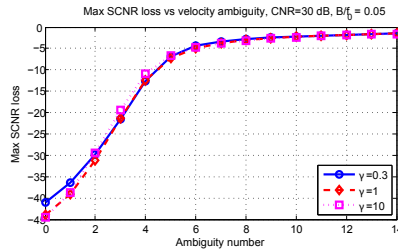
Figure 3.5: Maximum SCNR loss of the wideband waveform vs clutter spatial correlation, $\beta = 8$, CNR = 30 dB

Figure 3.6: Maximum SCNR loss of the wideband waveform vs velocity ambiguity, $\beta = 8$: a - as the function of the coherent bandwidth, $M = 64$; b - as the function of pulses in CPI, $B = 500$ MHz.

corresponds to breezy wind conditions. The SCNR loss of the wideband waveform significantly depends on the CNR at least at the few first velocity ambiguities and diminishes for high speeds. Note, that due to exponentially decay shape of the clutter spectrum, the increase of CNR also widens the Doppler frequency domain, where target detection is clutter limited, rather than noise limited. That is why the curves in Fig. 3.3 and Fig. 3.4 have similar shapes.

Last, the influence of clutter spatial correlation on SCNR loss of the wideband waveform is analyzed. Simulation results, demonstrated in Fig. 3.5, show that clutter spatial correlation has minor impact on the SCNR loss.

Appendix C proves that the bandwidth determines the efficiency of the clutter suppression with the wideband waveform. The numerical analysis in Fig. 3.6, a verifies this conclusion for CNR = 30 dB and breezy wind conditions $\beta = 8$. In fact, the wideband waveform with 10% bandwidth ($B = 1$ GHz) has significant SCNR loss only at the first ambiguous to clutter velocity at breezy wind conditions. The detection performance at higher velocities is superior to the low resolution staggered PRF waveform, when the extra 6 dB gain of longer coherent processing of the wideband waveform is considered. The plot for 1% bandwidth demonstrates non-applicability of clutter suppression by migration when the displacement of the target at ambiguous
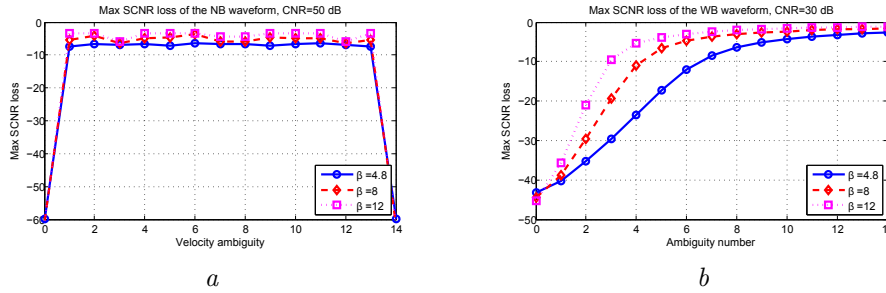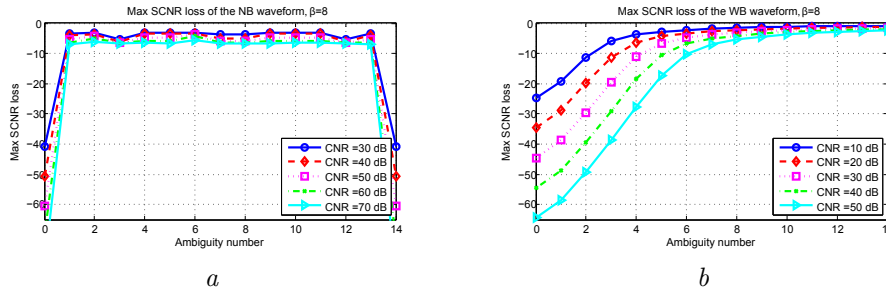
Figure 3.7: Maximum SCNR loss vs velocity ambiguity for different CNR of discrete clutter: *a* - narrowband waveform; *b* - wideband waveform.

velocity during CPI is small compared radar range resolution (for $B/f_c = 0.01$, range migration if $\frac{v_a M T_r}{\delta_R} = \frac{BM}{f_c} = 0.64$ range cells per ambiguity).

The effect of the number of coherently integrated pulses in the wideband burst on the ability to suppress clutter is investigated in Fig. 3.6, *b*. The number of pulses in the burst merely affects the detection performance of targets at ambiguous to clutter velocities in Gaussian clutter. The results agrees well with the conclusion given in Appendix C with the small deviation for $M = 16$, which is the result of poor Doppler resolution in the latter case.

To sum up, the ability of the wideband radar to perform unambiguous detection in diffuse ground clutter strongly depends on the clutter spectral characteristics. Fast radial movement of the target and large coherent bandwidth spreads the Doppler spectrum of the target (before migration compensation), and therefore improve clutter ambiguities suppression. The performance of clutter suppression using target migration is highly efficient against clutter with narrow Doppler spectrum, but has limited improvement against clutter with wide Doppler spectrum. To improve the preference of the wideband coherent radar against clutter, the waveform with the maximum available bandwidth should be employed.

3.4.2 Discrete clutter component

Assume only discrete clutter component is present, so $r \to +\infty$. Clutter distribution is then fully characterized by the CNR and spatial correlation. The analysis, given in Fig. 3.7 shows that DC component has no impact on detection performance at blind velocities for both waveforms, even for large CNR.

Efficient suppression of the DC clutter component is preserved for wide values of the radar parameters M and B, as demonstrated in Fig. 3.8, given non-negligible range-walk of the target exists at the ambiguous velocities. That also explains the efficiency of the migrating target indicator (MiTI) [41, 42] and similar approaches [7],

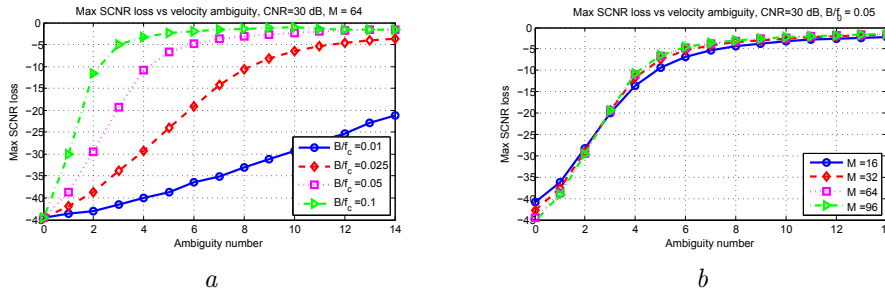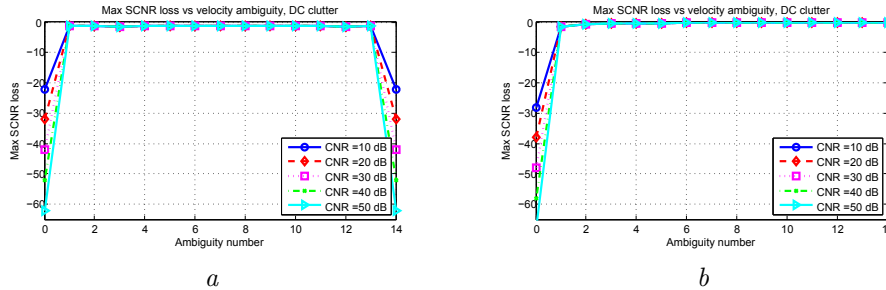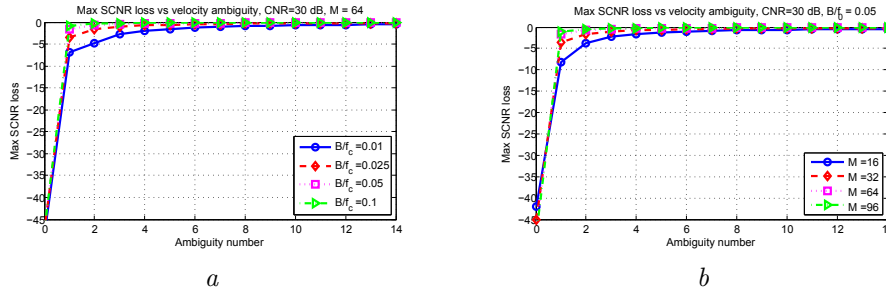Figure 3.8: Maximum SCNR loss of the wideband waveform vs velocity ambiguity in discrete clutter: a - as the function of the bandwidth, $M = 64$; b - as the function of pulses in CPI, $B = 500$ MHz.
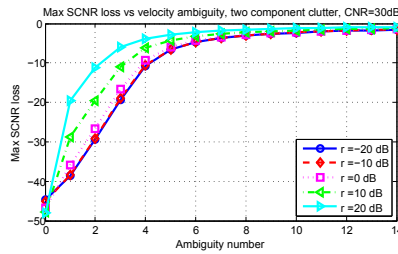
Figure 3.9: Maximum SCNR loss of the wideband waveform vs velocity ambiguity for different power ratio of stationary to diffuse components

demonstrated by simulations with the clutter modeled by discrete scatterers.

3.4.3   Two component clutter spectrum

The analysis above shows that the diffuse and discrete clutter components affects the ability to detect moving targets with wideband waveform in a different manner. Thus, in presence of two component clutter, the power ratio of two components plays an important role. The analysis of the influence of the parameter r on the SCNR loss of the wideband waveform is studied for CNR = 30 dB and $\beta = 8$. Simulation results are presented in Fig. 3.9. For $r \ll 1$, the behavior reminds that of the diffuse clutter case only, while for $r \gg 1$ a significant improvement at the first few ambiguous velocities is observed. For the fixed clutter power, increment of r results in the reduction of the diffuse clutter power and the clutter Doppler spread, which are the limiting factors for unambiguous targets detection with the wideband waveform.

An empirical expression for the ratio r at moderate to LRR (15, 36, 150 m) has been obtained from the analysis of multiple data sets, recorded in different frequency
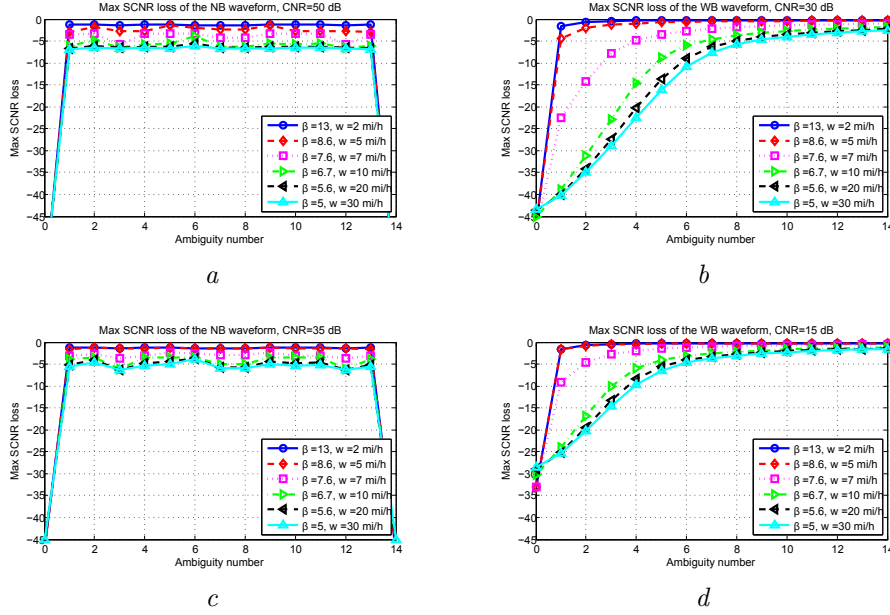
Figure 3.10: Maximum SCNR loss vs velocity ambiguity for different wind speed: *a* - narrowband waveform, CNR = 50 dB; *b* - wideband waveform, CNR = 30 dB; *c* - narrowband waveform, CNR = 35 dB; *d* - wideband waveform, CNR = 15 dB.

bands at MIT Lincoln Laboratory (LL)[20]:

$$10\log_{10}(r) = -15.5\log 10(w) - 12.1\log_{10}(f_c/10^6) + 63.2, \tag{3.14}$$

where w is the wind speed in mi/h[1]. This expression, being supplemented with another empirical formula for the clutter shape parameter [20]:

$$\beta^{-1} = \left(\log_{10}(w) - \log_{10}(2/3^{1.5})\right)\left(20\log_{10}(3)\right)^{-1}, \tag{3.15}$$

allows to predict performance of both wavforms in presence of ground clutter as the function of wind speed and CNR. With the use of (3.15) it can be seen that the values of $\beta = 4.8, 8, 12$ corresponds to the wind speeds $w = 37.4, 6, 2.4$ mi/h accordingly.

For the simulation analysis it is assumed that the ratio r of (3.14) is equal for the wideband and the narrowband waveform. The performance prediction in various wind conditions is shown in Fig. 3.10. There plots *a* and *b* correspond to the high CNR = 50 dB and 30 dB for the narrowband and wideband waveform accordingly; the plots *c* and *d* shows the performance for CNR = 35 dB and 15 dB respectively.

---

[1]In this chapter the wind speed is given in mi/h to follow the model used in the literature, 1 mi/h ≈ 0.45 m/s

The variation of the wind speed has significant impact on the wideband waveform performance and minor on the multi-burst narrowband waveform. When the wind speed is less than 5 mi/h, a target at any velocity can be detected by the wideband waveform with minor losses, the clutter model is close to the set of discrete scatterers.

To sum up, the wideband low-PRF waveform allows unambiguous detection of moving targets in ground clutter, but its performance significantly depends on the wind conditions. Thus, in windy conditions, the detection of moving targets at the first blind velocities can be significantly degraded by the clutter ambiguities. The wider the Doppler spectrum of ground clutter and the higher its CNR, the more loss occurs at the ambiguous-to-clutter velocities. In light wind conditions ($w < 7$ mi/h), detection loss due to presence of clutter is low, and detection with wideband waveform is preferred due to better range and velocity resolution it provides, and the higher gain as a result of longer CPI. The same holds for target detection in urban environment, when the clutter is dominated by the steady state man-made objects.

3.5   Analysis of recorded ground clutter: a case study

In this section, the clutter data recorded with the PARSAX[1] radar on 2 November 2016 is analyzed for possibility of clutter rejection by exploiting target range migration. PARSAX was set to single polarization (VV) high resolution mode, with the sounding chirps of $B = 95$ MHz ($\delta_R = 1.58$ m), which occupies frequency from 3.265 GHz to 3.365 GHz. The PRI is $T_r = 1$ ms. The received data is provided after range compression in fast-time (range cell) / slow-time format. Range compression is performed with Hamming window for range sidelobe reduction. The radar was pointed to azimuth angle 177.04 deg and elevation angle -1.9 deg. The data set consist of 3 data files, recorded within 5 minutes on the same illumination area, but with different attenuation of the transmitted power: 20 dB, 10 dB and 0 dB. From each record 20480 slow-time samples were taken for data analysis, which corresponds to ≈ 20 sec time interval. An additional file has been recorded with turned off transmitter and used for thermal noise estimation. The estimated noise power has been used to normalize the data in the clutter records such that the noise floor is at 0 dB.

The illumination area, represented in Fig. 6.1 is a man-made park to the south of Delft. The data from range cells $1590 \ldots 1639$ recorded with 10 dB attenuation is shown in Fig. 3.11. It represents a line of trees around the range cell 1600 and a block of trees at the range cells $1615 \ldots 1630$, separated by grass fields. At the time of experiment, the trees still had their leaves and the grass was still present in the fields. The meteorological station, placed next to radar (on the rooftop of EWI building),

---

[1]The detailed description of PARSAX radar is provided in Appendix A
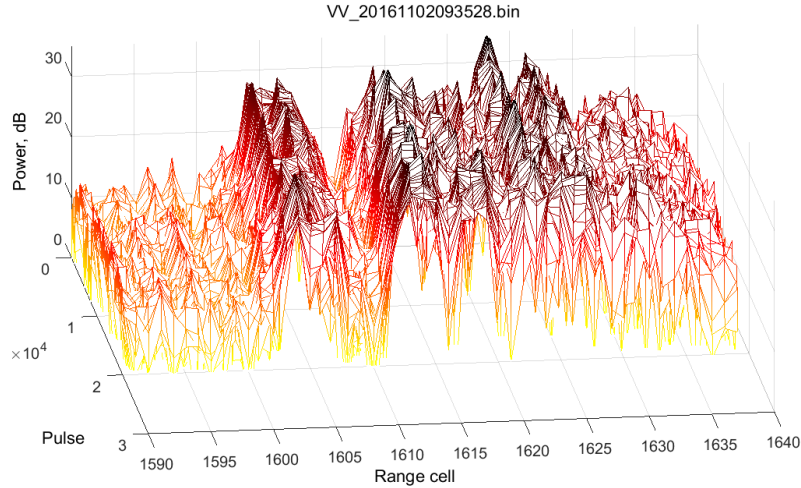
Figure 3.11: Power map of the analyzed clutter data

measured the wind speed equal to 5.8, 6.3 and 6.3 m/s accordingly for the data with attenuation 20 dB, 10 dB and 0 dB accordingly (the meteorological station provides 1 measurements per min). The average wind speed $6.1\text{m/s} \approx 13.7\text{mi/h}$ gives $\beta \approx 6.2$, which corresponds to breezy air condition.

Since the observed clutter has significant power variation and does not satisfy the Gaussian assumption, the analysis below is performed as follows: first, clutter spectrum is estimated from a single range cell. Here the range cells 1618 is selected as a representative range cell for trees clutter (the analysis in the other range cells with trees provides similar results). Second, clutter CM in one range cell is estimated from the time shifted data in the selected range cell and used for SCNR loss estimation using sample covariance matrix (SCM) of the data. Alternatively, the clutter parameters β, r, σ_c^2 are estimated from the data in the range cell under test, assuming $\gamma \to +\infty$, and plugged in the clutter model to obtain model-based prediction of SCNR loss. The alignment of the SCNR loss estimation by two approaches demonstrates how reliable is the clutter model for the considered scenario and how accurately clutter suppression using target migration can be predicted.

To estimate the parameters of the clutter model, sliding window of length $M_1 = 2048$ is applied to $N = 20480$ slow-time samples to form $N - M_1 + 1$ data "snapshots" for clutter auto-correlation estimation over slow-time, normalized such that $\hat{\mathbf{s}}_0 = 1$. Then clutter shape parameters $\theta = \{\beta, r\}$ of (3.5) are estimated from this normalized auto-correlation function with non-linear least squares (NLLS) method,
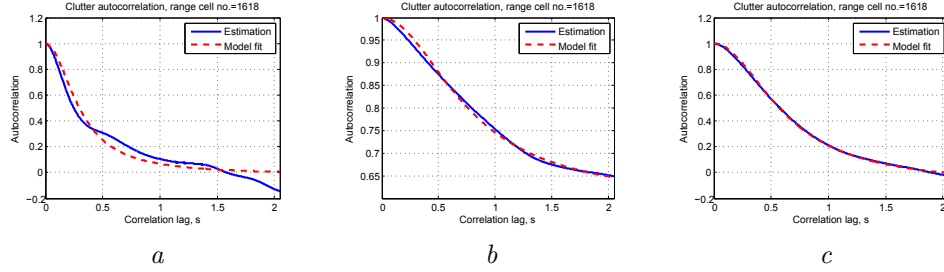
Figure 3.12: Estimated and fitted with the model correlation of the clutter, recorded with attenuation: a - 20 dB; b - 10 dB; c - 0 dB.
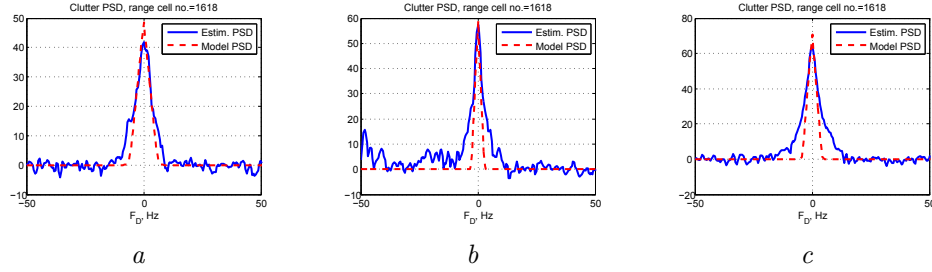
Figure 3.13: Estimated and fitted with the model PSD of the clutter, recorded with attenuation: a - 20 dB; b - 10 dB; c - 0 dB.

Table 3.2: Estimated parameters of the measured data

File name	Att.	Meas. wind speed, m/s	β	Est. CNR, dB	Est. β	Est. r
VV_20161102093629	0	6.3	6.1	35.1	86	0.41
VV_20161102093528	10	6.3	6.1	24.6	89	0.9
VV_20161102093408	20	5.8	6.2	15.2	43	0.31

which minimizes the following function:

$$\theta_{\mathrm{NLLS}} = \arg\min_{\theta} \|\hat{\mathbf{s}} - \mathbf{s}(\theta)\|_2^2. \tag{3.16}$$

Last, to fully specify the model, the CNR is evaluated by solving $\mathrm{CNR} = \sigma_c^2/\sigma_n^2 = \sigma_{c+n}^2/\sigma_n^2 - 1$, where σ_{c+n}^2 is the estimated variance of the data under consideration and $\sigma_n^2 = 1$ since the data has been preliminary normalized by the measured noise floor. Measured and fitted with the model correlation functions of the clutter are shown in Fig. 3.12.

Fitting of the clutter autocorrelation allows better estimation of the DC clutter component compared to the estimation of model parameters from the data PSD [20, 45]. The quality of the model fit is evaluated by comparison of the estimated
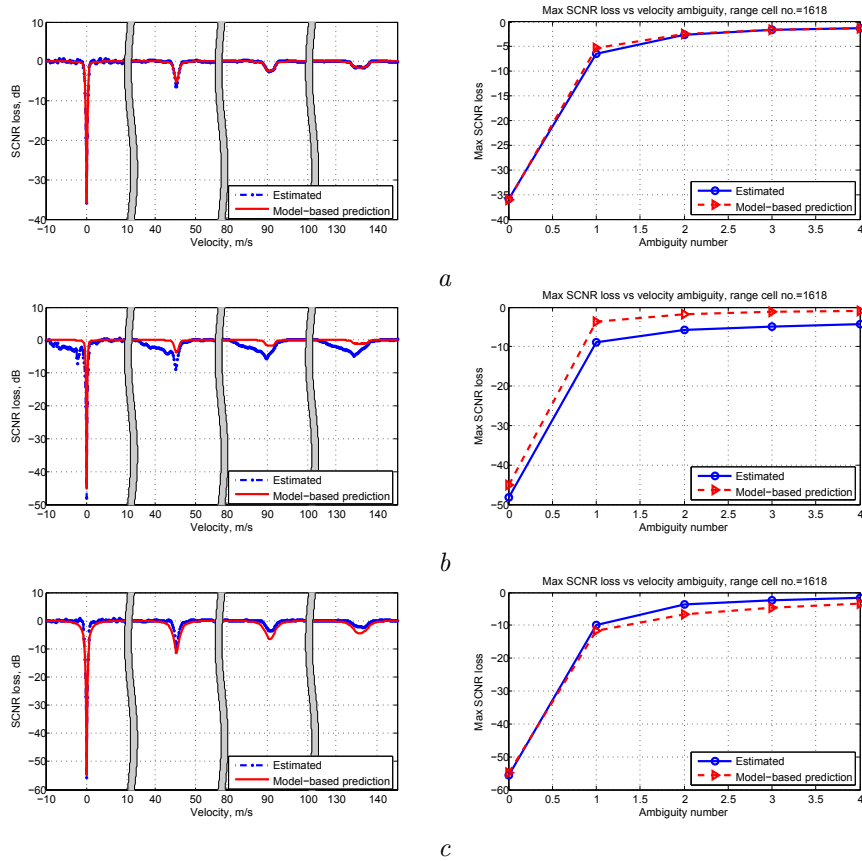
Figure 3.14: SCNR loss vs clutter velocity (left) and max SCNR loss vs clutter ambiguity number: a - 20 dB attenuation; b - 10 dB attenuation; c - 0 dB attenuation.

PSD to the fitted by the model in Fig. 3.13 (zoomed over Doppler axis). The PSD of the data was estimated with the Welch periodogram method from 10 subsets of non-overlapping data of length M_1. Four-sample Blackmann-Harris window was applied to each subset of the data. The final spectrum estimation is the average of 10 obtained spectrum estimates. The proposed approach of model parameters estimation tends to underestimate clutter decay, but keeps reasonable values of the DC component. The estimated parameters of the data are listed in Table 3.2.

The estimated and model-based CM of clutter allow to evaluate prediction of the SCNR loss at the ambiguous to clutter velocities by the SCNR loss curves, considered above. The performance of targets detection at ambiguous to clutter velocities is evaluated for $M = 128$, which gives about 4 range cell migration per ambiguity.

Clutter CM is estimated from the range cell under investigation from $N - M_1 + 1$ data "snapshots", taken from the data over slow-time with the data lag of 1 PRI between them. The estimated SCNR loss is then calculated for different target velocities by (3.9). For the model-based performance prediction, the estimated parameters of the clutter (CNR, β, r) are substituted in the clutter model to build CM $\mathbf{Q}$. In both cases homogeneous and uncorrelated over range clutter was considered, so $\gamma = +\infty$. The SCNR plots vs target velocity and the maximum SCNR loss vs ambiguity number are given in Fig. 3.14 for three values of CNR, mentioned in Table 3.2.

The results show that model-based approach allows accurate SCNR loss prediction at the ambiguous to clutter velocities. Moreover, the processing of real data shows that exploiting target migration allows sufficient clutter suppression for simultaneous detection of fast and slow (due to high Doppler resolution) moving targets. For the CNR values between 15 and 35 dB, the maximum loss at the ex-blind velocities does not exceed 10 dB at moderate weather conditions. Some mismatch between model-based and estimated SCNR loss is observed at the record with 10 dB attenuation. The PSD of the clutter in this record is noticeably asymmetrical around zero velocity and has similar shape around ambiguous velocities. In this case, the performance predicted with the model is too optimistic, since the model does not take into account these high frequency component of the clutter spectrum. The maximal error of predicted performance is about 6 dB at the first ambiguous velocity of the clutter. In the other data records, the model fits the data much better and the loss, predicted with the model, diverges from the estimated one by 3 dB at most.

Note from the results in Table 3.2 that fitting high resolution data with the model gives much larger values of β, and therefore faster clutter decay, than the prediction (3.15) provides for the measured wind speed. That can be due to smaller diffuse clutter component obtained by the HRR of the radar. Also this can be the result of different wind speed with the altitude: the radar and meteorological station are placed about 100 m higher then the trees are.

Similar performance prediction has been found in other range cells containing trees. Therefore, it can be stated that detection performance at the ambiguous to clutter velocities depends on the diffuse clutter parameters. With that parameters estimated from the data, the optimal filter for clutter suppression can be designed and the ability to detect moving targets at the ambiguous to clutter velocities can be accurately predicted.

3.6   Conclusion

In this chapter the effect of clutter Doppler spectrum on radar detection at ambiguous-to-clutter velocities is analyzed. It has been shown that radar detection degradation

at ambiguous-to-clutter velocities is due to diffuse clutter component, which is usually generated by slow movement of vegetation in the observed scene. The reflection from the stationary objects has negligible impact on unambiguous target detection. The improvement against diffuse clutter depends on the coherently processed bandwidth of the sounding signal, but not on its time duration. Therefore, for better moving target separation from clutter, a burst of wideband pulses with maximum available bandwidth should be employed. Analysis of real data records shows good fitness of the estimated loss due to presence of clutter with the one predicted with the model. The model, being a function of CNR and wind speed, can be used for accurate prediction of targets SCNR at ambiguous to clutter velocities. In the presented analysis of recorded data, the loss at ambiguous to clutter velocities because of clutter presence does not exceed 10 dB, which shows great opportunities for unambiguous moving target detection in ground clutter with single low-PRF wideband waveform.
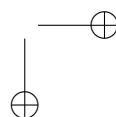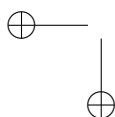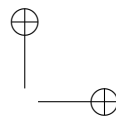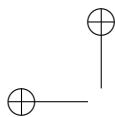
Chapter 4

Resolving velocity ambiguities with the wideband coherent waveform

The ambiguity function of the wideband waveform demonstrates the ability to measure target range and velocity unambiguously in a single long CPI burst with low-PRF. However, in presence of ground clutter and possibly multiple targets in the data set, weak targets can be masked by an ambiguous sidelobe of clutter or of another target. In this chapter, the problem of unambiguous estimation of the observed scene in the range-velocity plane is investigated. The existing techniques are discussed and their limitations are highlighted. High-resolution parametric-free spectrum estimators — Iterative Adaptive Approach (IAA) and Semi-Parametric (sparse) Iterative Covarince-based Estimator (SPICE) — are then proposed for unambiguous estimation of the scene. Their modifications to the case with known clutter spectrum characteristics are also investigated. The proposed techniques have better capabilities for ambiguous sidelobes rejection over the existing methods in various scenarios, as demonstrated by numerical simulations and validated on a real data set.

4.1 Introduction and problem statement

The ambiguity function of a wideband burst, provided in Chapter 2 (see Fig. 2.3), demonstrates the ability to measure target range and velocity without ambiguities in one burst. However, this ambiguity function suffers from strong ambiguous sidelobes, which can bring additional challenges for the data processing in scenarios including

clutter and/or multiple targets: a weak target can be masked by the sidelobe of another, or the sidelobe can produce a false alarm. The estimation of the observed scene from the measured data is considered here in such a way that the impact of the sidelobes is minimized.

Recall that the vectorized data in the LRRS segment under test can be described as (2.28):

$$\mathbf{y} = \sum_{s=1}^{S} \alpha_s \mathbf{a}(\theta_s) + \mathbf{c} + \mathbf{n}, \tag{4.1}$$

where $\theta_s = \{\tau_s, v_s\}$ is the location parameter, representing the range (at the beginning of CPI) and the velocity of the s-th scatterer (point-like target), $\mathbf{a}(\theta_s)$ and α_s denote its steering vector and complex amplitude, S is the total number of scatterers in the observed LRRS.

The vectors $\mathbf{c}$ and $\mathbf{n}$ are independent zero-mean Gaussian vectors $\mathbf{n} \sim CN(\mathbf{0}, \sigma_n^2 \mathbf{I})$ and $\mathbf{c} \sim CN(\mathbf{0}, \sigma_c^2 \mathbf{Q})$, $\mathbf{Q}_{i,i} = 1, \forall i = 1, \ldots, KM$, which model the responses of clutter and noise in the LRRS segment under test respectively. The clutter-plus-noise response is therefore $\mathbf{c} + \mathbf{n} \sim CN(\mathbf{0}, \mathbf{M})$, where $\mathbf{M} = \sigma_n^2 \mathbf{I} + \sigma_c^2 \mathbf{Q}$. In this chapter clutter-plus-noise CM $\mathbf{M}$ is assumed *a priori* known. In practice, it has to be estimated from the reference data (e.g. range cells in the vicinity of the LRRS under test).

For the fixed target and radar parameters, all possible combinations of the target range and velocity, satisfying target presence in the LRRS under test (2.14), define the target parameter space Θ. Sampling the parameter space Θ with sufficiently dense grid allows approximating the received signal with the linear data model:

$$\mathbf{y} = \mathbf{A}\mathbf{x} + \mathbf{c} + \mathbf{n}, \tag{4.2}$$

where $\mathbf{A} = [\mathbf{a}(\theta_0), \ldots, \mathbf{a}(\theta_{N_t N_v - 1})]$ is the library of all possible combinations of the target range and velocity in the LRRS under test; N_t and N_v are the number of grid point in the range and velocity accordingly. Since the parameter space includes the velocities $|v_0| > v_a/2$, the number of grid points is larger than the dimension of the data $N_t N_v > KM$, even if the scene is sampled with the nominal resolution in both range δ_R and velocity δ_v. Therefore the problem of reconstruction of $\mathbf{x}$ from the observed data $\mathbf{y}$ is ill-posed, unless some prior assumption on $\mathbf{x}$ is made. The most straightforward way is to consider that only a few targets (each having a few scattering centers) are present in the scene, which is equivalent to considering that vector $\mathbf{x} = [x_0, \ldots, x_{N_t N_v - 1}]$ is sparse.

In what follows, some recently proposed method for unambiguous reconstruction of the radar scene from the wideband measurements are analyzed and their limitations are summarized in the Table 4.1 at the end of the next section. Then, some

new techniques to resolve velocity ambiguities are proposed in Section 4.3. Their advantages over the existing methods are demonstrated via numerical simulations in Section 4.4 and validated on a real data set in Section 4.5.

4.2   Overview of existing techniques

4.2.1   Wideband Coherent Integration

The standard method for estimation of the radar scene is a Matched Filter, also known as Single-Frequency Least Squares estimator [50] and called wideband coherent integration (CI) [51–53] when applied to the wideband data under consideration. CI is developed assuming that the clutter response can be represented as a finite sum of scatterers. Therefore, CI is obtained via:

$$\hat{x}_i^{\mathrm{CI}} = \frac{\mathbf{a}^H\left(\theta_i\right)\mathbf{y}}{\mathbf{a}\left(\theta_i\right)^H\mathbf{a}\left(\theta_i\right)}, \tag{4.3}$$

performed $\forall i = 0, \ldots, N_t N_v - 1$. The main shortcoming of the CI is the presence of strong ambiguous sidelobes of the observed targets and clutter. As a consequence, separation of real targets from the ambiguous sidelobes is challenging. Moreover, the ambiguous sidelobes of clutter create large interference around the ambiguous velocities, making detection of targets there almost impossible (alike the "blind" velocities of a narrowband radar). The advantage of CI is its computational simplicity, which allows it to be efficiently implemented via Radon [54] or Keystone [52] transforms.

4.2.2   Clairvoyant estimator

The clairvoyant estimator is defined as the maximum likelihood estimation (MLE) with the prior knowledge of the observed scene, which has been proposed in [8]. The interfering signals for estimating complex magnitude of the target at location θ_i are characterized by the CM:

$$\mathbf{K}\left(\theta_i\right) = \sum_{s=1,\theta_s \neq \theta_i}^{S} |\alpha_s|^2 \mathbf{a}(\theta_s)\mathbf{a}^H(\theta_s) + \mathbf{M}, \tag{4.4}$$

where the parameters of all targets in the scene $\alpha_s, \theta_s, \forall s \in S$ and clutter-plus-noise CM $\mathbf{M}$ are assumed known. The structure of $\mathbf{K}\left(\theta_i\right)$ implies mutual independence of the data components in (4.2) [55]. For a single data realization, the clairvoyant estimator is given by:

$$\hat{x}_i^{\mathrm{Clair}} = \frac{\mathbf{a}^H\left(\theta_i\right)\mathbf{K}^{-1}\left(\theta_i\right)\mathbf{y}}{\mathbf{a}\left(\theta_i\right)^H\mathbf{K}^{-1}\left(\theta_i\right)\mathbf{a}\left(\theta_i\right)}. \tag{4.5}$$

Introducing the CM of total interference in the LRRS[1]:

$$\mathbf{R} = \sum_{s=1}^{S} |\alpha_s|^2 \, \mathbf{a}(\theta_s) \mathbf{a}^H(\theta_s) + \mathbf{M} \tag{4.6}$$

and applying matrix inverse lemma to (4.5) for every target location $\theta_i = \theta_s$:

$$\mathbf{a}^H(\theta_s)\, \mathbf{K}^{-1}(\theta_s) = \left(1 + \frac{|\alpha_s|^2 \, \mathbf{a}^H(\theta_s)\, \mathbf{R}^{-1}\mathbf{a}(\theta_s)}{1 - |\alpha_s|^2 \, \mathbf{a}^H(\theta_s)\, \mathbf{R}^{-1}\mathbf{a}(\theta_s)} \right) \mathbf{a}^H(\theta_s)\, \mathbf{R}^{-1}, \tag{4.7}$$

provides the estimator in the form:

$$\hat{x}_i^{\text{Clair}} = \frac{\mathbf{a}^H(\theta_i)\, \mathbf{R}^{-1}\mathbf{y}}{\mathbf{a}(\theta_i)^H \mathbf{R}^{-1}\mathbf{a}(\theta_i)}. \tag{4.8}$$

The extension of the estimator (4.8) for multiple data realizations (snapshots) is straightforward, see [8] for details.

The required knowledge of the targets locations and magnitudes makes the clairvoyant estimator not realizable in practice. However, the clairvoyant estimator will be used as a benchmark in performance assessment of practical estimators. The results obtained with the clairvoyant estimator in [8] demonstrate that velocity ambiguities can be efficiently resolved in a scenario with multiple point-like targets present in the scene, providing significant improvement over CI. A practical estimator then can be made by substitution of $\mathbf{R}$ with its estimation from the received data.

4.2.3 Wideband Capon

Trying to adapt the clairvoyant estimator to a real scenario, where $\mathbf{R}$ is not known, the wideband versions of high-resolution spectral estimators - Capon and APES [56] - have been developed in [8]. Capon and APES exploit multiple realizations of the observed process, obtained from data segmentation, to estimate the CM $\hat{\mathbf{R}}$ and perform spectral estimation.

Applying Capon and APES estimators to the wideband data requires some modification of the original algorithms. The data considered for analysis here is the LRRS under test, presented in the fast-frequency / slow-time domain, with the target signature (2.17). The data is given by the $K \times M$ matrix $\tilde{\mathbf{Y}}$, following the model in (4.1), but not in a vectorized form.

A new data set is generated by applying a sliding window of size $\bar{K} \times \bar{M}$ to the data, as shown in Fig. 4.1, which gives $N_K N_M$ snapshots $\mathbf{z}_{p,q} = \text{vec}\left(\tilde{\mathbf{Y}}_{p,\dots,p+N_K-1, \, q,\dots,q+N_K-1} \right)$, $N_K = K - \bar{K} + 1$ and $N_M = M - \bar{M} + 1$,

---

[1]Matrices $\mathbf{R}$ and $\mathbf{K}$ are defined for each estimator separately and essentially different
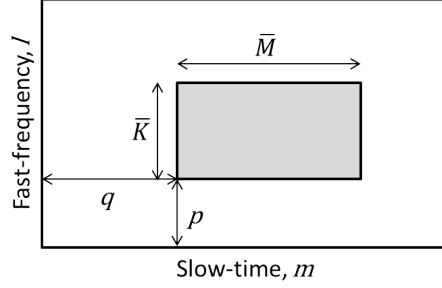
Figure 4.1: Data rearrangement for wideband Capon estimator

$p = 0, \ldots, N_K - 1$, $q = 0, \ldots, N_M - 1$. The signature of a scatterer moving with velocity v_0 and from the initial range position k_0 in the snapshot p, q has the steering vector: $\tilde{\mathbf{a}}_{p,q}(\theta_i) = \exp\left(j2\pi\left(f_r q + \tilde{f}_D p + \tilde{f}_D pq\right)\right)\bar{\mathbf{a}} \odot (\mathbf{b}_p \otimes \mathbf{c}_q)$ with $f_r = -k_0/K$, $\tilde{f}_D = v_0/v_a$, $\mu = B/(Kf_c)$ and $\odot$ denoting the Hadamard product. The first term compensates the initial phase in the snapshot p, q. The steering vector in the snapshot p, q is obtained via the Kronecker-Hadamard multiplication of $\bar{\mathbf{a}}$ - the vectorized steering vector in the snapshot $p = 0, q = 0$ with the term modeling the progressive change of the Doppler and range frequencies from one snapshot to another, modeled by the vectors $\mathbf{b}_p = [1, \exp\left(j2\pi\mu\tilde{f}_D p\right), \ldots, \exp\left(j2\pi\mu\tilde{f}_D p(\bar{M} - 1)\right)]^T$ and $\mathbf{c}_q = [1, \exp\left(j2\pi\mu\tilde{f}_D q\right), \ldots, \exp\left(j2\pi\mu\tilde{f}_D q(\bar{M} - 1)\right)]^T$. The steering vector $\bar{\mathbf{a}}$ corresponds (up to a constant) to the target model (2.17) with the data dimensions set to $\bar{K} \times \bar{M}$. More details can be found in [8].

Wideband Capon (W-Capon) estimator is obtained via:

$$\hat{x}_i^{\text{W}-\text{Capon}} = \frac{\sum_{p,q} \tilde{\mathbf{a}}_{p,q}^H(\theta_i)\hat{\mathbf{R}}^{-1}\mathbf{z}_{p,q}}{\sum_{p,q} \tilde{\mathbf{a}}_{p,q}^H(\theta_i)\hat{\mathbf{R}}^{-1}\tilde{\mathbf{a}}_{p,q}(\theta_i)}, \tag{4.9}$$

with the CM estimated in a standard way:

$$\hat{\mathbf{R}} = \frac{1}{N_K N_M}\sum_{p,q}\mathbf{z}_{p,q}\mathbf{z}_{p,q}^H. \tag{4.10}$$

Wideband version of APES can be obtained in a similar framework as W-Capon and it is not discussed here due to its worse ability to suppress ambiguous sidelobes [8]. Two main assumptions are made to obtain this estimator. First, the snapshots are assumed independent, which is not rigorously correct because of large overlap of the adjacent windows, applied to the data set. Second, the variation of a target signature, modeled by vectors $\mathbf{b}_p$ and $\mathbf{c}_q$ is not considered in the estimation of the matrix $\hat{\mathbf{R}}$.
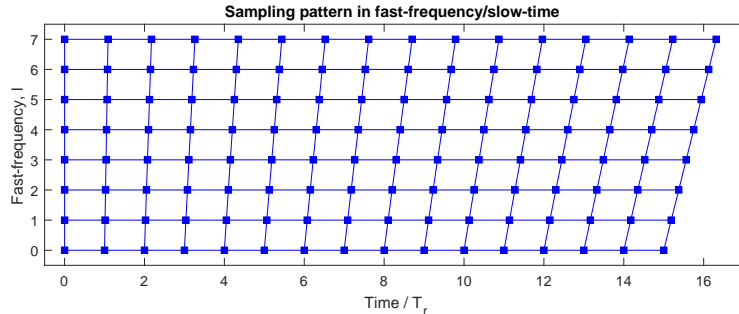
Figure 4.2: Sampling pattern interpretation in the fast-frequency/slow-time

The simulation results in [8] show that the ability of W-Capon to suppress the ambiguous sidelobes of a target significantly depends on its velocity. Thus, the ambiguous sidelobes of clutter, which has low velocity, can be efficiently suppressed. The responses of the fast targets, on the other hand, become smeared and still produce strong sidelobes. Clean-like algorithm has been proposed in [8] to improve the performance for fast targets. However, the advantage it provides is very limited in real scenarios.

4.2.4   Bayesian sparse estimator

An alternative formulation of the problem has been given in [9, 57]. The migrating target model in the fast-frequency / slow-time domain (2.17) can be rewritten as:

$$T_{\text{ff,st}}(l, m) = e^{-j2\pi \frac{k_0}{K} l} e^{j2\pi f_D T_r \left(1 + \frac{B}{K f_c} l\right) m}, \qquad (4.11)$$

which can be seen as a bi-dimensional sinusoid with the range frequency k_0 sampled with the rate $1/K$ and Doppler frequency f_D, sampled with the rate:

$$T_r(l) = \left(1 + \frac{B}{K f_c} l\right) T_r, \quad l = 0, \ldots, K - 1, \qquad (4.12)$$

which is a function of the fast-frequency index l. The corresponding sampling pattern in fast-frequency / slow-time is illustrated in Fig. 4.2.

The problem therefore has been recast to reconstruction of the observed scene from the non-uniformly sampled data. In absence of clutter, the data model (4.2) fits well to the compressive sensing framework, as shown in [9]. However, the reconstruction of the scene is still challenging due to the structure of the measurement or the sensing matrix, used for data representation. Note, that the sampling pattern in Fig. 4.2 comes directly from the data model and so it is not optimized for reliable scene reconstruction.

Table 4.1: Comparison of algorithms for wideband unambiguous estimation

Metric \ Algorithm	Wideband CI	Wideband Capon/APES	Bayesian sparse estimator
Target ambiguities suppression	Poor	Good for slow targets, Poor for fast targets	Good
Clutter ambiguities suppression	Poor	Good	Good, requires special processing
Complexity	Low	Moderate	High
Parameters	No	Sliding window size	Prior PDF of the targets power

A hierarchical Bayesian model is proposed to represent the data and reconstruct the observed scene [9, 57]. The approach has been further extended to account for the possible presence of diffuse clutter, modeled by auto-regressive process [19] or targets with significantly different powers [58]. The stability of the algorithms against possible grid mismatch has been also tackled [59]. The results of simulations and data processing are promising, albeit they require high computational power and some parameters to be set by the user (setting the prior distribution of the targets power).

4.2.5 Summary

The overview of the aforementioned algorithms is summarized in Table 4.1. There it can be seen that the substantial difference between the estimators lies in their robustness to the variation of the scene (noise/clutter limited) and the required adjustment of the model (via parameters or via change of the model itself). The desired solution would require minimal number of parameters from the user and flexibility to the variation of the scene. Moreover, the trade-offs performance vs complexity and performance vs adjustable parameters are clearly visible in the table and essential for the existing techniques.

4.3 Proposed approach

4.3.1 Parametric-free spectrum estimators

The limitations of the aforementioned algorithms can be alleviated with the use of modern spectrum estimation techniques, which satisfy the following criteria:

- Provide robust estimation with a single data snapshot;

- Applicable to non-uniform sampling grid;

- Maintain high spectral resolution to resolve ambiguities;

- Do not require setting parameters, which affect the estimation;

- Robust against possible presence of correlated noise (clutter).

Recently, a few high-resolution parametric-free spectrum estimation algorithms have been proposed, namely Iterative Adaptive Approach (IAA) [15, 16] and Semi-Parametric (sparse) Iterative Covarince-based Estimator (SPICE) [17, 50]. These estimators satisfy the aforementioned criteria and, therefore, are considered for wideband unambiguous reconstruction here.

4.3.2 Iterative Adaptive Approach

Iterative Adaptive Approach (IAA) is a parameter-free data-adaptive spectrum estimator, which has been originally proposed in [15] for source localization. Its ability to remove sidelobes in a data-adaptive manner and its stability against scene variation have been demonstrated in many applications, see e.g. [16, 50, 60].

The idea of IAA is to estimate x_i via minimization of the Weighted Least Squares (WLS) cost function:

$$f_{1,i} = (\mathbf{y} - x_i \mathbf{a}(\theta_i))^H \mathbf{K}^{-1}(\theta_i)(\mathbf{y} - x_i \mathbf{a}(\theta_i)) \tag{4.13}$$

at every location i. The CM $\mathbf{K}^{-1}(\theta_i)$ defines the interference coming from all other locations, considering that as other targets, present in the scene. It is done by assuming the CM with the structure:

$$\mathbf{K}(\theta_i) = \sum_{j=1, j \neq i}^{N_t N_v} |x_j|^2 \mathbf{a}(\theta_j)\mathbf{a}^H(\theta_j) = \mathbf{R} - |x_i|^2 \mathbf{a}(\theta_i)\mathbf{a}^H(\theta_i), \tag{4.14}$$

where

$$\mathbf{R} = \sum_{j=1}^{N_t N_v} |x_j|^2 \mathbf{a}(\theta_j)\mathbf{a}^H(\theta_j). \tag{4.15}$$

Maximizing WLS criteria (4.13) with respect to x_i gives:

$$x_i^{\text{IAA}} = \frac{\mathbf{a}^H(\theta_i)\mathbf{K}^{-1}(\theta_i)\mathbf{y}}{\mathbf{a}(\theta_i)^H \mathbf{K}^{-1}(\theta_i)\mathbf{a}(\theta_i)}. \tag{4.16}$$

Applying matrix inverse lemma to (4.16) as it is done in (4.7) gives:

$$x_i^{\text{IAA}} = \frac{\mathbf{a}^H(\theta_i)\mathbf{R}^{-1}\mathbf{y}}{\mathbf{a}(\theta_i)^H \mathbf{R}^{-1}\mathbf{a}(\theta_i)}. \tag{4.17}$$

Solving (4.17) and (4.15) in iterative manner gives an estimation of $\hat{\mathbf{x}}^{\mathrm{IAA}} = [x_1^{\mathrm{IAA}}, \ldots, x_{N_t N_v - 1}^{\mathrm{IAA}}]^T$. Typically, the number of iterations is set from 5 to 15 to obtain the estimation. The initialization is obtained with the output of CI (4.3), or equivalently $\mathbf{R} = \mathbf{I}$. The CM model (4.15) implies that the number of point-like targets in the scene can be as many as $KM - 1$, leaving one degree of freedom to the noise. This property of the algorithm makes it very stable against different variations of the radar scene, including the presence of multiple possibly extended targets and clutter.

The convergence and the statistical propertied of IAA are still subject of ongoing research. So far, only local convergence of IAA has been proved [16]. That is done by demonstrating that IAA is an approximated MLE of $|x_i|^2$ in multi-target scenario [15, 16].

4.3.3 Semi-Parametric Iterative Covariance-based Estimator

Semi-Parametric (sparse) Iterative Covarince-based Estimator (SPICE) is obtained by iterative minimization of the covariance fitting criterion [17, 18, 50]:

$$f_2 = \left\| \mathbf{R}^{-1/2} \left(\mathbf{y}\mathbf{y}^H - \mathbf{R} \right) \right\|_F^2 = \mathrm{tr} \left(\left(\mathbf{y}\mathbf{y}^H - \mathbf{R} \right)^H \mathbf{R}^{-1} \left(\mathbf{y}\mathbf{y}^H - \mathbf{R} \right) \right)$$
$$= \left\| \mathbf{y} \right\|^2 \mathbf{y}^H \mathbf{R}^{-1} \mathbf{y} + \mathrm{tr} \left(\mathbf{R} \right) - 2 \left\| \mathbf{y} \right\|^2 , \tag{4.18}$$

where the CM $\mathbf{R}$ is defined and initialized by (4.15) similarly to IAA and $\left\| \cdot \right\|_F$ denotes Frobenius norm. According to (4.15), it can be shown that:

$$\mathrm{tr} \left(\mathbf{R} \right) = \sum_{j=1}^{N_t N_v} \left\| \mathbf{a}(\theta_j) \right\|^2 |x_j|^2 = \sum_{j=1}^{N_t N_v} \left\| \mathbf{a}(\theta_j) \right\|^2 p_j, \tag{4.19}$$

with $p_j = |x_j|^2$.

The minimization of f_2 is equivalent to minimization of the function:

$$\min_{\{p_j\}} \mathbf{y}^H \mathbf{R}^{-1} \mathbf{y} + \frac{1}{\left\| \mathbf{y} \right\|^2} \sum_{j=1}^{N_t N_v} \left\| \mathbf{a}(\theta_j) \right\|^2 p_j \tag{4.20}$$

with $\{p_j\} = [p_1, \ldots, p_{N_t N_v}]^T$. It is demonstrated in [17, 18, 50] that the problem in (4.20) is convex and it can be solved by iteratively updating:

$$\hat{p}_j = \frac{\left\| \mathbf{y} \right\|^2}{\sum_{i=0}^{N_t N_v} p_i \left\| \mathbf{a}(\theta_i) \right\| \left| \mathbf{a}^H(\theta_i) \mathbf{R}^{-1} \mathbf{y} \right|} \frac{p_j \left| \mathbf{a}^H(\theta_j) \mathbf{R}^{-1} \mathbf{y} \right|}{\left\| \mathbf{a}(\theta_j) \right\|} \tag{4.21}$$

and the estimated CM defined by (4.15). The iteration (4.21) monotonically decreases the cost function (4.18) and converges globally [18, 50]. Therefore, iterative estimation

can be performed until the change in the next iteration becomes smaller than some predefined value ϵ. When the algorithm has converged, the estimation of $\mathbf{x}$ is obtained similarly to IAA, so by (4.17), but with the last estimation of $\mathbf{R}$ from SPICE [18].

The recent studies [18, 61] demonstrated that SPICE is closely connected to the LAD-LASSO (Least Absolute Deviation, Least Absolute Shrinkage and Selection Operator), which provides more insight in the statistical properties of SPICE.

4.3.4   Clutter-aware estimators

In presence of clutter, which has non-sparse structure, the proposed estimators can experience some performance degradation. A straightforward approach to diminish the impact of clutter consists of two steps: first, filter out clutter with an adaptive filter, which estimates clutter spectral characteristics from the reference data (e.g. range cells in the vicinity of the LRRS under test); second - reconstruct the scene from the whitened data with suppression of targets ambiguities. A similar approach has been recently considered in [62] and solved with the covariance-aware version of LASSO, hence with the a random sensing matrix, — the assumption, which cannot be satisfied with the wideband data model, considered here. An alternative approach, investigated here, consists of incorporation of clutter correlation properties into the WLS criterion of IAA (4.13) and into the covariance fitting criterion of SPICE (4.18).

Assume that clutter-plus-noise CM $\mathbf{M}$ is given. Denote the received data and a steering vector of a target after whitening transform by:

$$
\begin{aligned}
\mathbf{b}\left(\theta_i\right) &= \mathbf{M}^{-1/2}\mathbf{a}\left(\theta_i\right); \\
\mathbf{z} &= \mathbf{M}^{-1/2}\mathbf{y},
\end{aligned}
\tag{4.22}
$$

and rewrite IAA and SPICE criteria for the whitened data set.

IAA

The WLS criterion of IAA (4.13) for the data (4.22) is written as:

$$
\begin{aligned}
g_{1,i} &= \left(\mathbf{z} - \tilde{x}_i\mathbf{b}\left(\theta_i\right)\right)^H \tilde{\mathbf{K}}^{-1}\left(\theta_i\right)\left(\mathbf{z} - \tilde{x}_i\mathbf{b}\left(\theta_i\right)\right) \\
&= \left(\mathbf{y} - \tilde{x}_i\mathbf{a}\left(\theta_i\right)\right)^H \mathbf{M}^{-1/2}\left(\sum_{j=1,j\neq i}^{N_t N_v} |\tilde{x}_j|^2 \, \mathbf{b}\left(\theta_j\right)\mathbf{b}^H\left(\theta_j\right)\right)^{-1} \mathbf{M}^{-1/2}\left(\mathbf{y} - \tilde{x}_i\mathbf{a}\left(\theta_i\right)\right) \\
&= \left(\mathbf{y} - \tilde{x}_i\mathbf{a}\left(\theta_i\right)\right)^H \tilde{\mathbf{K}}^{-1}\left(\theta_i\right)\left(\mathbf{y} - \tilde{x}_i\mathbf{a}\left(\theta_i\right)\right) = f_{1,i},
\end{aligned}
\tag{4.23}
$$

so it is equivalent to the objective function of IAA without whitening transform. Therefore, incorporation of clutter correlation properties does not modify the IAA estimator.

SPICE

Applying the SPICE criteria (4.18) to the data set (4.22) gives:

$$g_2 = \left\| \tilde{\mathbf{R}}^{-1/2} \left(\mathbf{z}\mathbf{z}^H - \tilde{\mathbf{R}} \right) \right\|_F^2 = \mathbf{z}\mathbf{z}^H \mathbf{z}^H \tilde{\mathbf{R}}^{-1} \mathbf{z} + \mathrm{tr}\left(\tilde{\mathbf{R}} \right) - 2\mathbf{z}\mathbf{z}^H, \qquad (4.24)$$

where

$$\tilde{\mathbf{R}} = \sum_{j=1}^{N_t N_v} |\tilde{x}_j|^2 \, \mathbf{b}(\theta_j)\mathbf{b}^H(\theta_j) = \mathbf{M}^{-1/2} \left(\sum_{j=1}^{N_t N_v} \tilde{p}_j \mathbf{a}(\theta_j)\mathbf{a}^H(\theta_j) \right) \mathbf{M}^{-1/2}$$
$$= \mathbf{M}^{-1/2}\mathbf{R}\mathbf{M}^{-1/2}. \qquad (4.25)$$

Equivalently, the function to be minimized is:

$$g_3 = \mathbf{z}^H \tilde{\mathbf{R}}^{-1} \mathbf{z} + \sum_{j=1}^{N_t N_v} \frac{\mathbf{b}^H(\theta_j)\mathbf{b}(\theta_j)}{\mathbf{z}^H\mathbf{z}} \tilde{p}_j$$
$$= \mathbf{y}^H \tilde{\mathbf{R}}^{-1} \mathbf{y} + \frac{1}{\mathbf{y}^H\mathbf{M}^{-1}\mathbf{y}} \sum_{j=1}^{N_t N_v} \mathbf{a}^H(\theta_j)\mathbf{M}^{-1}\mathbf{a}(\theta_j)\tilde{p}_j. \qquad (4.26)$$

The cost function (4.26) has similar structure to that in (4.20), except of the weights applied to p_j, and therefore can be solved similarly via iteration:

$$\hat{\tilde{p}}_j = \frac{\mathbf{y}^H\mathbf{M}^{-1}\mathbf{y}}{\sum_{i=0}^{N_t N_v} \tilde{p}_i \sqrt{\mathbf{a}^H(\theta_i)\mathbf{M}^{-1}\mathbf{a}(\theta_i)} \, |\mathbf{a}^H(\theta_i)\mathbf{R}^{-1}\mathbf{y}|} \frac{\tilde{p}_j \left| \mathbf{a}^H(\theta_j)\mathbf{R}^{-1}\mathbf{y} \right|}{\sqrt{\mathbf{a}^H(\theta_j)\mathbf{M}^{-1}\mathbf{a}(\theta_j)}}. \qquad (4.27)$$

Hereinafter the estimator (4.27) is referred to as SPICE-W.

4.4 Simulations

In this section the performance of the proposed estimators is evaluated and compared to the existing approaches via numerical simulations.

4.4.1 Settings

The effectiveness of the algorithms is analyzed in terms of their ability to suppress the ambiguous sidelobes and preserve the target response at the correct location in various scenarios. For simulations, the parameters of the radar are fixed to the values given in Table 4.2.

Moreover some processing parameters are set fixed for all the estimators: the oversampling in range and velocity are $n_t = 4$ and $n_v = 4$ accordingly, compared

Table 4.2: Simulated radar parameters

Parameter		Value
Carrier frequency	f_c	10 GHz
Bandwidth	B	1 GHz
PRI	T_r	1 ms
Ambiguous velocity	v_a	15 m/s
Pulses	M	32
Range cells in LRRS	K	8

to the corresponding resolutions of the waveform. The number of range cells in the LRRS under test is set to $K = 8$ to satisfy the condition on the maximum velocity (2.14) for $v_{max} = 32$ m/s. Thus, the number of range bins in the estimated image $\hat{\mathbf{X}}$ is $N_t = n_t K = 32$ and the number of velocity bins is $N_v = 2\lceil n_v M v_{max}/v_a \rceil + 1 = 561$.

W-Capon is implemented with $\bar{K} = 3K/8 = 3$ and $\bar{M} = 3M/8 = 12$. IAA is obtained with the fixed number of iterations: $I_{\text{IAA}} = 10$. SPICE is run until the stopping criterion $||\hat{\mathbf{x}}^i - \hat{\mathbf{x}}^{i-1}||^2/||\hat{\mathbf{x}}^i||^2 < \epsilon, \quad \epsilon = 10^{-4}$ is satisfied, or the maximal number of iterations $I_{\text{SPICE}}^{\max} = 50$ is reached.

To provide some insight into the behavior of the estimators in typical scenarios, their performance is evaluated in two scenarios:

- Multiple point-like targets in white noise;

- Multiple point-like targets in clutter (colored noise).

Simulated scenarios are demonstrated in Fig. 4.3 and Fig. 4.9 below, followed by detailed explanations.

The obtained estimation of $\hat{\mathbf{x}}$ is rearranged back into the matrix $\hat{\mathbf{X}} \in \mathbb{C}^{N_t \times N_v}$ and the estimated range-velocity map is demonstrated below. For better visibility of the ambiguous sidelobes suppression 1D plots are added, which show the maximal over range response for every velocity cell, namely $h(v) = \max_{t \in [0, N_t-1]} \left| \hat{\mathbf{X}}_{t,v} \right|$.

4.4.2   Noise-limited case

In the noise limited scenario $\mathbf{M} = \sigma_n^2 \mathbf{I}$, and Fig. 4.3 represents the post-processing SNR of the targets:

$$\text{SNR}_s = \frac{M|\alpha_s|^2}{\sigma_n^2}. \tag{4.28}$$

Simulation results in the noise-limited scenario are demonstrated in Fig. 4.4 - 4.8 for one random realization of the data.

The range-velocity map and the velocity profile of the CI, plotted in Fig. 4.4, illustrate the shortcomings of this method: multiple ambiguous sidelobes, present in the estimated scene, makes the estimation of targets locations and their number difficult. Moreover, two targets separated by one ambiguity (a case which can rarely happen in reality, but interesting for simulation analysis) create mutual interference to one another. If the targets have different powers, the weak target will be masked by the presence of a strong one — the situation, not desirable in practice.

The result of the Clairvoyant estimator, depicted in Fig. 4.5, shows that in the noise-limited scenario the ambiguities can be efficiently resolved. The estimate of the W-Capon, demonstrated in Fig. 4.6, suffers from the sidelobes of the fast targets, while the sidelobes level of the target at moderate velocity ($v_0 = v_a$) is lower than that of CI. This demonstrates velocity dependence of W-Capon, mentioned above.

The estimations of the scene, obtained with IAA and SPICE are presented in Fig. 4.7 and Fig. 4.8 accordingly. These algorithms provide accurate estimations of the scene with efficient suppression of ambiguous sidelobes. The noise-like response, observed in IAA estimation is lower than the actual noise floor. Such a result has been noticed in the other studies (e.g. [18]) and was explained there as capturing a fraction of the noise power in each bin of the grid. The IAA estimate is dense, so all elements are non-zero, but rather small. SPICE, on the other hand, provide sparse estimation with multiple elements of $\hat{\mathbf{X}}$ equal to zero or approaching it with the numerical precision. In the noise limited scenario SPICE-W is equivalent to SPICE and therefore not considered herein.

In summing up the simulation results, it is noted that the proposed non-parametric high-resolution spectrum estimators - IAA and SPICE - provide better estimation than the existing approaches in the noise limited scenario.
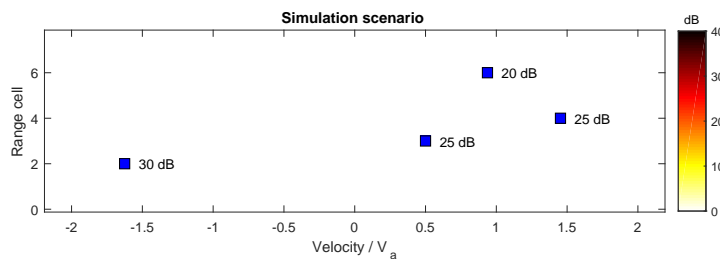
Figure 4.3: Simulation scenario in the noise-limited case
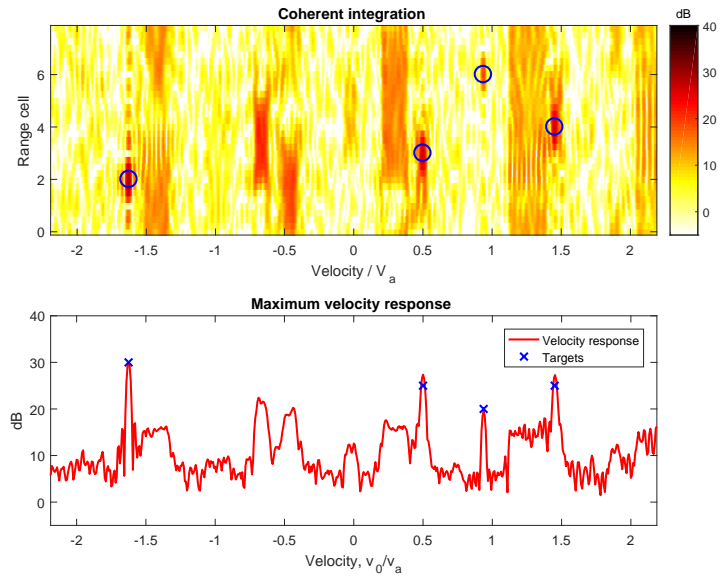
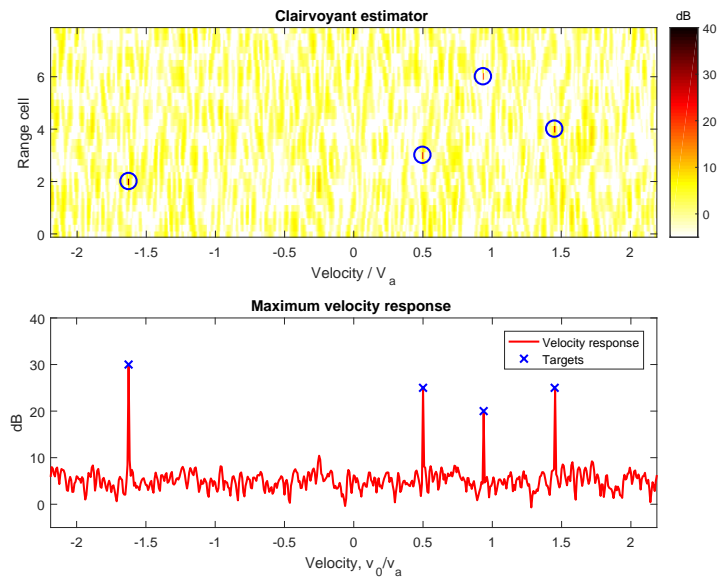Figure 4.4: Wideband CI in the noise-limited scenario

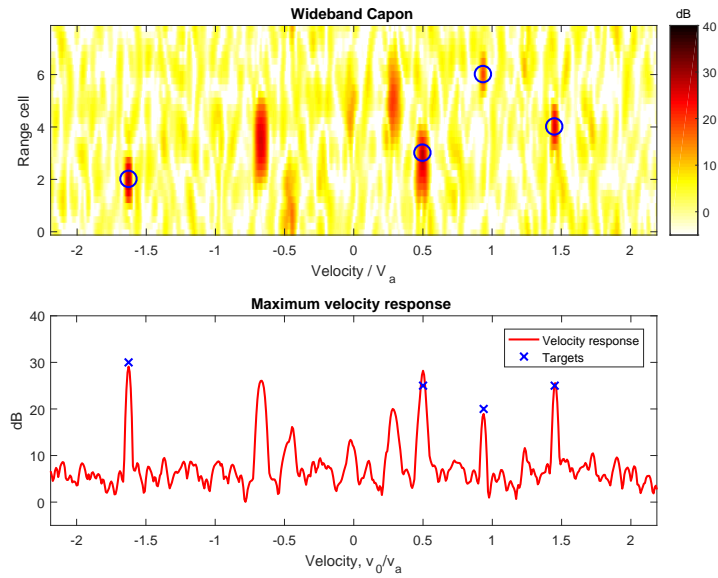Figure 4.5: Clairvoyant estimator in the noise-limited scenario

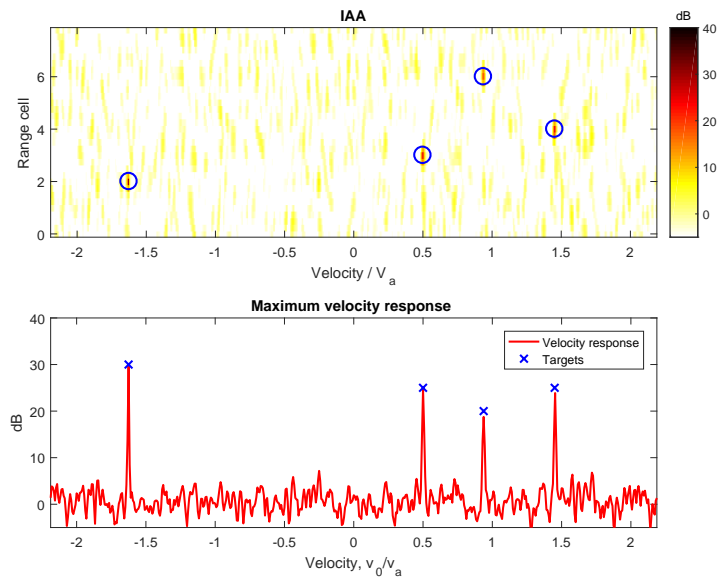Figure 4.6: W-Capon in the noise-limited scenario

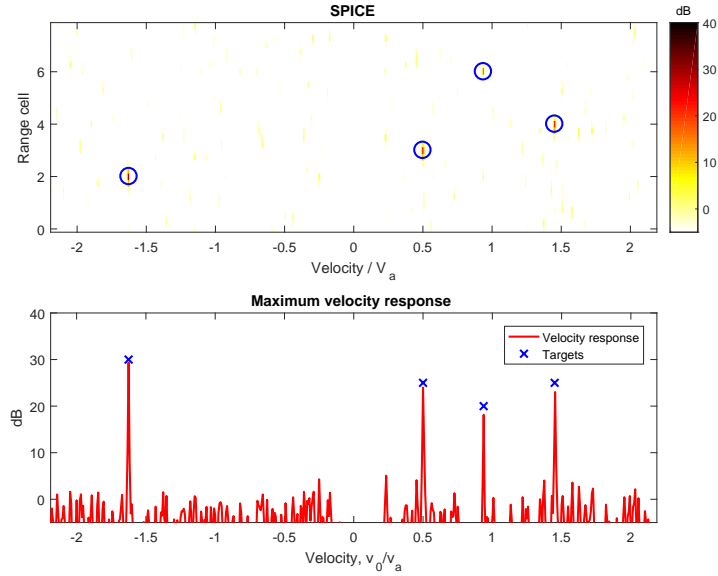Figure 4.7: IAA estimator in the noise-limited scenario

Figure 4.8: SPICE estimator in the noise-limited scenario

4.4.3 Clutter-limited case

In these simulations, uncorrelated over range clutter with exponential decay Doppler spectrum[1] ($\beta = 12$, $r = 0$) and CNR $= \sigma_c^2/\sigma_n^2 = 20$ dB is considered. Fig. 4.9 shows clutter PSD as a background and the post-processing SCNR of the present targets:

$$\text{SCNR}_s = |\alpha_s|^2 \mathbf{a}^H(\theta_s)\mathbf{M}^{-1}\mathbf{a}(\theta_s), \qquad (4.29)$$

where θ_s is the location parameter of the s-th target. In the velocity profiles, targets' SNRs (4.28) are marked.

The estimates of the scene in the clutter-limited case are given in Fig. 4.10 - 4.15. The result of wideband CI, shown in Fig. 4.10, suffers from the strong ambiguous sidelobes of both clutter and targets. The ambiguous sidelobes of clutter, which are present in all the range cells, generate the "blind" velocities, similarly to what usually happens with a narrowband radar. The target at the velocity $v_s = 14m/s \approx 0.94v_a$ appears hidden in the ambiguous sidelobe of clutter and cannot be distinguished from the latter.

The clairvoyant estimator significantly reduces the ambiguous sidelobes of clutter, but does not completely remove them (see Fig. 4.11). Some residuals of the ambiguous

---

[1]The details about exponential decay clutter spectrum are given in Chapter 3
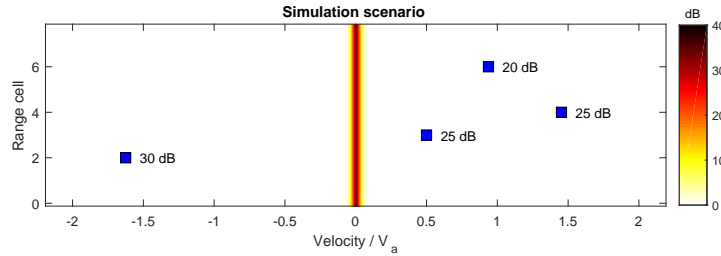
Figure 4.9: Simulation scenario in the clutter-limited case

sidelobes are present around the velocities $\pm v_a, \pm 2 v_a$. This result demonstrates that some limitations for unambiguous proceeding in presence of clutter exist. With the clairvoyant estimator, the target at velocity $v_0 = 14 m/s \approx 0.94 v_a$ becomes visible against the ambiguous sidelobe of clutter. The ambiguous sidelobes of the other targets are completely removed, similarly to the noise-limited scenario.

The estimate obtained with W-Capon (Fig. 4.12), demonstrates its ability to efficiently suppress the ambiguous sidelobes of clutter, up to the level obtained with clairvoyant estimator. However, the targets create high ambiguous sidelobes, which makes distinction of real targets from their ambiguous sidelobes difficult.

The result of scene estimation with IAA is shown in Fig. 4.13. Ambiguous residuals of clutter are comparable to that of the clairvoyant estimator. The targets in the clutter-free regions are correctly estimated and their sidelobes are removed. The target at velocity $v_0 \approx v_a$ is visible against clutter, its magnitude is underestimated by a few dBs. The performance for the target at the clutter ambiguity is limited, but improved in comparison to the existing techniques.

SPICE provides the estimation of the scene (see Fig. 4.14) very similar to result of the IAA, except for more sparse representation of the noise-limited part of the scene. The ambiguous residuals of clutter have higher level than that of the clairvoyant estimator or IAA and remain the limiting factor for unambiguous processing.

The result of the covariance-aware SPICE is demonstrated in Fig. 4.15. In the velocity profile of Fig. 4.15, SCNRs of the present targets are shown. SPICE-W provides a sparse scene estimation with the targets peaks at the correct locations and around zeros velocity for clutter. The recovered clutter response around zero velocity does no create a problem, as any detection at velocity below some threshold can be simply ignored. This result demonstrates that the clutter-aware estimator is preferable to the other techniques in clutter-limited scenario.
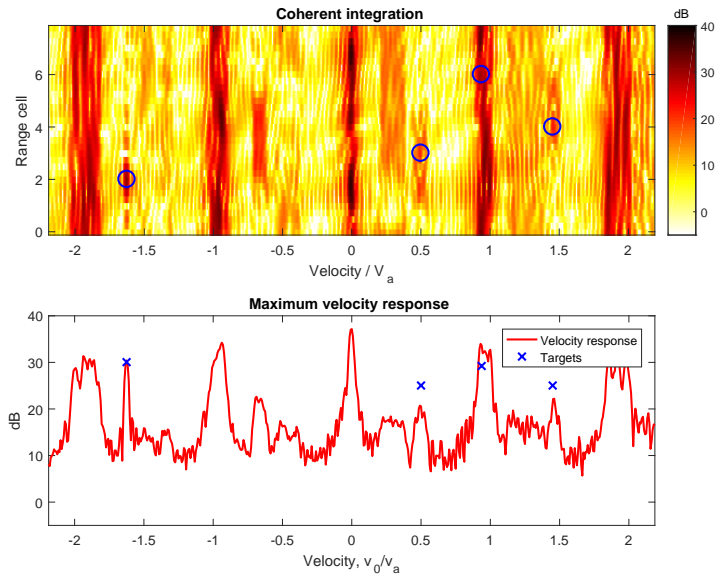
Figure 4.10: Wideband CI in the clutter-limited scenario
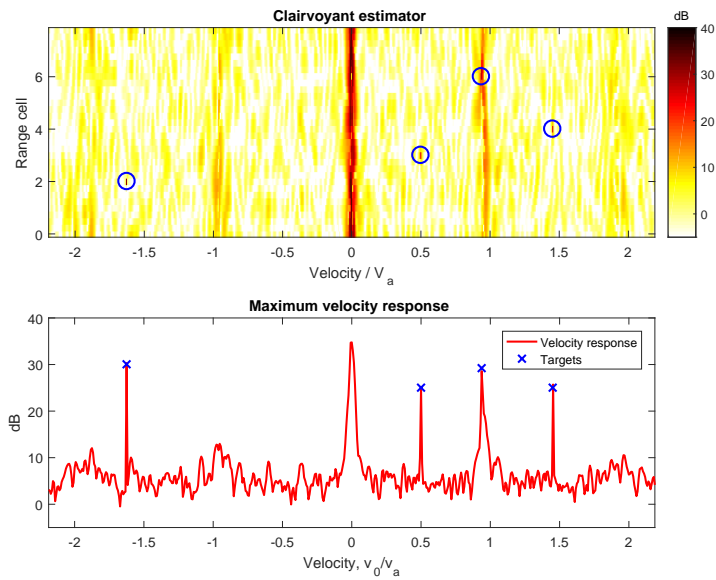

Figure 4.11: Clairvoyant estimator in the clutter-limited scenario

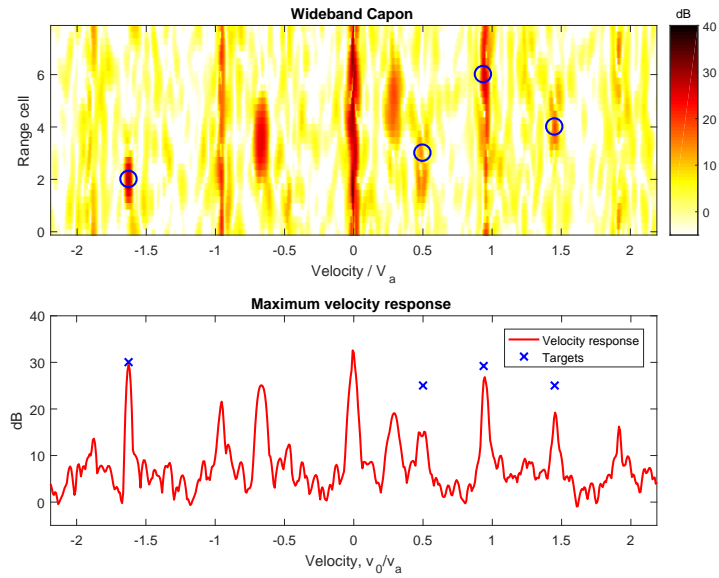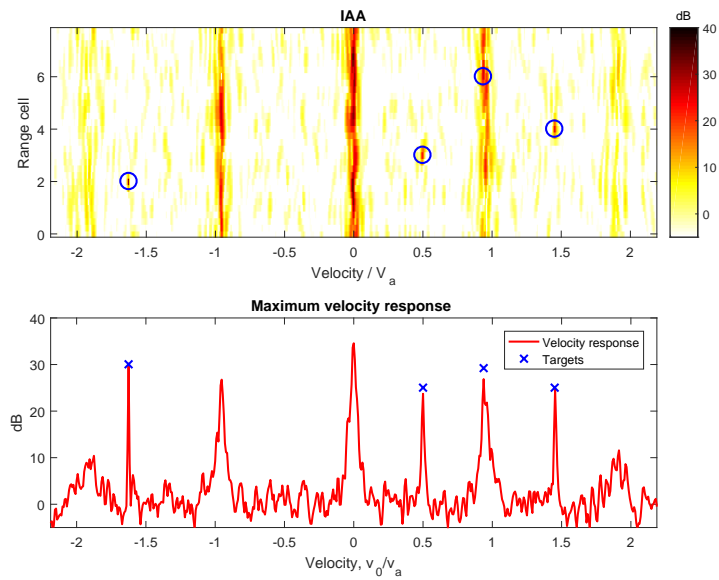Figure 4.12: W-Capon in the clutter-limited scenario

Figure 4.13: IAA estimator in the clutter-limited scenario
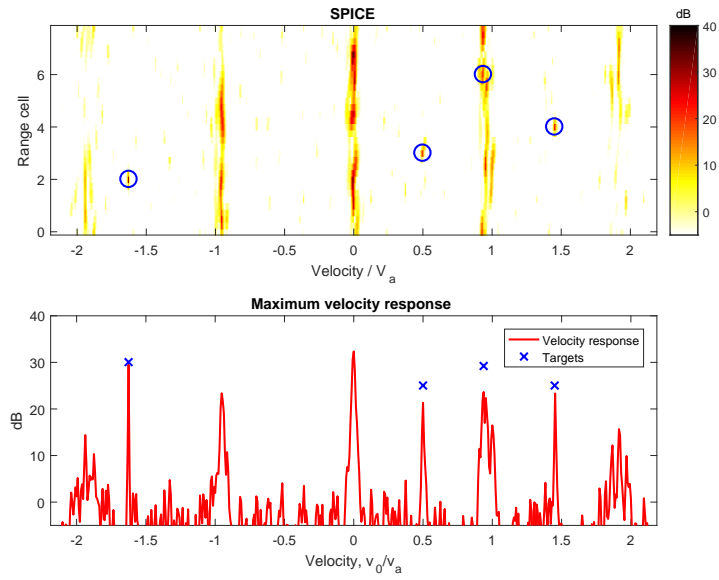
Figure 4.14: SPICE estimator in the clutter-limited scenario
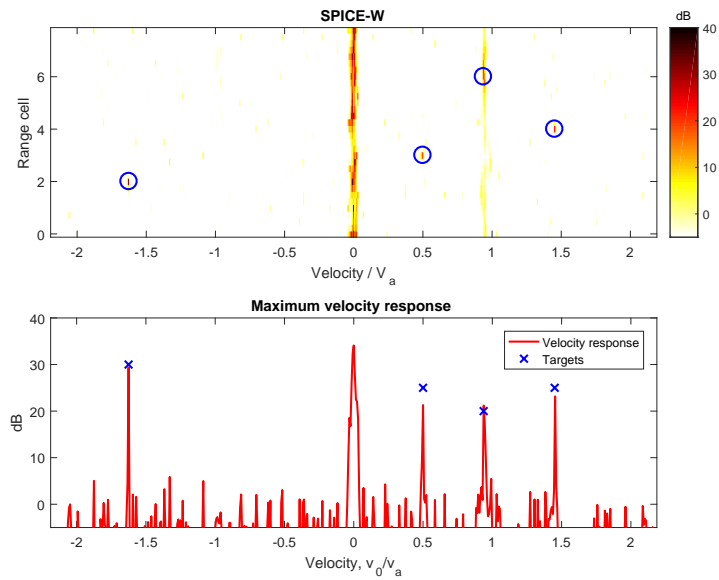

Figure 4.15: SPICE-W estimator in the clutter-limited scenario

Table 4.3: PARSAX waveform parameters

Parameter		Value
Carrier frequency	f_c	3.265 GHz
Bandwidth	B	95 MHz
PRI	T_r	1 ms (0.5 ms)
Ambiguous velocity	v_a	45 m/s (22.5 m/s)
Pulses	M	64
Range cells in LRRS	K	10

4.5 Experimental validation

The proposed algorithm has been tested on experimental data from PARSAX radar collected in November, 2014. The waveform parameters are summarized in Table 4.3; the detailed description of PARSAX radar is provided in Appendix A. The observed scene is A13 highway between the Hague and Rotterdam. The measurement scenario is similar to the one described in [53].

4.5.1 Targets at the noise-limited velocities

Consider the standard PARSAX mode with $T_r = 1$ ms, which gives $v_a \approx 45$ m/s. The observed scene contains the highway with a speed limit of 100 km/h ≈ 28 m/s $\approx 0.6v_a$. Therefore, all targets are observed at velocities below the first clutter ambiguity, so in the noise-limited region.

Consider $M = 64$ pulses in a burst, which gives about 2 range cell migration per velocity ambiguity $v_a \approx 45$ m/s. The number of range cells in the LRRS is set to $K = 10$. Since no target truth is available in advance, the output of the wideband CI with $M_{\mathrm{ref}} = 128$ pulses is used as a reference, given in Fig. 4.16. Therein two targets can be recognized at velocities $v_1 \approx -18$ m/s and $v_2 \approx -23$ m/s; also a weak target at $v_3 \approx 15$ m/s can be observed.

The output of wideband CI is depicted in Fig. 4.17. The sidelobes of clutter and targets raised compared to Fig. 4.16 due to shorter CPI and can be interpreted as other cars, moving in the opposite direction. Similar to the numerical simulations, CI suffers from the strong ambiguous sidelobes of clutter and targets, making it difficult to distinguish between correct responses and false ones.

The estimations obtained with IAA and SPICE are shown in Fig. 4.18 and Fig. 4.19 accordingly. Both IAA and SPICE significantly suppress the ambiguous responses of the targets and reduce the ambiguous sidelobes of clutter by about 15-20 dBs. The clutter residuals at ambiguous velocities ($v \approx \pm v_a$) are lower for IAA than for SPICE by a few dBs, similar to the simulation results.
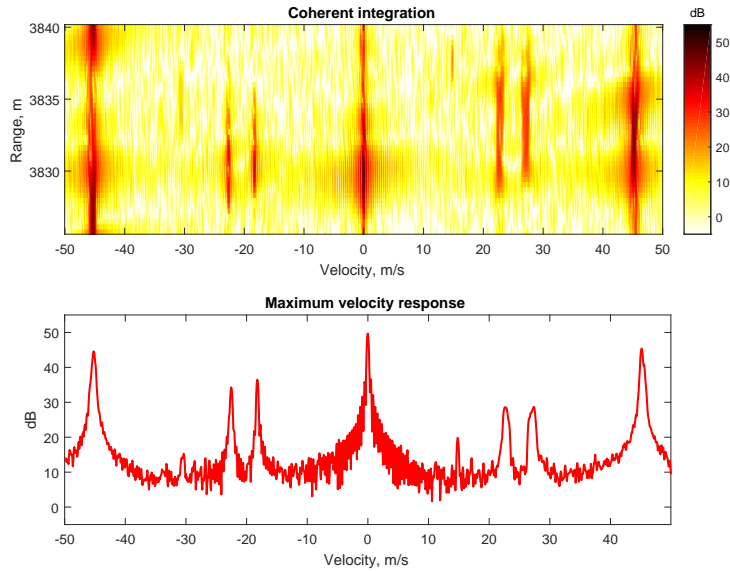
Figure 4.16: PARSAX data: wideband CI, $M = 128$, $T_r = 1$ ms

Clutter-aware SPICE is implemented as follows. First, clutter CM in one range cell is estimated from $L = 3M = 192$ target free reference cells by means of SCM:

$$\hat{\mathbf{S}} = \frac{1}{L} \sum_{l=0}^{L-1} \mathbf{z}\left(l\right) \mathbf{z}^H\left(l\right). \tag{4.30}$$

Then, the CM in the LRRS is obtained as $\hat{\mathbf{M}} = \mathbf{I}_K \otimes \hat{\mathbf{S}}$, where $\otimes$ stand for the Kroneker product. The result of the SPICE-W is shown in Fig. 4.20. It demonstrates better rejection of clutter ambiguities, than the aforementioned techniques, and correctly estimates the present targets. This result demonstrates the advantage of SPICE-W, compared to the other methods which do not benefit from the clutter estimation.

4.5.2   Target in the clutter ambiguity

To evaluate the performance in the clutter limited scenario, a new data set is created by downsampling the data set in slow time by factor 2. The new data set consists of $M = 64$ with $T_r = 2$ ms and $v_a \approx 22.5$ m/s. The time duration of the burst is now increased two times with M being constant (the new parameters are listed in braces in Table 4.3). Range migration per velocity ambiguity, defined by BM/f_c, is equal to the previous setting. In this setting, the target at velocity $v_2 \approx -23$ m/s becomes
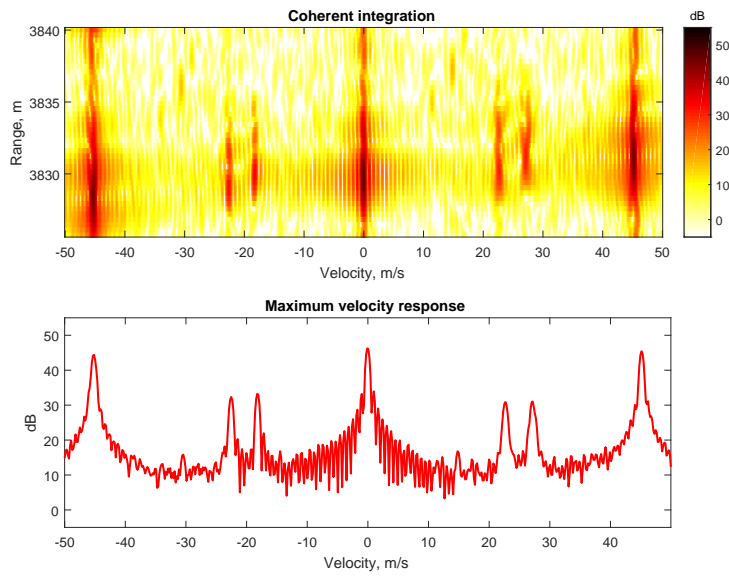
Figure 4.17: PARSAX data: wideband CI, $M = 64$, $T_r = 1$ ms
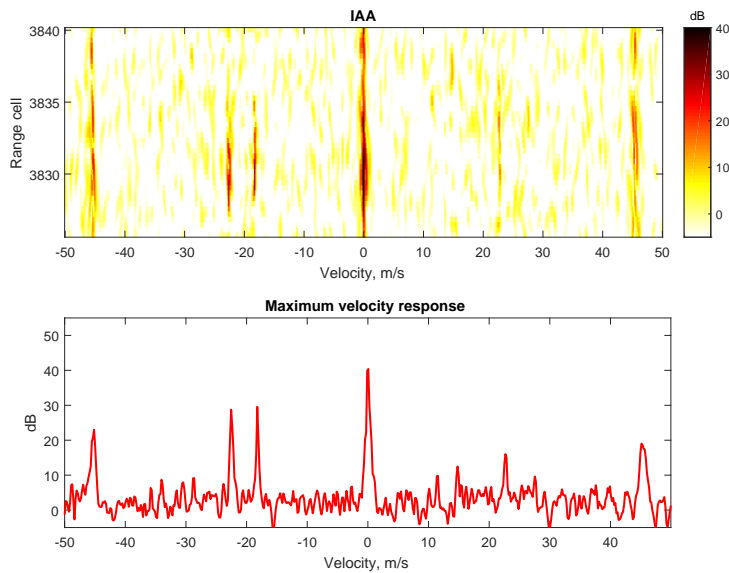
Figure 4.18: PARSAX data: IAA estimator, $M = 64$, $T_r = 1$ ms
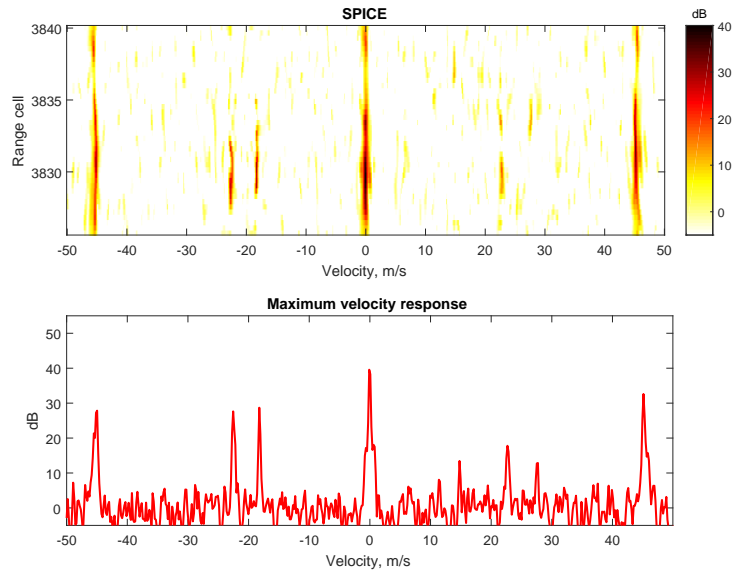
Figure 4.19: PARSAX data: SPICE estimator, $M = 64$, $T_r = 1$ ms
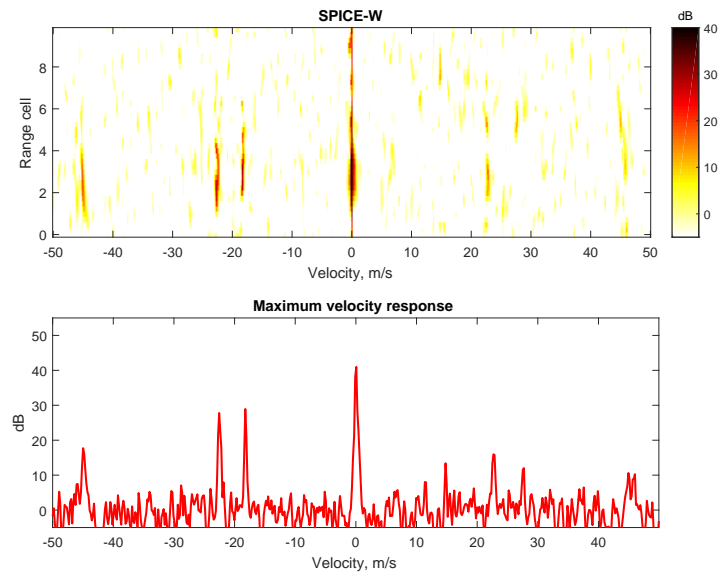
Figure 4.20: PARSAX data: SPICE-W estimator, $M = 64$, $T_r = 1$ ms

hidden by the ambiguous sidelobes of clutter and cannot be distinguished from the clutter ambiguity with the wideband CI, as shown in Fig. 4.21.

IAA and SPICE, applied for this scenario can remove the ambiguous sidelobes of the target in the clutter-free region, see Fig. 4.22, 4.23. The target, which is hidden in the clutter ambiguity, is still difficult to distinguish from the clutter ambiguity, as the clutter sidelobe at $v \approx 22$ m/s provides even higher response than the actual target at $v \approx -22$ m/s does.

Clutter-aware SPICE, which result is shown in Fig. 4.24, suppresses the sidelobe of clutter at $v \approx 22$ m/s to the level approximately 8 dB lower than the actual target response. In this estimation, the presence of two actual targets in the scene can be recognized. This demonstrates the improvement achieved by exploiting clutter correlation properties in the estimator.

This result demonstrates that some limitations for unambiguous scene reconstructions exist due to presence of diffuse clutter, which cannot be modeled adequately as a combination of multiple point-like targets. This agrees well with the results in Chapter 3.

4.6   Conclusion

Unambiguous estimation of the range-velocity scene, observed with a wideband waveform, is essentially limited by the presence of strong ambiguous sidelobes of the targets and clutter present in the scene. The existing method for unambiguous scene reconstruction either has limited capabilities for sidelobes suppression or require some parameters to be set. High-resolution parametric-free spectrum estimators - Iterative Adaptive Approach and Semi-Parametric (sparse) Iterative Covarince-based Estimator - are proposed herein for estimation of the scene. They do not require any parameter to be set by the user and provide a significant improvement in sidelobe rejection over the conventional techniques in the noise-limited case. The clutter-aware version of SPICE is proposed for improved performance in presence of diffuse clutter, whose covariance matrix is known (or estimated from the reference data). Clutter-aware SPICE outperforms the other methods considered in this chapter in presence of clutter. The performance of different methods is validated with the analysis of a real data set.
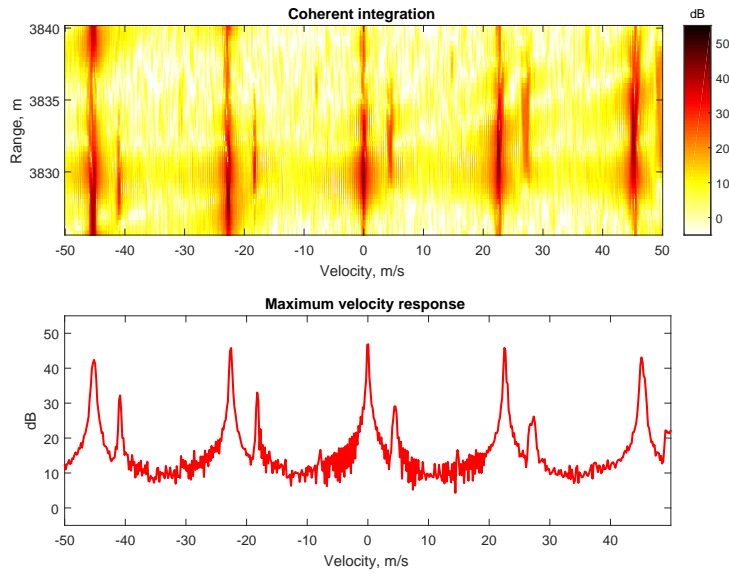
Figure 4.21: PARSAX downsampled data: wideband CI, $M = 64$, $T_r = 0.5$ ms
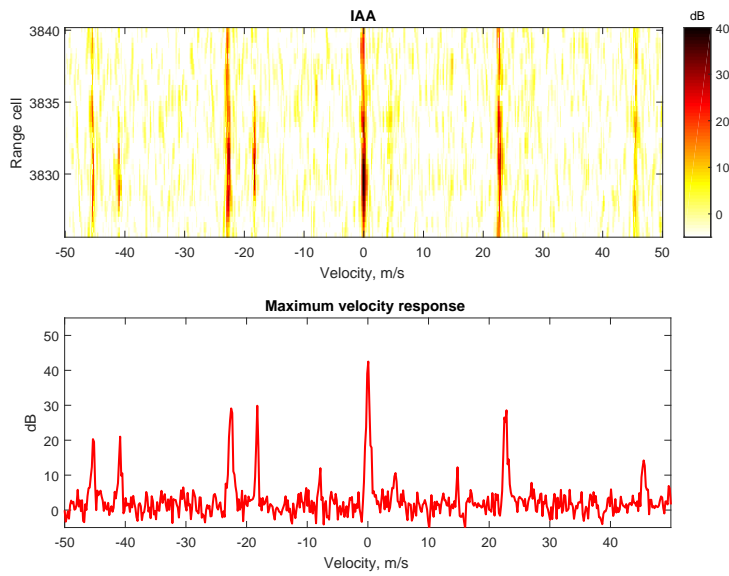
Figure 4.22: PARSAX downsampled data: IAA estimator, $M = 64$, $T_r = 0.5$ ms
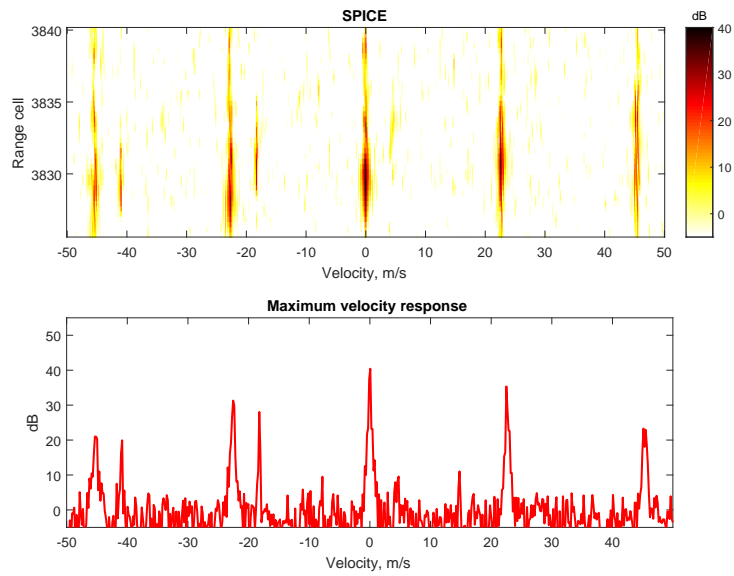
Figure 4.23: PARSAX downsampled data: SPICE estimator, $M = 64$, $T_r = 0.5$ ms
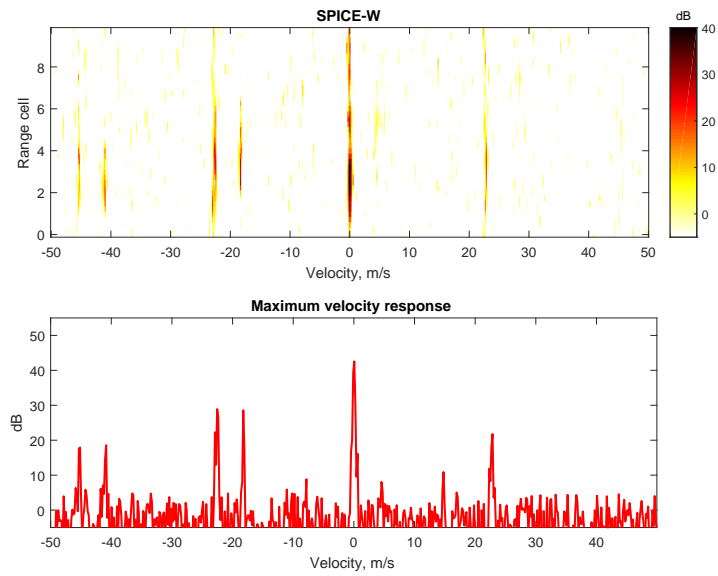
Figure 4.24: PARSAX downsampled data: SPICE-W estimator, $M = 64$, $T_r = 0.5$ ms
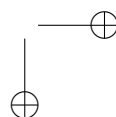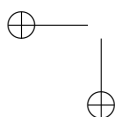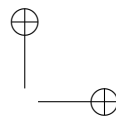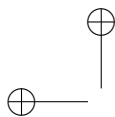
Chapter 5

Detection of moving targets in a single bursts low-PRF wideband radar

In this chapter, the problem of moving target detection with a single burst of wideband pulses is considered. Due to range-migration effect, the detection is performed over the low range resolution segment (LRRS), which can encompass the responses of multiple targets and clutter. It is demonstrated that conventional radar detectors are not adequate when more than one target can be present in the data set: they either detect the strongest target or create multiple false detections at the locations of the ambiguous sidelobes of the present targets. Two approaches to detect the presence of multiple targets in the scene are proposed. They preserve the probability of false alarm at the required level and minimize false detections due to ambiguous sidelobes of the present targets. The performance of the proposed techniques is evaluated in numerical simulations.

5.1   Introduction and problem statement

The results of the previous chapter have demonstrated that the observed scene can be estimated in the range-velocity plane without ambiguities using one burst of high-resolution pulses with low PRF. However, the unambiguous estimation of the scene does not solve the primary task of surveillance radar, namely targets detection and localization. The obtained estimation still can be used either as a part of a detector or at the next stages of the radar processing, e.g. for targets classification, tracking,

etc. To begin with, a conventional detection problem is recalled and the challenge of detecting multiple targets present in the scene is discussed.

5.1.1 Detection of a single target

The conventional detection problem in radar corresponds to the binary hypothesis testing problem, namely deciding on the presence (hypothesis H_1) or absence (hypothesis H_0) of a target in the observed data set. For the data model, considered herein (2.28), the observed data set corresponds to the LRRS under the test and the detection problem is formulated as:

$$\mathbf{y} = \begin{cases} H_0: & \mathbf{c} + \mathbf{n}, \\ H_1: & \alpha \mathbf{a}\left(\theta\right) + \mathbf{c} + \mathbf{n}, \end{cases} \tag{5.1}$$

where $\mathbf{a}\left(\theta\right)$ and α are accordingly the steering vector of the target its complex amplitude[1], constant during CPI. Note that (5.1) assumes the presence of at most one point-like target in the data set. Similarly to the previous chapters, assume that clutter-plus-noise response in a LRRS is modeled by a zero-mean complex Gaussian vector $\mathbf{c} + \mathbf{n} \sim \mathcal{CN}(0, \mathbf{M})$ with known CM.

Since the target complex amplitude is generally unknown to the radar receiver, the detector is designed via the generalized likelihood ratio test (GLRT) [21, 49]:

$$\Lambda(\mathbf{y}; \alpha|\theta) = \frac{f^{(1)}(\mathbf{y}; \alpha)}{f^{(0)}(\mathbf{y})} \underset{H_0}{\overset{H_1}{\gtrless}} \gamma', \tag{5.2}$$

with the likelihood functions under both hypotheses given by:

$$f^{(1)}(\mathbf{y}; \alpha) = \frac{1}{(2\pi)^{KM}|\mathbf{M}|} \exp\left(-(\mathbf{y} - \alpha\mathbf{a}(\theta))^H \mathbf{M}^{-1}(\mathbf{y} - \alpha\mathbf{a}(\theta))\right), \tag{5.3}$$

and $f^{(0)}(\mathbf{y}) = f^{(1)}\left(\mathbf{y}; \alpha\right)|_{\alpha=0}$.

Maximization of the (5.3) over α_1 provides:

$$\hat{\alpha}^{\mathrm{MLE}} = \frac{\mathbf{a}(\theta)\mathbf{M}^{-1}\mathbf{y}}{\mathbf{a}(\theta)\mathbf{M}^{-1}\mathbf{a}(\theta)}, \tag{5.4}$$

which being substituted into (5.2) leads to the decision rule:

$$T_1(\mathbf{y}|\theta) = \frac{\left|\mathbf{a}(\theta)\mathbf{M}^{-1}\mathbf{y}\right|^2}{\mathbf{a}(\theta)\mathbf{M}^{-1}\mathbf{a}(\theta)} \underset{H_0}{\overset{H_1}{\gtrless}} \gamma. \tag{5.5}$$

---

[1] In the previous chapter target amplitude of the location θ_i was denoted by x_i

In absence of targets, the statistic $T_1(\mathbf{y}|\theta, H_0) \sim \frac{1}{2}\chi_2^2$ is chi-squared distributed random variable with 2 degrees of freedom scaled by $1/2$. This test preserves constant false alarm rate (CFAR) w.r.t. $\mathbf{M}$. The desired probability of False Alarm (P_{FA}) is set by adjusting the threshold γ according to the Cumulative Density Function (CDF) of the chi-squared distribution. If the target is present, the statistic (5.5) follows non-central chi-squared distribution $T_1(\mathbf{y}|\theta, H_1) \sim \frac{1}{2}\chi_2^2 [\text{SCNR}]$ with the non-centrality parameter, equal to the target: $\text{SCNR} = |\alpha|^2 \mathbf{a}(\theta)\mathbf{M}^{-1}\mathbf{a}(\theta)$ [63].

Note, that the decision test (5.5) can be different to ensure CFAR performance in difficult scenarios, e.g. when clutter is not Gaussian, as discussed in Chapter 6, or when the matrix $\mathbf{M}$ is not known *a priori*, but it is estimated from the reference data set [64, 65].

The model (5.1) assumes that the target magnitude is an unknown constant. The presence of the target under H_1 therefore imposes non-zero mean of the distribution in (5.1), but does not affect the CM. This model is referred to as First Order Gaussian (FOG) model [66]. The alternative approach is to assume that the target amplitude is zero-mean Gaussian distributed, and the CM of the data differs between H_0 and H_1 by the target component $P\mathbf{a}(\theta)\mathbf{a}^H(\theta)$, where P is the signal power to be estimated. Interestingly, the detection for the latter case, refereed to as Second Order Gaussian model, is a monotonic function of the same statistics [67].

In practice, target location θ is unknown *a priori*. Therefore, the statistic (5.5) is evaluated $\forall \theta \in \Theta$ and the decision is made by [21, 49]:

$$\begin{cases} T(\mathbf{y}) = T_1(\mathbf{y}|\hat{\theta}) \underset{<H_0}{\overset{\geq H_1}{\gtrless}} \gamma, \\ \hat{\theta} = \text{argmax}_{\theta \in \Theta}\, T_1(\mathbf{y}|\theta). \end{cases} \tag{5.6}$$

which is the direct consequence of (5.1), where the presence of at most one target in the observed data set is considered. The second equation defines the location of the target if hypothesis H_1 is selected. Since the test estimates SCNR for every possible target location, the maximization over θ ensures the detection of the target at its correct location (or in the vicinity of it in case of grid mismatch).

Irrespective of the statistics $T_1(\mathbf{y}|\theta)$, the location of the target (5.6) is obtained by the search over the whole target space Θ. The limitation of that procedure is its inability to declare the presence of more than one target in the scene. In this case, the maximization (5.6) will ignore the presence of any target, except of the one with the highest SCNR. Recall that in the wideband case, the data vector $\mathbf{y}$ represents a block of K adjacent range cells. In this case, a few targets contaminated by the clutter can be present in the data vector $\mathbf{y}$, e.g. when observing a highway with multiple moving cars. For this situation, another approach should be considered.

5.1.2   Detection of multiple targets

Recall the data model, which describes the vectorized received data in the LRRS under test:

$$\mathbf{y} = \sum_{s=1}^{S} \alpha_s \mathbf{a}(\theta_s) + \mathbf{c} + \mathbf{n}. \tag{5.7}$$

Moreover, it is assumed that clutter-plus-noise response is a zero-mean Gaussian vector $\mathbf{c} + \mathbf{n} \sim \mathcal{CN}(0, \mathbf{M})$ and S primitive scatterers with complex back-scattering coefficients $\alpha_s, \forall s = 1, \ldots, S$ are present in the observed LRRS.

If more than one target can be present in the scene, as in (5.7), the radar processor should decide on how many targets S are present in the data and estimate their parameters $\alpha_s, \theta_s, \forall s = 1, \ldots, S$. That is equivalent to deciding in favor of one of hypotheses:

$$H_S : \mathbf{y} = \sum_{s=1}^{S} \alpha_s \mathbf{a}(\theta_s) + \mathbf{c} + \mathbf{n}, \ \ S \in [0, S_{\max}], \tag{5.8}$$

where $S_{\max}$ is the maximum expected number of point-like targets in the data.

The estimation of the integer parameter S from the data set is called model order selection [68]. With application to radar, Minimum description Length (MDL) [69], Akaike Information Criterion (AIC) [70] and Bayesian Information Criterion (BIC) [68] are mostly considered, e.g. [15,16,28]. The major limitation of applying information criteria to the problem under consideration is their inability to control the false alarm probability (P_{FA}), similarly to the conventional detectors. Indeed, in heavy environmental conditions and presence of interfering signals and/or jammers, the ability to increase or decrease the number of detected targets on the radar display by controlling P_{FA} plays a crucial role for the radar operator. Therefore, information criteria are not considered for detection of multiple targets herein, and another strategy is followed.

One possible approach to detect multiple targets present in the data set consists of applying CFAR test (5.5) to every possible target location $\theta \in \Theta$, without subsequent maximization. A target is then detected at every location θ, at which the test passes the detection threshold (5.5). The shortcoming of this approach is its sensitivity to the sidelobes of the present targets — a sidelobe response (and especially an ambiguous sidelobe) of a strong target will cross the threshold and create a target-like output, similar to a false alarm. In a dense target scenario, every target will create a number of such false targets as a result of ambiguous sidelobes.

Another way to detect the targets consists of two steps: first, estimate the observed scene with some high-resolution estimator, which resolves velocity ambiguities of the

targets (see Chapter 4) and, second, detect the targets from the estimated range-velocity image, alike cell-averaging (CA), order statistics (OS) and many other tests do [3]. The major limitation of this approach is unknown probability distribution of the outputs of IAA and SPICE. A similar way to tackle the problem has been investigated using IAA in [60, 71], where the advantage of IAA detector is evident in terms of receiver operating characteristic (ROC) curves, but P_{FA} control for the proposed detector is missing.

5.2 Proposed approach

Consider a scenario in which more than one target can be present in the scene. Then, the task of a detector is to decide in favor of one of the hypotheses in (5.8). Two strategies to attack this problem are considered here.

5.2.1 RELAX-like detector of multiple targets

Assume that the targets present in the scene follow the First Order Gaussian (FOG) model. Then the received data is distributed as:

$$\mathbf{y} \sim \begin{cases} H_0 : CN\left(\mathbf{0}_{KM}, \mathbf{M}\right), \\ H_S : CN\left(\sum_{s=1}^{S} \alpha_s \mathbf{a}(\theta_s), \mathbf{M}\right), \end{cases} \tag{5.9}$$

where hypothesis H_S stands for the presence of S point-like targets in the scene, $S \ll KM$. Note also the the hypotheses $H_0, \ldots, H_S$ are nested, namely $H_S = H_{S+P}|_{\alpha_i=0, \forall i=S+1, \ldots S+P}$. Define the likelihood function for each hypothesis S via:

$$f^{(S)}(\mathbf{y}; \alpha_{1 \ldots S}, \theta_{1 \ldots S}) = \frac{\exp\left(-\left(\mathbf{y} - \sum_{s=1}^{S} \alpha_s \mathbf{a}(\theta_s)\right)^H \mathbf{M}^{-1}\left(\mathbf{y} - \sum_{s=1}^{S} \alpha_s \mathbf{a}(\theta_s)\right)\right)}{\pi^{KM} |\mathbf{M}|}, \tag{5.10}$$

and since the hypotheses are nested $f^{(S)}(\mathbf{y}) = f^{(S+P)}(\mathbf{y})|_{\alpha_i=0, \forall i=S+1, \ldots, S+P}$. Because the clutter CM is known, the whitening transform can be applied. The data vector and the target signature are then given accordingly:

$$\mathbf{z} = \mathbf{M}^{-1/2} \mathbf{y}; \tag{5.11}$$

$$\mathbf{b}(\theta) = \mathbf{M}^{-1/2} \mathbf{a}(\theta), \ \forall \theta \in \Theta. \tag{5.12}$$

Maximization of the log-likelihood with respect to all the unknown parameters is equal to minimization of the quadratic cost function F:

$$F\left(N, \alpha_{1 \ldots S}, \theta_{1 \ldots S}\right) = \left(\mathbf{z} - \sum_{s=1}^{S} \alpha_s \mathbf{b}(\theta_s)\right)^H \left(\mathbf{z} - \sum_{s=1}^{S} \alpha_s \mathbf{b}(\theta_s)\right). \tag{5.13}$$

The maximization of this cost function w.r.t. α_s and $\theta_s, \forall s = 1, \ldots, S$ requires a multidimensional search over all the unknown parameters, which is typically NP-hard. An efficient implementation for maximization (5.13) has been proposed in [28] and referred as RELAX spectrum estimator. RELAX is asymptotically statistically efficient estimator, with improved performance over the CLEAN algorithm [72]. It is expected to provide accurate estimation of the targets' parameters (α_s, θ_s) in the considered model, because of sufficiently large data dimension KM. RELAX is a semi-parametric algorithm, which requires the number of point-like targets to be known or estimated [28]. Herein, it is proposed to use the threshold of the CFAR detector (5.5) for detection of a new target in RELAX iteration, instead of using an information criterion. The proposed modification allows controlling P_{FA} for the proposed test.

Although the estimation of sinusoidal parameters can be obtained with RELAX in presence of clutter or correlated noise, herein RELAX is applied to the whitened data. The whitening transformation is crucial to avoid estimating the clutter response, which can dominate over the targets responses and can occur spread in range and velocity domain. Reconstruction of the clutter response with RELAX might lead to high computation load and performance loss.

The proposed RELAX-like detector consists of three steps: initialization, iterative estimation and detection, and correction.

Initialization   The proposed detector of multiple point-like targets is initialized with the statistics and the binary output of the matched filter detector (5.5), which can be rewritten in terms of whitened data $\mathbf{z}$ with (5.11). Denote by $\Theta_D = \{\theta \in \Theta|_{T_1(\mathbf{z}|\theta)>\gamma}\}$ the set of locations, at which the test (5.5) passes the threshold. Also, introduce a new set of locations Θ_T, where the target are declared after the processing and initialize it with an empty set: $\Theta_T = \{\}$. If $\mathrm{card}\,(\Theta_D) \leq 1$, the detection is equivalent to the single target case and the hypothesis H_0 or H_1 is selected, depending on the output of (5.6). In this case no further processing is required.

Iterative estimation and detection   At the N-th iteration of the algorithm, a new target with index N is found in the data set by maximizing observed SCNR over $\theta \in \Theta_D$:

$$\hat{\theta}_N = \operatorname*{argmax}_{\theta \in \Theta_D} \frac{\left|\mathbf{b}^H(\theta)\mathbf{z}^{(N-1)}\right|^2}{\mathbf{b}^H(\theta)\mathbf{b}(\theta)}, \tag{5.14}$$

$$\Theta_T = \Theta_T \cup \hat{\theta}_N, \tag{5.15}$$

where the meaning of $\mathbf{z}^{(N)}$ is explained shortly and $\cup$ defines set union. The amplitude of the new target is estimated by:

$$\hat{\alpha}_N = \frac{\mathbf{b}^H(\hat{\theta}_N)\mathbf{z}^{(N-1)}}{\mathbf{b}^H(\hat{\theta}_N)\mathbf{b}(\hat{\theta}_N)}. \tag{5.16}$$

With the estimated location and magnitude, the N-th target is added to the set of detected targets Θ_{T}.

When a new target has been added, the parameters of N previously detected targets are updated by iterating a few times the estimates:

$$\mathbf{z}_j^{(N)} = \mathbf{z} - \sum_{n=1, n \neq j}^{N} \alpha_n \mathbf{b}(\theta_n); \tag{5.17}$$

$$\hat{\theta}_j = \underset{\theta \in \Theta}{\operatorname{argmax}} \frac{\left| \mathbf{b}^H(\theta)\mathbf{z}_j^{(N)} \right|^2}{\mathbf{b}^H(\theta)\mathbf{b}(\theta)}; \tag{5.18}$$

$$\hat{\alpha}_j = \frac{\mathbf{b}^H(\hat{\theta}_j)\mathbf{z}_j^{(N)}}{\mathbf{b}^H(\hat{\theta}_j)\mathbf{b}(\hat{\theta}_j)}. \tag{5.19}$$

In each iteration, the parameters of every target j are re-estimated in three steps: first, a new data set is created by subtracting the signatures of the other targets (5.17); second, the location of the j-th target is updated (also in Θ_{T}) by (5.18); third, the magnitude of the j-th target is re-estimated (5.19). When $N = 1$ no iteration is required. In the converse case, the iterations are repeated until the change of the cost function (5.13) after applying (5.17) - (5.19) for all the targets becomes smaller than some pre-defined value ϵ [28].

Moreover, the search of the target location at the iteration N can be performed in the vicinity of its previous location, which significantly decreases the search time [73]. At this stage a larger oversampling (in both range and velocity dimensions) is applied to improve estimation of the target locations, especially with high SCNR.

When the parameters of all the targets are estimated, the data vector and the set of detected locations Θ_{D} are updated:

$$\mathbf{z}^{(N)} = \mathbf{z} - \sum_{n=1}^{N} \alpha_n \mathbf{b}(\theta_n); \tag{5.20}$$

$$\Theta_{\mathrm{D}} = \theta \in \Theta|_{T_1\left(\mathbf{z}^{(N)}, \theta\right) > \gamma}. \tag{5.21}$$

The subtraction of the estimated target response from the data removes the detection of this target and also the false detection due to its sidelobes from the set Θ_{D}. Therefore, the outer loop is stopped when no more targets are detected by (5.21), or

equivalently card $(\Theta_D) = 0$. The output of the algorithm are the locations Θ_T and magnitudes $\alpha_n, \forall n = 1, \ldots, N$ of the detected targets.

To decrease the computational complexity of the algorithm and speed up its convergence, the search in (5.21) can be performed only at the locations, where the test (5.5) declares target presence (so Θ_D at the initialization of the algorithm). In this case, one target will be removed from the data set at each iteration, the maximum number of iterations is limited by card (Θ_D), where Θ_D is the set of locations at the initialization.

Correction   At the final step of the processing, the detected targets should be tested against the CFAR threshold in presence of the other targets. The locations, at which the test is not passed are removed from the set of detected targets:

$$\tilde{\Theta}_T = \Theta_T - \Theta_T\big|_{T_1\left(\mathbf{z}_j^{(N)}, \hat{\theta}_j\right) < \gamma, \ \forall j = 1, \ldots, N}, \tag{5.22}$$

where $\Theta_A - \Theta_B$ denotes the difference of the sets. This post-processing is required to remove from the output some false targets, which can arise in the RELAX procedure when a wrong location has been selected at some iteration. For example, at one of the iterations, the maximum was found at the sidelobe of a real target. At the next iterations, RELAX minimizes the magnitude of this wrong target, but still keeps its location in Θ_T. The procedure (5.22) will clean the location of the false target from the final detection set. It was found to be a useful step in the numerical simulations of the RELAX detector. The number of detected targets and the hypothesis in (5.9) are selected as $\hat{S} = \text{card}\left(\tilde{\Theta}_T\right)$.

In the majority of the data sets the conventional CFAR detector, e.g. (5.5), with the appropriately selected P_{FA} will declare the presence of not more than one target in a LRRS: card $(\Theta_D) \leq 1$. In this case, no post-processing with RELAX is required. This makes the proposed RELAX-like detector computationally affordable for real applications.

5.2.2   Multiple target detection using the unambiguous estimation of the observed scene

This approach is partially heuristic and relies on the fact that the targets with the SCNR high enough to be detected with typical $P_{FA} \in [10^{-10}, 10^{-5}]$ and not competing with the other targets (are not located in the ambiguous sidelobes of each other), have amplitude estimation, obtained with IAA close to the amplitude MLE (5.4) at the correct target location θ_i, so: $\hat{\alpha}_i^{ML} \approx \hat{\alpha}_i^{IAA}$, but not in the location of a sidelobe. The amplitude estimation $\hat{\alpha}_i^{IAA}$, denoted by x_i in (4.17) at the location θ_i resolves the sidelobe issue (global leakage) and therefore provides a reasonable estimate of

$\alpha_i, \forall \theta_i \in \Theta$. In this way, detection can be performed $\forall \theta_i \in \Theta$ in parallel without subsequent maximization over location parameter θ.

The choice of IAA for development of this detector is motivated by its lower error in the estimation of the target magnitude compared to SPICE, as noted in [18] and its robustness to the presence of clutter and extended targets in the scene with no parameters involved in the estimation. In principle, a similar strategy can be applied with another high-resolution spectrum estimator, used instead of IAA. However, herein only the detector using IAA is considered. Two options to incorporate IAA estimation into the detector are investigated and referred to by IAA-(A) and IAA-(B) accordingly.

IAA-(A) detector Assume IAA estimation is available for every possible target location θ_i on the grid. Define the detector via the likelihood ratio (5.2), where the target's amplitude estimation α_i is obtained with IAA:

$$\Lambda(\mathbf{y}|\theta_i) = \frac{f^{(1)}(\mathbf{y};\alpha_i = \hat{\alpha}_i^{\mathrm{IAA}})}{f^{(0)}(\mathbf{y})} \underset{H_0}{\overset{H_1}{\gtrless}} \gamma'. \tag{5.23}$$

Following the lines (5.2) - (5.5) and substituting $\hat{\alpha}_i^{\mathrm{IAA}}$ for $\hat{\alpha}_i^{\mathrm{MLE}}$, it can be shown that the quadratic form in (5.3) under H_1 becomes:

$$\begin{aligned}
&\left(\mathbf{y} - \hat{\alpha}_i^{\mathrm{IAA}}\mathbf{a}(\theta_i)\right)^H \mathbf{M}^{-1} \left(\mathbf{y} - \hat{\alpha}_i^{\mathrm{IAA}}\mathbf{a}(\theta_i)\right) \\
&= \mathbf{y}^H\mathbf{M}^{-1}\mathbf{y} + \mathbf{a}^H(\theta_i)\mathbf{M}^{-1}\mathbf{a}(\theta_i)\left(\left|\hat{\alpha}_i^{\mathrm{IAA}}\right|^2 - 2\Re\left(\hat{\alpha}_i^{\mathrm{IAA}}\hat{\alpha}_i^{\mathrm{MLE}}\right)\right) \\
&= \mathbf{y}^H\mathbf{M}^{-1}\mathbf{y} + \mathbf{a}^H(\theta_i)\mathbf{M}^{-1}\mathbf{a}(\theta_i)\left(\left|\hat{\alpha}_i^{\mathrm{IAA}} - \hat{\alpha}_i^{\mathrm{MLE}}\right|^2 - \left|\hat{\alpha}_i^{\mathrm{MLE}}\right|^2\right) \\
&= \mathbf{y}^H\mathbf{M}^{-1}\mathbf{y} - \frac{\left|\mathbf{a}(\theta_i)\mathbf{M}^{-1}\mathbf{y}\right|^2}{\mathbf{a}^H(\theta_i)\mathbf{M}^{-1}\mathbf{a}(\theta_i)}\left(1 - \frac{\left|\hat{\alpha}_i^{\mathrm{IAA}} - \hat{\alpha}_i^{\mathrm{MLE}}\right|^2}{\left|\hat{\alpha}_i^{\mathrm{IAA}}\right|^2}\right).
\end{aligned} \tag{5.24}$$

Then, similarly to (5.5), the detection test can be written as:

$$T(\mathbf{y}|\theta_i) = \frac{\left|\mathbf{a}(\theta_i)\mathbf{M}^{-1}\mathbf{y}\right|^2}{\mathbf{a}^H(\theta_i)\mathbf{M}^{-1}\mathbf{a}(\theta_i)}G(\theta_i) \underset{H_0}{\overset{H_1}{\gtrless}} \gamma, \tag{5.25}$$

where

$$G(\theta_i) = 1 - \frac{\left|\hat{\alpha}_i^{\mathrm{IAA}} - \hat{\alpha}_i^{\mathrm{MLE}}\right|^2}{\left|\hat{\alpha}_i^{\mathrm{MLE}}\right|^2}. \tag{5.26}$$

The proposed decision test (5.25) is represented as a product of the standard matched filter detector (5.5) and the gain term: $G(\theta_i)$. The effect of this term can be qualitatively analyzed by comparison of the recovered range velocity maps with the CI

(which is MLE for single target in the noise-limited scenario) and IAA, shown in the previous chapter (Fig. 4.4, 4.7). Note that for the correct locations of the targets $\left|\alpha_i^{\mathrm{IAA}} - \alpha_i^{\mathrm{MLE}}\right| \ll \left|\alpha_i^{\mathrm{MLE}}\right|$ and so $G(\theta_i) \approx 1$. Thus, around the correct target location, the test reduces to the single point-target test with an additional loss due to approximation. On the other hand, for the sidelobe location $\left|\alpha_i^{\mathrm{IAA}} - \alpha_i^{\mathrm{MLE}}\right| \approx \left|\alpha_i^{\mathrm{MLE}}\right|$ and accordingly $G(\theta_i) \approx 0$, which allows to reject false detections due to the sidelobes of strong targets and simultaneously detect weak targets at their correct locations. In presence of clutter, some similar performance is expected due to IAA stability against whitening transform (4.23). In addition, it can be seen that $G(\theta_i) \leq 1, \forall \theta_i \in \Theta$, therefore the proposed modification of the test ensures a bounded false alarm property when the threshold for the original test is applied. Moreover, for small $P_{FA} \leq 10^{-6}$, the false alarms appears in the target-like spikes of clutter or noise, the magnitude of which is well-estimated by IAA. The deviation of P_{FA} of the proposed detector from the required level in this case is expected to be small.

IAA-(B) detector   Herein the detector of multiple point-like targets is derived for the second-order Gaussian model, which assumes that the target response is zero-mean Gaussian process with the CM, defined by the target signature. The detection problem for the second-order Gaussian model is:

$$\mathbf{y} \sim \begin{cases} H_0 : CN\left(\mathbf{0}, \mathbf{M}\right), \\ H_1 : CN\left(\mathbf{0}, \mathbf{M} + P_i\mathbf{a}(\theta_i)\mathbf{a}^H(\theta_i)\right), \end{cases} \tag{5.27}$$

where P_i corresponds to $|\alpha_i|^2$ in the above notations. Define the GLRT:

$$\Lambda(\mathbf{y}; P_i|\theta_i) = \frac{f^{(1)}(\mathbf{y}; P_i)}{f^{(0)}(\mathbf{y})} \underset{H_0}{\overset{H_1}{\gtrless}} \gamma' \tag{5.28}$$

with the likelihood functions given by:

$$f^{(1)}(\mathbf{y}; P_i) = \frac{\exp\left(-\mathbf{y}^H\left(\mathbf{M} + P_i\mathbf{a}(\theta_i)\mathbf{a}^H(\theta_i)\right)^{-1}\mathbf{y}\right)}{\pi^{KM}\left|\mathbf{M} + P_i\mathbf{a}(\theta_i)\mathbf{a}^H(\theta_i)\right|}. \tag{5.29}$$

under H_1 and $f^{(0)}(\mathbf{y}) = f^{(1)}(\mathbf{y}; P_i)|_{P_i=0}$. Simplifying the above with:

$$\left|\mathbf{M} + P_i\mathbf{a}(\theta_i)\mathbf{a}^H(\theta_i)\right| = |\mathbf{M}|\left(1 + P_i\mathbf{a}^H(\theta_i)\mathbf{M}^{-1}\mathbf{a}(\theta_i)\right); \tag{5.30}$$

$$\left(\mathbf{M} + P_i\mathbf{a}(\theta_i)\mathbf{a}^H(\theta_i)\right)^{-1} = \mathbf{M}^{-1} - \frac{P_i\mathbf{M}^{-1}\mathbf{a}(\theta_i)\mathbf{a}^H(\theta_i)\mathbf{M}^{-1}}{1 + P\mathbf{a}^H(\theta_i)\mathbf{M}^{-1}\mathbf{a}(\theta_i)} \tag{5.31}$$

gives the GLRT in the form:

$$\Lambda(\mathbf{y}; P_i|\theta_i) = \left(1 + P_i\mathbf{a}^H(\theta_i)\mathbf{M}^{-1}\mathbf{a}(\theta_i)\right)^{-1}\exp\left(\frac{P_i\left|\mathbf{a}^H(\theta_i)\mathbf{M}^{-1}\mathbf{y}\right|^2}{\mathbf{a}^H(\theta_i)\mathbf{M}^{-1}\mathbf{a}(\theta_i)}\right) \underset{H_0}{\overset{H_1}{\gtrless}} \gamma'. \tag{5.32}$$

Table 5.1: Simulated radar parameters

Parameter		Value
Carrier frequency	f_c	10 GHz
Bandwidth	B	1 GHz
PRI	T_r	1 ms
Ambiguous velocity	v_a	15 m/s
Pulses	M	32
Range cells in LRRS	K	8

According to [67], the MLE of P_i can be defined:

$$\hat{P}_i^{\mathrm{MLE}} = \max\left\{ \frac{\left|\mathbf{a}^H(\theta_i)\mathbf{M}^{-1}\mathbf{y}\right|^2 - \mathbf{a}^H(\theta_i)\mathbf{M}^{-1}\mathbf{a}(\theta_i)}{\left(\mathbf{a}^H(\theta_i)\mathbf{M}^{-1}\mathbf{a}(\theta_i)\right)^2},\ 0\right\}. \tag{5.33}$$

Plugging this estimation into the GLRT results in a monotonic function of the statistics (5.5) (for details see [67]).

In a multi-target scenario, an approximate MLE of $\hat{P}_i$ is obtained via IAA $\hat{P}_i^{\mathrm{IAA}} = \left|x_i^{\mathrm{IAA}}\right|^2$, as demonstrated in [15, 16]. Therefore, the unambiguous scene estimation, delivered by IAA, can be incorporated into a detector via $\hat{P}_i^{\mathrm{IAA}}$ by:

$$\Lambda(\mathbf{y}|\theta_i) = \frac{f^{(1)}(\mathbf{y}; P_i = \hat{P}_i^{\mathrm{IAA}})}{f^{(0)}(\mathbf{y})} \underset{H_0}{\overset{H_1}{\gtrless}} \gamma'. \tag{5.34}$$

Substitution of the likelihood functions into (5.34) gives the detection rule $\forall \theta_i \in \Theta$ in the form:

$$\left(1 + \hat{P}_i^{\mathrm{IAA}}\mathbf{a}^H(\theta_i)\mathbf{M}^{-1}\mathbf{a}^H(\theta_i)\right)^{-1} \exp\left(\frac{\hat{P}_i^{\mathrm{IAA}}\left|\mathbf{a}(\theta_i)\mathbf{M}^{-1}\mathbf{y}\right|^2}{\mathbf{a}^H(\theta_i)\mathbf{M}^{-1}\mathbf{a}(\theta_i)}\right) \underset{H_0}{\overset{H_1}{\gtrless}} \gamma'. \tag{5.35}$$

The estimate $\hat{P}_i^{\mathrm{MLE}}$ is a unique maximum of the likelihood ratio over P_i, which implies that substitution of $\hat{P}_i^{\mathrm{IAA}}$ into the test insures a bounded false alarm property of (5.35). Similarly to the test (5.25), the detector (5.35) is expected to provide better suppression of the sidelobes than the matched filter detector and approach the required level for small P_{FA}.

5.3   Performance assessment

In this section the performance of the following tests is investigated:

- Matched Filter (MF) detector (5.5);

- RELAX-like detector of multiple targets (5.18) - (5.22);

- IAA-A detector (5.25);

- IAA-B detector (5.35).

The test (5.6), which involves maximization over the parameter space, is not considered for comparison here since it cannot tackle the situation with multiple targets present in the scene, which is the main objective of this chapter.

Performance of the tests is evaluated by numerical simulations in three scenarios:

- Target-free scenario;

- Single target present in the data set;

- Multiple targets present in the data set.

The radar parameters, considered in the simulations are summarized in Table 5.1. The ambiguity function for these settings is demonstrated in Fig. 2.3, b and the level of its first ambiguous sidelobe is $SL_1 \approx -10$ dB. The maximum expected target velocity is set to $v_{\max} = 32$ m/s. The number of range cells is accordingly set to $K = 8$ in order to satisfy (2.14). The range-velocity map is estimated in $N_t = n_t K = 32$ range and $N_v = 2\lceil n_v M v_{max}/v_a \rceil + 1 = 561$ velocity samples accordingly. IAA estimation obtained after $I_{\text{IAA}} = 5$ iterations is used in IAA-A and IAA-B detectors.

The clutter has exponential decay Doppler PSD[1] with $\beta = 12$, $r = 0$ and $CNR = \sigma_c^2/\sigma_n^2 = 20$ dB. The detection curves are plotted for the post-processing SCNR:

$$\text{SCNR}_s = |\alpha_s|\mathbf{a}^H(\theta_s)\mathbf{M}^{-1}\mathbf{a}(\theta_s), \tag{5.36}$$

where θ_s is the location parameter of the s-th target.

5.3.1   Target-free scenario

Target-free scenario is considered in order to evaluate false alarm regulation of the considered detectors: $P_{FA} = \Pr\{T(\mathbf{y}|H_0) > \gamma\}, \forall \theta \in \Theta$. False alarm regulation is evaluated by testing 100 target free scenes of $N_t N_v$ cells each, so in approximately $1.8 \cdot 10^6$ trials. Simulations results for different tests in the noise-limited case are shown in Fig. 5.1. The horizontal axis shows the P_{FA} set for each test (referred as designed P_{FA}) and the vertical axis corresponds to the value of $\hat{P}_{FA}$ evaluated in numerical simulations.

The results in Fig. 5.1 demonstrate that only the MF detector is a CFAR test, the other tests, namely RELAX, IAA-A and IAA-B, have bounded false alarm probability.

---

[1]The details about exponential decay clutter spectrum are given in Chapter 3
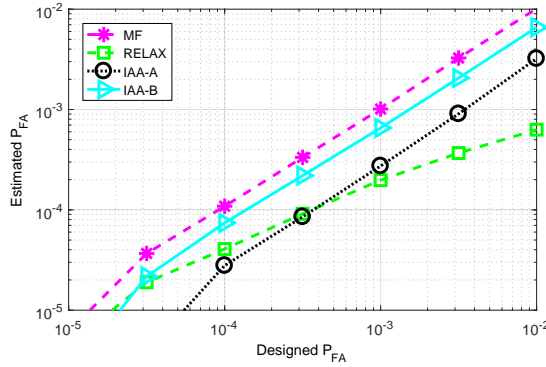
Figure 5.1: False alarm regulation

Bounded P_{FA} property of the RELAX-like detector comes from its structure: it applies post-processing to the output of MF detector, which is a CFAR test. If all the declared targets pass this post-processing, the output is equal to that of the MF detector; otherwise, some detections are removed from the set of targets, leading to the bounded false alarm property of the RELAX detectors. Note that with increasing of the threshold, P_{FA} regulation of RELAX-like test converges to the designed value, so for typical $P_{FA} \in [10^{-10}, 10^{-6}]$, the RELAX-like detector has approximate CFAR behavior.

The proposed tests, which use IAA estimation, also ensure bounded P_{FA} property, as follows from their structure. Simulations results demonstrate that IAA-B test approached closer the designed P_{FA}, compared to IAA-A test. It was observed that the difference between the designed and obtained P_{FA} for the IAA detectors can slightly (within one order) vary with the PSD of the clutter and the processing parameters (oversampling in range and time, number of IAA iterations).

5.3.2 Single target present in the data set

The scenario with a single target present in the data set is considered to evaluate the ability of the detectors to declare the target presence at its correct location and reject the ambiguous sidelobes. Probability of detection here is defined as probability to declare the presence of the target within a resolution cell from its correct location $\theta_0 = \{\tau_0, v_0\}$:

$$P_D = \Pr \left\{ \max_{\theta \in \mathcal{T}} T(\mathbf{y}|\theta) > \gamma \right\}, \qquad (5.37)$$

where $\mathcal{T} = \{\theta = \{\tau, v\} \in \Theta \mid (|\tau - \tau_0| \leq \delta_R/2) \wedge (|v - v_0| \leq \delta_v/2)\}$.
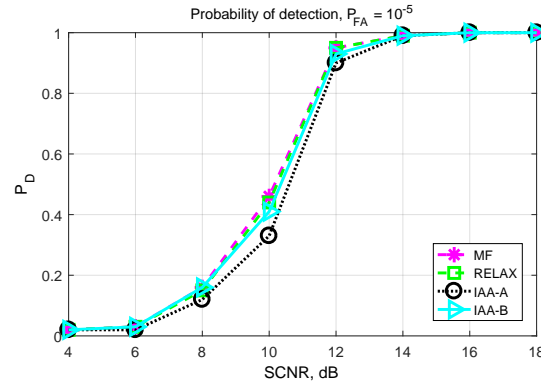
Figure 5.2: Probability of detection vs SCNR of a single target, $P_{FA} = 10^{-5}$

The detection curves, evaluated in 100 independent realizations of the considered detectors, are plotted in Fig. 5.2 for $P_{FA} = 10^{-5}$. The results demonstrate that all the detectors have similar performance, except for for IAA-A, which experiences about 0.5 dB loss compared to the MF detector. RELAX-like and IAA-B detectors have almost the same performance as the MF detector.

In order to account for the behavior of the detectors not only in the vicinity of the target location but also at the location of the ambiguous sidelobes, consider the following metric. The probability of correct set detection is the probability that all the targets present in the scene are detected at their correct locations (within a resolution cell in each dimension) and at the same time no false targets are declared in the observed scene:

$$P_{CD} = \Pr \left\{ \left(\max_{\theta_t \in \mathcal{T}_s} T\left(\mathbf{y}|\theta_t\right) > \gamma, \forall t = 1, \ldots, S \right) \wedge \left(\max_{\theta_n \in \Theta - (\mathcal{T}_1 \vee \ldots \vee \mathcal{T}_S)} T\left(\mathbf{y}|\theta_n\right) < \gamma \right) \right\},$$
(5.38)

where $\Theta - \mathcal{T}$ denotes the difference of the sets Θ and $\mathcal{T}$. This metric accounts simultaneously for the correct detection of the targets and for the false alarms, which can occur due to a spike of clutter (noise) or as a false detection at a sidelobe of one of the present targets and has been used before e.g. in [18] (hence there the number of targets is assumed *a priori* known to the detector). Performance of the algorithms then can be compared using the counterpart of the detection characteristic, which demonstrates P_{CD} as a function of the target SCNR. In this metric, the optimal detector is characterized by a non-decreasing function, which increases similarly to the detection curve in Fig. 5.2, but saturates at the level $P_{\mathrm{CD}}^{\max} = 1 - P_{FA} K M n_{\mathrm{va}}$, where $K M n_{\mathrm{va}}$ defines the number of range-velocity cells with the nominal range and velocity resolution of the waveform. The simulation results for $P_{FA} = 10^{-5}$ and
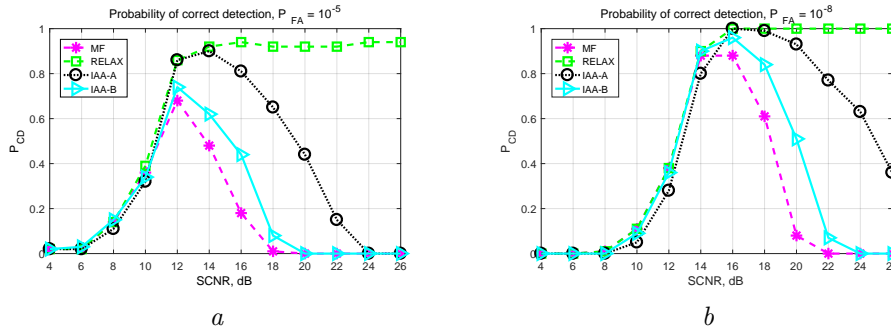
Figure 5.3: Probability of correct set detection vs SCNR for a single target present in the data set: a - $P_{FA} = 10^{-5}$; b - $P_{FA} = 10^{-8}$.

$P_{FA} = 10^{-8}$ are demonstrated in Fig. 5.3; the performance has been evaluated in 100 independent realizations of the scene. In this setting $P_{\mathrm{CD}}^{\max} \approx 0.99$ and $P_{\mathrm{CD}}^{\max} \approx 1 - 10^{-5}$ for $P_{FA} = 10^{-5}$ and $P_{FA} = 10^{-8}$ accordingly.

The analysis presented in Fig. 5.3 demonstrates that the MF detector has only 3-7 dB SCNR range, at which $P_{\mathrm{CD}} \geq 0.5$. It expands with increasing the detection threshold (decreasing P_{FA}), but it is still limited by the level of the first ambiguous sidelobe, which is $\mathrm{SL}_1 \approx -10$ dB in the considered example. The IAA detectors expand this interval in SCNR: IAA-B by approximately 2 dB compared to the MF detector and IAA-A by 8 dB and 12 dB for $P_{FA} = 10^{-5}$ and $P_{FA} = 10^{-8}$ accordingly. It demonstrates that the ability of IAA to remove ambiguous responses of strong targets is also limited. The RELAX-like detector outperforms the other tests in a wide range of SCNR.

5.3.3 Multiple targets scenario

The scenario with two targets in the scene is considered to study the ability of the proposed techniques to declare the presence of multiple targets at their correct locations simultaneously. For the analysis here, a scenario with two point-like targets, moving at different velocities is considered, since the presence of more moving targets in one LRRS will rarely happen in reality (except observing a highway with multiple lines). Moreover, the targets are located at random locations and do not compete with each other (so, not located in the ambiguous sidelobes of each other), but can compete with clutter. The appropriate metric to compare the performance of the detectors in this case if the probability of correct set detection P_{CD}, defined in (5.38).

Two scenarios are considered. In the first case, two targets with $\mathrm{SCNR}_2 = \mathrm{SCNR}_1$ are present in the observed LRRS. Simulations results for this scenario are given in Fig. 5.4, which show probability of correct set detection P_{CD} vs SCNR of each target
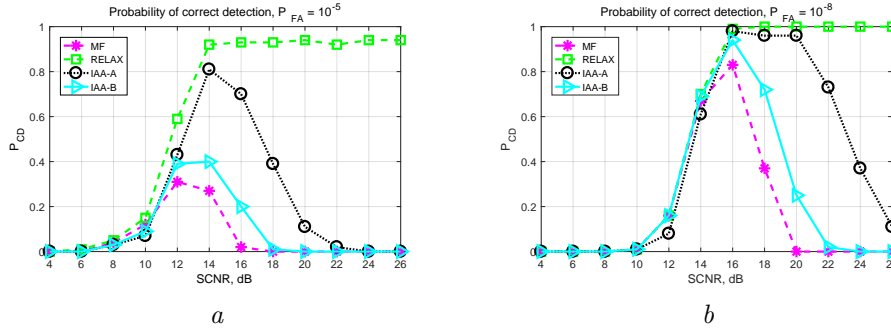
Figure 5.4: Probability of correct set detection vs SCNR for the scenario with two non-competing targets with equal SCNR: a - $P_{FA} = 10^{-5}$; b - $P_{FA} = 10^{-8}$.
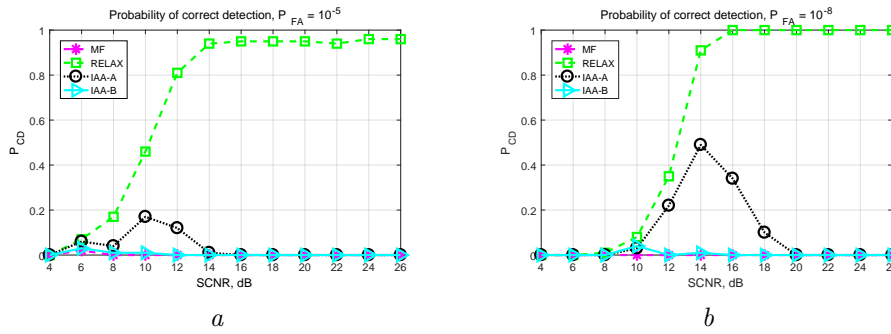

Figure 5.5: Probability of correct set detection vs SCNR for the scenario with two non-competing targets $\mathrm{SCNR}_2 = \mathrm{SCNR}_1 + 10$ dB: a - $P_{FA} = 10^{-5}$; b - $P_{FA} = 10^{-8}$.

for $P_{FA} = 10^{-5}$ and $P_{FA} = 10^{-8}$. The performance in presence of two targets shows some degradation compared to the scenario with a single target present in the scene (Fig. 5.3). Only the RELAX-like detector provides correct detection of the present targets when their SCNRs are high.

In the second case, one target is stronger than the other by 10 dB: $\mathrm{SCNR}_2 = \mathrm{SCNR}_1 + 10$ dB. Simulations results for the case of equal targets are given in Fig. 5.5, where the horizontal line corresponds to the SCNR of the weak target (SCNR_1). In this case, only the RELAX-like detector provides correct detection of both targets, while P_{CD} of the other detectors is low. Recall that the degradation of performance in Fig. 5.4, 5.5 is due to presence of ambiguous sidelobes in the detected map. The targets will be still detected according to the curves, shown in Fig. 5.2, but with multiple false detections at their ambiguous sidelobes.

5.4 Conclusion

In this chapter, the problem of detecting multiple targets in the observed low range resolution segment has been investigated. It has been demonstrated that conventional matched filter detector will suffer from multiple false detections at the ambiguous side-lobes of the real targets. The standard pick-the-peak detector cannot tackle this issue because of the possible presence of the other targets in the data vector. New techniques for detecting multiple targets in the received data vector are proposed, which preserve false alarm probability at the required level. These detectors demonstrate improved performance in terms of probability of correct targets detection compared to the conventional techniques. The proposed detector, exploiting RELAX estimation of the targets magnitudes, provides the best performance over the considered approaches in a wide range of targets SCNRs.
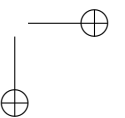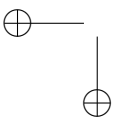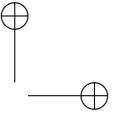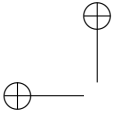
Chapter 6

Migrating target detection in high resolution ground clutter

In this chapter the detection of fast moving targets in the ambiguous-to-clutter (or blind) velocities is studied, considering specific aspects of the ground clutter being observed by a high resolution radar. Due to target migration, fast-moving targets compete with the clutter response from a few adjacent range cells during the CPI. In the high-resolution mode, the clutter power in these range cells can vary significantly along range; clutter is described by the compound-Gaussian model. The method to incorporate clutter power variation over range in the detector of a migrating target is investigated, and the benefits of applying this detector to migrating targets are evaluated.

6.1   Introduction

The ability of the modern radars to process coherently the waveform with a large bandwidth has significantly increased resolution capabilities of surveillance radars, thus providing additional possibilities for target detection and classification [2, 6, 21]. However, target detection in the high range resolution (HRR) mode has a few differences w.r.t. the detection in the low range resolution (LRR) mode. The targets become extended in range and have non-negligible range-walk during the CPI, but also the clutter probability distribution diverges from Gaussian, which lead to severe degradation of the detection algorithms, derived under the assumption of Gaussian clutter [21].

The Gaussian model of clutter, used in narrowband radars, is found not appli-

cable in the case of HRR. Multiple measurements campaigns, performed with different radars and in diverse conditions, have shown the deviation of the measured data statistic from the Gaussian model [21,34–37]. Empirical distributions of the clutter intensity were systematically observed to have larger tails than exponential distribution (intensity distribution in case of Gaussian clutter). Different multi-parametric distributions, including the Weibull, log-normal, and K distributions, have been adapted to accurately describe the data and derive efficient detectors [40, 74, 75]. However, those detectors miss unification, as completely different detection algorithms can be derived as optimal for the same data set, being described by different models e.g. by Weibull and K distributions.

A typical image of high resolution ground clutter is shown in Fig. 6.1. The radar image is recorded with the PARSAX radar, operating in S-band and providing range resolution of 1.58 meters[1]. It can be easily checked that clutter power varies over a large range of values and sometimes has abrupt changes in range. Such clutter behavior cannot be described with the Gaussian model of clutter, so more advanced modeling is required.

The modern trend is to represent high resolution radar clutter by the compound noise models (compound-Gaussian (CG) process, spherically invariant random vectors (SIRV)) which provide a mathematical tractable tool to deal with non-Gaussian clutter. The appearance of these models has been explained via the phenomenological scattering picture of high resolution radar: the number of scattering centers in the radar footprint cannot be assumed infinitely large anymore, so the central limit theorem is not applicable and, thus, Gaussian clutter model is not valid anymore. Accounting for the limited number of scattering centers in the radar footprint led to validation of K-distribution [38]. The further development of this idea results in the approach to model non-Gaussian radar clutter by a mixture of Gaussian distributions. Such model is called the CG model [21, 76, 77]. The compound models accurately describe the scattering phenomena of clutter for short observation times [21, 78]. Most distributions used to describe spiky clutter (including Weibull, K, Student and Gaussian distributions) can be shown in the form of CG model [21–23]. The main advantage of the CG model is its ability to separate clutter spectrum characteristics from its PDF, which allows significant simplification of the detection algorithms.

Radar detection of a point target in CG and SIRV models has been extensively studied during the last decades, resulting in a number of handful CFAR detectors for point targets [21, 23]. Algorithms for interference CM estimation from the reference CG data complement the aforementioned detectors and make them adaptive [21, 79]. The detection algorithms, being different, are still performed in the manner of the low-resolution radars – in each range cell. The estimated CM thus represents slow-time

---

[1]The detailed description of PARSAX radar is provided in Appendix A
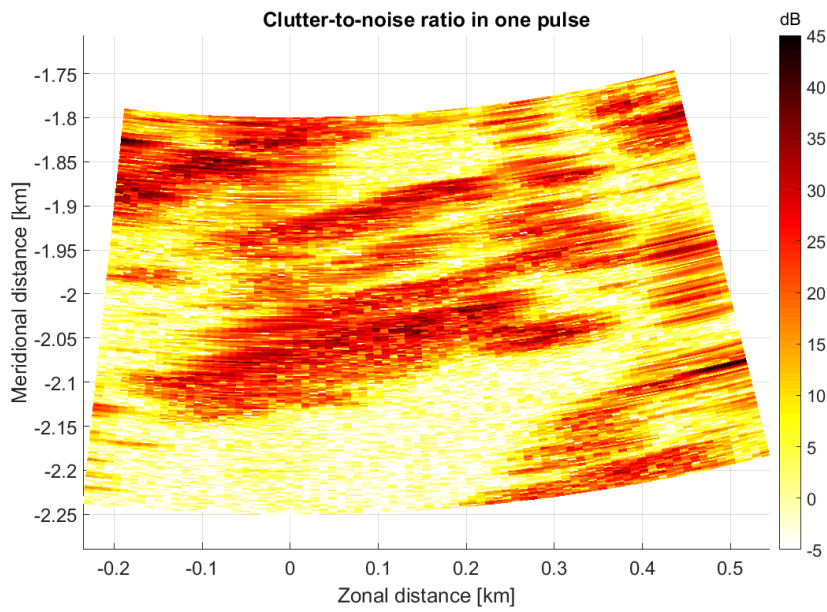
Figure 6.1: *a* - Clutter map of the park near Delft, *b* - Satellite image of the park from Google maps

spectrum characteristics of the competing clutter [21].

The targets of interest (planes, cars etc.), observed by a high-resolution radar, are well modeled as a set of independent point scatterers separated along the range [32].

That allows generalizing the developed algorithms for detection of range-extended (also called range-distributed) targets. Thus, the detection of range-extended targets has been first studied in case of homogeneous and locally-homogeneous Gaussian clutter [10]. Hereinafter, the clutter model with a constant texture in the block of range cells under test is reffered to as locally homogeneous clutter model [13]. Later, these detectors have been extended to the case of inhomogeneous clutter, modeled as SIRV [11, 12]. The assumption of independence between adjacent range cells under both hypotheses plays a key role in the development of the aforementioned detectors. In fact, it allows factorization of the decision test for an extended target in terms of single range cell statistics within the target extent [11, 12]. The possibility to include clutter range correlation has been discussed in [12] with the rather simplified model of CG clutter: texture is either completely correlated or uncorrelated between the range cells (in fact, clutter is simply grouped into the blocks with equal local power), the speckle components assumed uncorrelated between different range cells. Another approach to model target extension is applied for Doppler spread targets. In this case, the target response is modeled as a vector, which belongs to a particular subspace of known dimension [80]. The detector, in this case, is developed for the subspace signal [63]. An overview of detection techniques of range-extended targets can be found in [21].

Opposite to the target range extension, target range-walk has been commonly neglected in the detection literature. This assumption is usually justified by the use of a short CPI (a few ms) for detection in each burst, or by focusing the detection problem on slow-moving targets discrimination from static clutter. However, for the long CPI, considered herein, target migration cannot be neglected, especially for the targets at the ambiguous-to-clutter velocities. Recently, some detectors of range-migrating targets in Gaussian [54] and locally Gaussian clutter [13] have been proposed. These detectors require knowledge of the clutter correlation properties (via CM) in two dimensions: in range and slow-time. In other words, the detection of range-migrating targets requires clutter correlation in range to be considered. Thus, Dai et al. [13] showed that assumption of clutter independence between adjacent range cells leads to the non-CFAR performance of the adaptive (with estimated CM) detector for range-migrating targets. A similar observation has been made in the detection of a target crossing the clutter boundary [81]. At the same time, the analysis of HRR real data presented in [21, 37, 40, 82] suggests that radar ground clutter is correlated in range over a few range cells. Clutter spatial correlation was recently considered for slow-time CM estimation in HRR radar clutter [83] and detection of targets in range-oversampled data [84].

The main objective of this chapter is to derive a CFAR detector for the case of range-migrating target embedded in highly heterogeneous clutter following the CG model and to evaluate the benefits of applying CFAR detectors to migrating

targets. This chapter is organized as follows: in Section 6.2 the CG clutter model is recalled and the method to consider spatial correlation is introduced; then, in Sections 6.3 and 6.4 the detectors for the spatially uncorrelated and correlated clutter are derived accordingly. Section 6.5 considers detection of a range-migrating and range-extended target and Section 6.6 proposes a method for range / slow-time CM estimation from the reference data. The performance of the proposed techniques is assessed via numerical simulations in Section 6.7 and the major benefits of the proposed techniques are highlighted in Section 6.8.

6.2 Clutter model and problem formulation

6.2.1 Clutter model

The signature of a moving target, observed by the HRR radar requires target detection to be performed in a LRRS, contrary to the conventional detection in a single range cell. Accordingly, the CG clutter model, usually defined for a single range cell, has to be expanded to the LRRS. Clutter modeling in a few adjacent range cells is subject to different models of spatial correlation. Two clutter models have been considered so far [36,85]: independent interference model (IIM), assuming independent clutter from one range cell to another, and dependent interference model (DIM), which takes into account clutter correlation over range. In the following, the clutter model is defined for the DIM, while IIM is shown to be a particular case of the former.

The CG process $\mathbf{c}$ is the product of the square root of the positive scalar quantity τ, referred to as texture, and M-dimensional zero-mean complex Gaussian vector $\mathbf{g}$, called speckle [21]. The CG model, being a product of two random variables, gives three ways to model spatial correlation: considering either the speckle component or texture to be correlated over the range, or both of them. To choose between these three models of CG clutter, some results on detection of a range-migrating target in Gaussian clutter are recalled. The adaptive detector for this scenario involves the estimated CM of stacked bi-dimensional data in range and slow-time of size $KM \times KM$ [54]. The CG model can be considered as the extension of Gaussian model, which preserves the correlation properties of the former, and allows the power variation along the range. *Therefore, herein it is assumed for the CG clutter, that the speckle is correlated over the range, while the texture is independent from one range cell to another.* The independence of the texture is imposed for model tractability.

The clutter response in the LRRS can be represented by $K \times M$ matrix $\mathbf{C}$, its vectorized counterpart is $KM \times 1$ vector $\mathbf{c} = \text{vec}(\mathbf{C}^T)$, which is given element-wise by $\mathbf{c} = [c_0, c_1 \ldots c_{KM-1}]^T$. Hereinafter the clutter response in the k-th range cell is referred by the sub-vector of length M: $\mathbf{c_k} = [c_{kM}, \ldots, c_{(k+1)M-1}]^T$, so $\mathbf{c} = [\mathbf{c_0}^T, \mathbf{c_1}^T, \ldots, \mathbf{c_{K-1}}^T]^T$. Similar definition of subvectors holds for other $KM \times 1$

vectors.

The realization of clutter in the k-th range cell can be tackled as a realization of CG process, denoted by: $\mathbf{c_k} = \sqrt{\tau_k}\mathbf{g_k}$. In the LRRS, the speckle component is a KM-dimensional complex multivariate Gaussian vector with zero mean and known CM: $\mathbf{g} \sim \mathcal{CN}(\mathbf{0}_{KM}, \mathbf{Q})$. The speckle component in the k-th cell $\mathbf{g_k}$ is the subvector of $\mathbf{g}$, so it is an M-dimensional complex multivariate Gaussian vector, which complies with the CG model for $\mathbf{c_k}$. The PDF of speckle component in the LRRS $\mathbf{g}$ can be written in the form:

$$p(\mathbf{g}) = \frac{\exp\left(-\mathbf{g}^H\mathbf{Q^{-1}}\mathbf{g}\right)}{\pi^{KM}|\mathbf{Q}|} = \frac{\exp\left(-\sum_{i=0}^{K-1}\sum_{j=0}^{K-1}\mathbf{g_i}^H\mathbf{Q_{i,j}^{-1}}\mathbf{g_j}\right)}{\pi^{KM}|\mathbf{Q}|}, \qquad (6.1)$$

where notation $\mathbf{Q_{i,j}} = \mathbf{Q}_{iM\ldots(i+1)M-1,jM\ldots(j+1)M-1}$ defines $M \times M$ block of the speckle CM, $\mathbf{Q_{i,j}^{-1}}$ stands for the ith, j^{th} block of $\mathbf{Q^{-1}}$ and $\mathbf{Q}$ is a Hermitian positive definite matrix.

Due to the assumption of texture independence along range, conditional on texture covariance and cross-covariance matrices of clutter in the range cells of a LRRS are:

$$E\{\mathbf{c_i}\mathbf{c_j}^H|\tau_i, \tau_j\} = \sqrt{\tau_i\tau_j}E\{\mathbf{g_i}\mathbf{g_j}^H\} = \sqrt{\tau_i\tau_j}\mathbf{Q_{i,j}}. \qquad (6.2)$$

The conditional on $\sqrt{\tau_\mathcal{K}}$ PDF of CG clutter in the LRRS is:

$$p(\mathbf{c}|\sqrt{\tau_\mathcal{K}}) = \frac{\exp\left(-\sum_{i=0}^{K-1}\sum_{j=0}^{K-1}\frac{\mathbf{c_i}^H\mathbf{Q_{i,j}^{-1}}\mathbf{c_j}}{\sqrt{\tau_i\tau_j}}\right)}{\pi^{KM}|\mathbf{Q}|\prod_{k=0}^{K-1}\tau_k^M}, \qquad (6.3)$$

where $\mathcal{K} : k = 0\ldots K-1$. Generally, CG model is defined by a Gaussian vector conditional on texture τ_k, while here it is defined as conditional on the square root of the texture $\sqrt{\tau_k}$. Since texture is a positive scalar, the transformation between τ_k and $\sqrt{\tau_k}$ is unique; therefore, both parameterizations give equivalent representation.

The PDF of $\mathbf{c}$ is obtained from $p(\mathbf{c}|\sqrt{\tau_\mathcal{K}})$ by averaging over $\sqrt{\tau_\mathcal{K}}$ as follows:

$$p(\mathbf{c}) = E\{p(\mathbf{c}|\sqrt{\tau_\mathcal{K}})\} = \int_0^\infty \cdots \int_0^\infty \frac{1}{\pi^{KM}|\mathbf{Q}|\prod_{k=0}^{K-1}\tau_k^M}$$
$$\cdot\exp\left(-\sum_{i=0}^{K-1}\sum_{j=0}^{K-1}\frac{\mathbf{c_i}^H\mathbf{Q_{i,j}^{-1}}\mathbf{c_j}}{\sqrt{\tau_i\tau_j}}\right)\prod_{k=0}^{K-1}p_{\sqrt{\tau}}\left(\sqrt{\tau_k}\right)d\sqrt{\tau_1}\ldots d\sqrt{\tau_{K-1}}, \qquad (6.4)$$

where $p_{\sqrt{\tau}}\left(\sqrt{\tau_k}\right)$ denotes the PDF of $\sqrt{\tau_k}$. Note that the DIM clutter model (6.4) might look overcomplicated, but it satisfies the general requirement for the CG clutter, namely, if the clutter texture is equal in all the range cells (including the reference cells, not considered in (6.4)), the CG model degenerates to the Gaussian case.
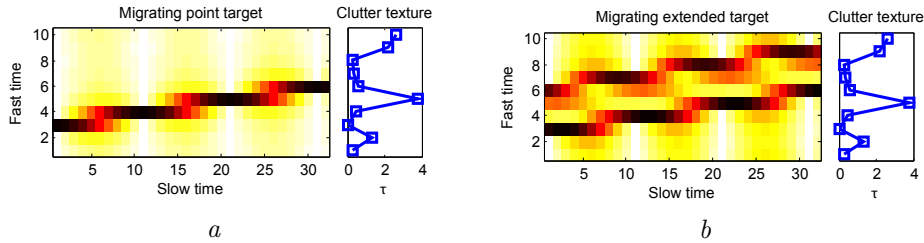
Figure 6.2: Detection scene in spiky clutter: a - range migrating point target; b - range migrating extended target (target response along range is random).

The PDF of clutter in the LRRS (6.4) includes multidimensional integration over interrelated variables $\sqrt{\tau_k}$ and therefore it does not provide a way to derive a detector directly. In order to design a practical detector, two simplifications are considered in the following sections separately:

- Clutter has no spatial correlation, so it satisfies IIM;

- Clutter texture is treated as an unknown nuisance parameter.

If both simplifications are applied together, the decision rule can be obtained as a special case of each detector, derived below.

6.2.2 Problem formulation

The scenario under consideration is shown in Fig. 6.2. Assume clutter dominated scenario, i.e. high CNR. Then $\mathbf{M} = E\left\{(\mathbf{c} + \mathbf{n})(\mathbf{c} + \mathbf{n})^H\right\} \approx E\left\{\mathbf{c}\mathbf{c}^H\right\}$ and the detection problem of a point target (Fig. 6.2 a) can be formulated as:

$$\mathbf{y_k} = \begin{cases} H_0: & \mathbf{c_k}, \\ H_1: & \alpha\mathbf{a_k} + \mathbf{c_k}, \end{cases} \qquad k = 0 \ldots K - 1, \qquad (6.5)$$

where α is a constant amplitude of a target in the LRRS under the hypothesis of its presence (H_1), $\mathbf{y_k}$, $\mathbf{c_k}$ and $\mathbf{a_k}$ are the sub-vectors, corresponding to the received data, the clutter and the target responses accordingly in the k-th range cell (fast-time sample, in Fig. 6.2, the k-th row is $\mathbf{a_k}$). The definition of the sub-vectors is identical to that of $\mathbf{c_k}$ given above.

In case of a range-extended target (Fig. 6.2, b), the detection problem can be formulated as:

$$\mathbf{y_k} = \begin{cases} H_0: & \mathbf{c_k}, \\ H_1: & \sum_{r \in \mathcal{R}} \alpha\mathbf{a_k}(r) + \mathbf{c_k}, \end{cases} \qquad k = 0 \ldots K - 1, \qquad (6.6)$$

where $\mathcal{R}$ is the set of the range cells, over which the target is spread, and $\mathbf{a_k}(r)$ have the same velocity v_0 (non-deformable target).

The design of a point target detector (6.5) is first considered. Then, the detector is generalized to the case of a range-extended target (6.6). The design of detectors in the next sections follows two-step procedure: first, a detector assuming known speckle CM is investigated, and then an adaptive detector is obtained, which utilizes speckle CM, estimated from the reference data set.

6.3 Migrating target detection in compound-Gaussian clutter - independent interference model

This section aims at the design of an optimal detector for migrating target in CG clutter, when clutter has no spatial correlation and the distribution of texture, given by $p_\tau(\tau_{\mathcal{K}})$ or, equivalently, $p_{\sqrt{\tau}}\left(\sqrt{\tau_{\mathcal{K}}}\right)$ is known *a priori*.

6.3.1 Assumptions

Assume clutter in the LRRS under test satisfies IIM, namely, the clutter vectors in different range cells are statistically independent. Statistical independence of clutter in adjunct range cells implies that both the speckle and the texture are uncorrelated over range, so the cross-covariance matrices of clutter (6.2) are zero matrices: $E\{\mathbf{c_i}\mathbf{c_j}^H\}|_{i\neq j} = \mathbf{0}_{M,M}$. Furthermore, assume clutter is homogeneous over range: $p(\mathbf{c_i}) = p(\mathbf{c_j})$, $\forall i,j \in \mathcal{K}$, which implies homogeneous texture: $p_{\sqrt{\tau}}\left(\sqrt{\tau_1}\right) = \ldots = p_{\sqrt{\tau}}\left(\sqrt{\tau_{K-1}}\right) = p_{\sqrt{\tau}}\left(\sqrt{\tau}\right)$ and homogeneous speckle component over range: $\mathbf{g_i} \sim CN(0,\mathbf{S})$, $\forall i \in \mathcal{K}$ [85]. To simplify the notations in this section the $M \times M$ speckle CM in slow-time is referred by $\mathbf{Q_{1,1}} = \ldots = \mathbf{Q_{K-1,K-1}} = \mathbf{S}$. The clutter CM in every range cells is then given by $E\{\mathbf{c_k}\mathbf{c_k}^H\} = E\{\tau_k\}\mathbf{S}$; and the CM of clutter in a LRRS has block-diagonal structure:

$$\mathbf{M} = \begin{bmatrix} E\{\tau_0\}\mathbf{S} & \mathbf{0}_{M,M} & \cdots & \mathbf{0}_{M,M} \\ \mathbf{0}_{M,M} & E\{\tau_1\}\mathbf{S} & \cdots & \mathbf{0}_{M,M} \\ \vdots & \vdots & \ddots & \vdots \\ \mathbf{0}_{M,M} & \mathbf{0}_{M,M} & \cdots & E\{\tau_{K-1}\}\mathbf{S} \end{bmatrix}. \tag{6.7}$$

Straightforward application of these assumptions to (6.3) and (6.4) results in the following PDF of clutter in the LRRS:

$$p(\mathbf{c}) = \prod_{k=0}^{K-1} p(\mathbf{c_k}) = \prod_{k=0}^{K-1} \int_0^\infty \frac{\exp\left(\tau_k^{-1}\mathbf{c_k}^H\mathbf{S^{-1}}\mathbf{c_k}\right)}{(\pi\tau_k)^M |\mathbf{S}|} p_\tau(\tau_k)\, d\tau_k, \tag{6.8}$$

which is simply a product of clutter PDFs in the K range cells under test, statistically
independent of each other.

Under hypothesis H_1 the PDF of the LRRS under test is derived from the PDF
under H_0 by setting the mean value of the Gaussian form to be equal to the present
signal $\mathbf{s} = \alpha\mathbf{a}$, where $\mathbf{a}$ is known steering vector and α is unknown, but constant
withing CPI complex amplitude of the target. The PDF of the LRRS under hypothesis
of target presence (H_1) is then written using the known steering vector of the target
in the k-th range cell $\mathbf{a_k}$ as:

$$f^{(1)}(\mathbf{y};\alpha) = \prod_{k=0}^{K-1} \int_0^\infty \frac{\exp\left(-\tau_k^{-1}(\mathbf{y_k} - \alpha\mathbf{a_k})^H \mathbf{S^{-1}}(\mathbf{y_k} - \alpha\mathbf{a_k})\right)}{(\pi\tau_k)^M |\mathbf{S}|} p_\tau(\tau_k)\, d\tau_k, \quad (6.9)$$

where the superscript in braces stands for the hypothesis index $H_i, i \in \{0,1\}$. To em-
phasize the dependence of PDF under H_1 on unknown target amplitude α, assuming
the received data vector $\mathbf{y}$ is fixed, it is referred hereinafter by the likelihood function
[86]. Its counterpart under H_0 can be obtained by: $f^{(0)}(\mathbf{y}) = f^{(1)}(\mathbf{y};\alpha)|_{\alpha=0}$.

6.3.2 Detector design

The detection problem (6.5) involves unknown target amplitude α. Therefore, the
GLRT is performed to derive a detector [49]:

$$\Lambda(\mathbf{y}) = \frac{\max_\alpha f^{(1)}(\mathbf{y};\alpha)}{f^{(0)}(\mathbf{y})} \underset{H_0}{\overset{H_1}{\gtrless}} T, \quad (6.10)$$

where T is the threshold calculated to ensure the desired probability of false alarm
(P_{FA}).

The kernel function of the CG model allows simplification of (6.9) under both
hypotheses in the following form, depending on the texture PDF [21, 36, 85]:

$$h_M(x) = \int_0^\infty \tau^{-M} \exp\left(-\frac{x}{\tau}\right) p_\tau(\tau)\, d\tau, \quad (6.11)$$

resulting in the following expression for the likelihood functions in the LRRS under
both hypothesis:

$$f^{(1)}(\mathbf{y};\alpha) = \frac{\prod_{k=0}^{K-1} h_M\left((\mathbf{y_k} - \alpha\mathbf{a_k})^H \mathbf{S^{-1}}(\mathbf{y_k} - \alpha\mathbf{a_k})\right)}{|\mathbf{S}|^K \pi^{KM}} \quad (6.12)$$

where $f^{(0)}(\mathbf{y}) = f^{(1)}(\mathbf{y};\alpha)|_{\alpha=0}$.

Next, the logarithm of likelihood function under H_1 is maximized over the un-
known deterministic target amplitude α by taking the derivative and setting it to

zero. It is done using the relation for derivative of function $h_M(x)$: $\partial h_M(x)/\partial x = -h_{M+1}(x)$ and constructing the function $c_M(x) = h_{M+1}(x)/h_M(x)$. Finally, the amplitude estimation has the form:

$$\hat{\alpha} = \frac{\displaystyle\sum_{k=0}^{K-1} c_M\left((\mathbf{y_k} - \hat{\alpha}\mathbf{a_k})^H \mathbf{S^{-1}}(\mathbf{y_k} - \hat{\alpha}\mathbf{a_k})\right)\mathbf{a_k}^H \mathbf{S^{-1}}\mathbf{y_k}}{\displaystyle\sum_{k=0}^{K-1} c_M\left((\mathbf{y_k} - \hat{\alpha}\mathbf{a_k})^H \mathbf{S^{-1}}(\mathbf{y_k} - \hat{\alpha}\mathbf{a_k})\right)\mathbf{a_k}^H \mathbf{S^{-1}}\mathbf{a_k}}. \tag{6.13}$$

The estimation $\hat{\alpha}$ is therefore defined by the transcendental equation (6.13) and requires iterative solution, subject to known PDF of the clutter texture $p_\tau(\tau)$. A convergence analysis of the iteration (6.13) is still the subject of the research; some useful properties of functions $c_M(x)$ and $h_M(x)$ can be found in [87]. In the simulations performed, the iteration (6.13) always converged, independently on its initialization.

The detection rule is then obtained by substitution of the estimation $\hat{\alpha}$ in (6.10):

$$\hat{\Lambda}(\mathbf{y}) = \prod_{k=0}^{K-1} \frac{h_M\left((\mathbf{y_k} - \hat{\alpha}\mathbf{a_k})^H \mathbf{S^{-1}}(\mathbf{y_k} - \hat{\alpha}\mathbf{a_k})\right)}{h_M\left(\mathbf{y_k}^H \mathbf{S^{-1}}\mathbf{y_k}\right)} \underset{H_0}{\overset{H_1}{\gtrless}} T. \tag{6.14}$$

The functions $c_M(x)$ and $h_M(x)$, considered above, are identical to the ones used for the speckle CM estimation [85] and for detection of non-migrating targets [23] in CG clutter with known PDF. For practical application this means that estimation of $\mathbf{S}$ and detection can be done on the same (or identical) chain.

6.3.3 Case study - K-distribution

A particular case of compound Gaussian distribution is K-distribution, regularly used to describe high resolution radar clutter [34, 37, 40]. In this case, the texture follows Gamma distribution:

$$p_\tau(\tau) = \frac{1}{\Gamma(\nu)}\left(\frac{\nu}{\mu}\right)^\nu \tau^{\nu-1}\exp\left(-\frac{\nu}{\mu}\tau\right)\mathbb{1}(\tau), \tag{6.15}$$

where $\mathbb{1}(x)$ is the Heaviside step function and $\Gamma(x)$ is the Gamma function; μ and ν are the scale and shape parameters of Gamma distribution respectively. Then the joint PDF of the LRRS can be expressed by substitution (6.15) into (6.11) and (6.12) and non-linear functions $h_M(x)$ and $c_M(x)$ can be written analytically:

$$h_M(x) = \frac{2x^{\frac{\nu-M}{2}}}{\Gamma(\nu)}\left(\frac{\nu}{\mu}\right)^{\frac{\nu+M}{2}} K_{\nu-M}\left(\sqrt{4\nu x/\mu}\right);$$

$$c_M(x) = \sqrt{\frac{\nu}{\mu x}}\frac{K_{\nu-M-1}\left(\sqrt{4\nu x/\mu}\right)}{K_{\nu-M}\left(\sqrt{4\nu x/\mu}\right)}. \tag{6.16}$$
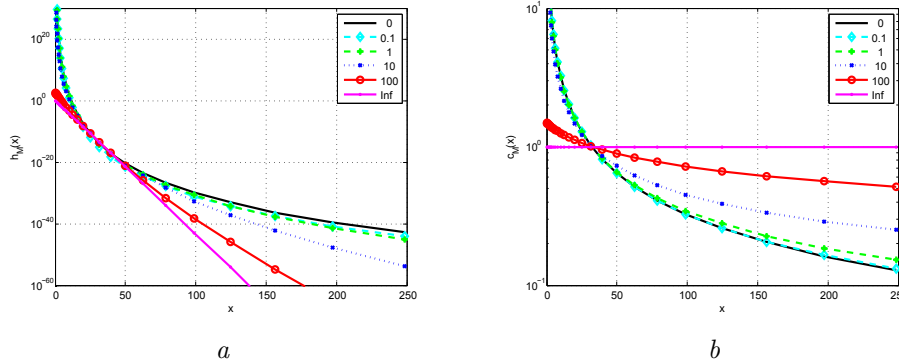
Figure 6.3: Weighting coefficients for different values of clutter shape ν, $M = 32$: a - $h_M(x)$, b - $c_M(x)$

with $K_n(x)$ being the modified Bessel function of the second kind. The plots of these functions $h_M(x)$ and $c_M(x)$ for different shaped of K-distribution are shown in Fig. 6.3 for $M = 32$ and $\mu = 1$. Analytical expression of functions $h_M(x)$ and $c_M(x)$ have been derived for a few heavy-tailed distributions, including Weibull and Student-t [22].

It is interesting to examine two extreme cases of K-distribution shape parameter, i.e. $\nu \to 0$ and $\nu \to \infty$. If $\nu \to \infty$, then the clutter tends to Gaussian distribution with power $p_\tau(\tau) = \delta(\tau - \mu)$, where μ is the known mean power of clutter. By definition (6.11), the function $h_M(x)$ reduces to $h_M^\infty(x) = \mu^{-M} \exp(-x/\mu)$, which is linear in a logarithmic scale, and, accordingly, $c_M(x)$ degenerates to a constant: $c_M^\infty(x) = \mu^{-1}$ (superscript of functions h_M and c_M stands for specific value of K-distribution shape parameter ν). As it can be expected, in this case, MLE of $\hat{\alpha}$ simplifies to its form in Gaussian interference:

$$\hat{\alpha} = \frac{\sum_{k=0}^{K-1} \mathbf{a_k}^H \mathbf{S^{-1}} \mathbf{y_k}}{\sum_{k=0}^{K-1} \mathbf{a_k}^H \mathbf{S^{-1}} \mathbf{a_k}} = \frac{\mathbf{a}^H \mathbf{Q^{-1}} \mathbf{y}}{\mathbf{a}^H \mathbf{Q^{-1}} \mathbf{a}}, \tag{6.17}$$

where the second representation uses the speckle CM in the LRRS (6.1). Straightforward simplification of the GLRT (6.14) by means of (6.17) leads to the following decision rule:

$$\ln\left(\hat{\Lambda}(y)\right) = \frac{\left|\mathbf{a}^H \mathbf{Q^{-1}} \mathbf{y}\right|^2}{\mu \; \mathbf{a^H Q^{-1} a}}, \tag{6.18}$$

which is a general form of a scale-invariant detector considered in [63]. The particular case of clutter scale parameter $\mu = 1$ then degenerates to the Matched Filter detector (5.5).

The other limiting case appears when $\nu \to 0$. Gamma PDF is not defined for $\nu \to 0$, but tends to have non-informative PDF of the texture. A possible non-informative prior can be flat over all possible values of τ bounded above by τ_{max}: $p_\tau(\tau) = (\mathbb{1}(0) - \mathbb{1}(\tau_{max}))/\tau_{max}$. Setting the upper limit of the integral in (6.11) to τ_{max} and solving it for $\tau_{max} \to +\infty$ (by changing the variable $z = 1/\tau$ and using eq. 3.351.3 of [88]), it is possible to find the resulting functions $h_M^0(x) = \Gamma(M)\,x^{-M}$ and $c_M^0(x) = M/x$. The plots of these functions with $\mu = 1$ are also shown in Fig. 6.3 for comparison. The amplitude estimation then reduces to:

$$\hat{\alpha} = \frac{\sum_{k=0}^{K-1} \frac{\mathbf{a_k}^H \mathbf{S}^{-1} \mathbf{y_k}}{(\mathbf{y_k}-\hat{\alpha}\mathbf{a_k})^H \mathbf{S}^{-1}(\mathbf{y_k}-\hat{\alpha}\mathbf{a_k})}}{\sum_{k=0}^{K-1} \frac{\mathbf{a_k}^H \mathbf{S}^{-1} \mathbf{a_k}}{(\mathbf{y_k}-\hat{\alpha}\mathbf{a_k})^H \mathbf{S}^{-1}(\mathbf{y_k}-\hat{\alpha}\mathbf{a_k})}} \tag{6.19}$$

and the GLRT (6.14) has the form:

$$\hat{\Lambda}(\mathbf{y}) = \prod_{k=1}^{K} \left(\frac{(\mathbf{y_k} - \hat{\alpha}\mathbf{a_k})^H \mathbf{S}^{-1} (\mathbf{y_k} - \hat{\alpha}\mathbf{a_k})}{\mathbf{y_k}^H \mathbf{S}^{-1} \mathbf{y_k}} \right)^{-M} \underset{H_0}{\overset{H_1}{\gtrless}} T. \tag{6.20}$$

Note that in case of any value of $\nu < +\infty$ (so, except of the Gaussian clutter), the estimation of $\hat{\alpha}$ is defined by the transcendental equation, and so it has to be solved iteratively.

Further note that the detector given by (6.19) and (6.20) does not involve distribution-dependent functions h_M and c_M explicitly. This result, obtained with the non-informative prior of texture is equivalent to considering clutter texture as an additional unknown parameter, instead of random quantity with a given PDF $p_\tau(\tau)$. Therefore, the detection rule, given by (6.19) and (6.20), is the distribution-free test for the IIM of clutter.

6.4   Migrating target detection in compound-Gaussian clutter - dependent interference model

6.4.1   Assumptions

When range correlated clutter is considered, the assumption of homogeneous texture in (6.4) does not simplify the problem considerably. Namely, the multiple integral cannot be factorized in terms of functions $h_M(x)$ and $c_M(x)$, given above; so the derivation of the likelihood ratio from (6.4) seems intractable even for known PDFs [21].

The way to overcome this limitation is to consider each texture as an unknown deterministic parameter to be estimated in the GLRT. The same strategy is usually employed for non-migrating target detection to obtain the distribution-free test.

It has been shown in [23] that for moderate number of pulses in CPI ($M > 16$)
the performance of the distribution-free detector approaches the performance of the
distribution-aware one. Moreover, the target range-walk can be observed only for
large M, therefore, from this point on, the texture is regarded as an unknown con-
stant and denoted by σ_k^2.

As follows from the problem formulation and clutter model, the detection problem
(6.5) involves unknown parameters $\sigma_{\mathcal{K}}^2$ and α. In order to derive a detector the GLRT
is performed:

$$\Lambda(\mathbf{y}) = \frac{\max_{\sigma_{\mathcal{K}}, \alpha} f^{(1)}(\mathbf{y}; \sigma_{\mathcal{K}}, \alpha)}{\max_{\sigma_{\mathcal{K}}} f^{(0)}(\mathbf{y}; \sigma_{\mathcal{K}})}. \tag{6.21}$$

The likelihood function of the LRRS under H_1 is:

$$f^{(1)}(\mathbf{y}; \sigma_{\mathcal{K}}, \alpha) = \frac{\exp\left(-\sum_{i=0}^{K-1} \sum_{j=0}^{K-1} \frac{(\mathbf{y_i} - \alpha \mathbf{a_i})^H \mathbf{Q_{i,j}^{-1}} (\mathbf{y_j} - \alpha \mathbf{a_j})}{\sigma_i \sigma_j}\right)}{\pi^{KM} |\mathbf{Q}| \prod_{k=0}^{K-1} \sigma_k^{2M}}. \tag{6.22}$$

and similarly $f^{(0)}(\mathbf{y}; \sigma_{\mathcal{K}}) = f^{(1)}(\mathbf{y}; \sigma_{\mathcal{K}}, \alpha)|_{\alpha=0}$.

6.4.2 Detector design

First, find the estimation of $\sigma_{\mathcal{K}}$ under both hypotheses by maximizing the loga-
rithm of (6.22) w.r.t. each $\sigma_k, k \in \mathcal{K}$. To simplify further derivations, denote
$q_{i,j}^{(1)} = (\mathbf{y_i} - \alpha \mathbf{a_i})^H \mathbf{Q_{i,j}^{-1}} (\mathbf{y_j} - \alpha \mathbf{a_j})$ and $q_{i,j}^{(0)} = \mathbf{y_i}^H \mathbf{Q_{i,j}^{-1}} \mathbf{y_j}$, where $i, j \in \mathcal{K}$. Then the
sum in the exponential term of (6.22) can be expressed as:

$$\sum_{i=0}^{K-1} \sum_{j=0}^{K-1} \frac{q_{i,j}^{(H)}}{\sigma_i \sigma_j} = \frac{q_{k,k}^{(H)}}{\sigma_k^2} + 2\Re\left(\sum_{j=0,j\neq k}^{K-1} \frac{q_{k,j}^{(H)}}{\sigma_k \sigma_j}\right) + \sum_{i=0,i\neq k}^{K-1} \sum_{j=0,j\neq k}^{K-1} \frac{q_{i,j}^{(H)}}{\sigma_i \sigma_j}. \tag{6.23}$$

Note that $q_{k,j}^{(H)}$ is independent of $\sigma_{\mathcal{K}}$; and that the last item in (6.23) represents terms
independent of the data in the k-th range cell. The estimation of σ_k is found by
taking the derivative of logarithm of (6.22) w.r.t. σ_k using (6.23) and setting it to
zero. Then, the estimation of $\sigma_k^{(H)}$ is obtained as the positive solution of the quadratic
equation:

$$\left(\sigma_k^{(H)}\right)^2 - \sigma_k^{(H)} \sum_{j=0,j\neq k}^{K-1} \frac{\Re\left(q_{k,j}^{(H)}\right)}{M\sigma_j^{(H)}} - \frac{q_{k,k}^{(H)}}{M} = 0, \tag{6.24}$$

which is dependent on $\sigma_{j\in\mathcal{K}, j\neq k}^{(H)}$ and it also depends on α under H_1 via $q_{k,j}^{(1)} = q_{k,j}^{(1)}(\alpha)$.
The likelihood function (6.22) for the K range cells in the LRRS depends on K

independent unknowns $\sigma_{\mathcal{K}}$, and results in K interrelated equations in the form of (6.24) under each hypothesis.

By denoting: $b_k^{(H)} = - \sum_{j=0, j \neq k}^{K-1} \left(M \sigma_j^{(H)} \right)^{-1} \Re(q_{k,j}^{(H)})$ and $c_k^{(H)} = -q_{k,k}^{(H)}/M$, it is easy to show that each of K equations always (under any hypothesis $H_i, i \in \{0,1\}$, with any realization of data $q_{k,j}^{(H)}$ and any assumption on $\sigma_{j \in \mathcal{K}, j \neq k}^{(H)}$) has two real roots, as $\left(b_k^{(H)} \right)^2 - 4 c_k^{(H)} > 0, \forall k \in \mathcal{K}$. Moreover, from Vieta's formula for the second-order polynomial, it follows that the roots of (6.24) satisfy $\sigma_k^{[1]} \sigma_k^{[2]} = c_k < 0$, so only one root is positive, which is the one of interest. Therefore, each equation for $\sigma_k^{(H)}$ has a unique solution, which can be obtained given all the other parameters are fixed:

$$\hat{\sigma}_k^{(H)} = g_k^{(H)} \left(\hat{\sigma}_{j \in \mathcal{K}, j \neq k}^{(H)} \right), \tag{6.25}$$

where

$$g_k^{(H)} \left(\hat{\sigma}_{j \in \mathcal{K}, j \neq k}^{(H)} \right) = \frac{1}{2} \left(-b_k^{(H)} + \sqrt{\left(b_k^{(H)} \right)^2 - 4 c_k^{(H)}} \right). \tag{6.26}$$

Then, under H_0, the system of K equations $\hat{\sigma}_k^{(0)} = g_k^{(0)} \left(\hat{\sigma}_{j \in \mathcal{K}, j \neq k}^{(0)} \right)$ of the form (6.25) for K unknowns $\sigma_{\mathcal{K}}$ is built and it can be solved iteratively by the fixed point iteration for a system of equations.

Similarly, under H_1, K equations for σ_k (6.25) are defined: $\hat{\sigma}_k^{(1)} = g_k^{(1)} \left(\hat{\sigma}_{j \in \mathcal{K}, j \neq k}^{(1)}, \alpha \right)$, which depend on $K + 1$ unknowns: $\sigma_{\mathcal{K}}$ and α. The last equation for the system under H_1 provides the estimation of amplitude α in the canonical form:

$$\hat{\alpha} = \frac{\mathbf{a}^H \left(\hat{\mathbf{M}}^{(1)} \right)^{-1} \mathbf{y}}{\mathbf{a}^H \left(\hat{\mathbf{M}}^{(1)} \right)^{-1} \mathbf{a}}, \tag{6.27}$$

where the matrix $\hat{\mathbf{M}}^{(1)}$ is defined according to the clutter model (6.2):

$$\mathbf{M} = \begin{bmatrix} \sigma_0^2 \mathbf{Q_{0,0}} & \cdots & \sigma_0 \sigma_{K-1} \mathbf{Q_{0,K-1}} \\ \vdots & \ddots & \vdots \\ \sigma_{K-1} \sigma_0 \mathbf{Q_{K-1,0}} & \cdots & \sigma_{K-1}^2 \mathbf{Q_{K-1,K-1}} \end{bmatrix}. \tag{6.28}$$

with $\sigma_{\mathcal{K}}$ being substituted with their estimates under hypothesis H_1, so: $\hat{\mathbf{M}}^{(H)} = \mathbf{M}|_{\sigma_{\mathcal{K}} = \hat{\sigma}_{\mathcal{K}}^{(H)}}$. The K equations for $\hat{\sigma}_k^{(1)}$ (6.25) and one for $\hat{\alpha}$ form the system of $K + 1$ equations with $K + 1$ unknowns, to be solved similarly to that under H_0.

In order to perform detection, the estimations $\hat{\sigma}_k^{(0)}, \hat{\sigma}_k^{(1)}$ and $\hat{\alpha}$ should be substituted into the GLRT. However, straightforward substitution of estimators (6.25)

6.4 Migrating target detection in compound-Gaussian clutter - dependent
interference model 111

and (6.27) into the likelihood ratio (6.21) leads to a bulky form of the decision
rule. To derive a compact representation, rewrite equation (6.24) in terms of
$\hat{\mu}_{k,j}^{(H)} = (\hat{\sigma}_k^{(H)} \hat{\sigma}_j^{(H)})^{-1} q_{k,j}^{(H)}$ as:

$$\sum_{j=0,j\neq k}^{K-1} \Re\left(\hat{\mu}_{kj}^{(H)}\right) + \hat{\mu}_{kk}^{(H)} = M. \tag{6.29}$$

Then, the exponential term of the likelihood function under each hypothesis (6.23) is:

$$\sum_{k=0}^{K-1} \sum_{j=0}^{K-1} \frac{q_{k,j}^{(H)}}{\hat{\sigma}_k^{(H)} \hat{\sigma}_j^{(H)}} = \sum_{k=0}^{K-1} \left(\hat{\mu}_{kk}^{(H)} + \sum_{j=0,j\neq k}^{K-1} \hat{\mu}_{kj}^{(H)}\right) = KM, \tag{6.30}$$

where the second equality holds because of (6.29) and Hermitian structure of the
clutter CM. Consequently, the exponential term of the likelihood functions (6.22)
does not affect the detection. The GLRT has a form:

$$\Lambda(\mathbf{y}) = \prod_{k=0}^{K-1} \left(\frac{\hat{\sigma}_k^{(0)}}{\hat{\sigma}_k^{(1)}}\right)^{2M} \underset{H_0}{\overset{H_1}{\gtrless}} T, \tag{6.31}$$

where T is the threshold to satisfy the appropriate probability of false alarm P_{FA}.

The convergence of the iterative estimator (6.25) and its approximate solution
with a lower computational burden are discussed in the Appendices D.1 and D.2
accordingly.

The clutter model, given above gives the maximum fidelity to represent clutter
variation over the range. However, in some scenarios, such flexibility of the model
is not required and can be traded for a more efficient implementation. Obviously,
the most straightforward assumption to be considered is clutter independence from
one range cell to another, so IIM, which implies $b_{\mathcal{K}}^{(H)} = \mathbf{0}_K$ and the decision rule
degenerates to the test derived above by equations (6.19) and (6.20). More generally,
the clutter can be assumed to have a boundary between two non-overlapping regions
with different power, modeled in terms of SIRVs. The scenarios of interest, where
such simplification can be made, include homogeneous clutter with an outlier in one
or a few adjacent range cells e.g. due to the presence of an electricity pylon or mast;
or clutter transition between two regions, e.g. between a field and a forest. The
detector for such scenario can have a simplified form of (6.31), given in Appendix
D.3. However, the latter detector requires knowledge of the clutter boundary between
two regions, and thus it less adaptive to the radar scene. Possible implementation
of such detector might include construction of the clutter map of surrounding clutter
and further estimation of the clutter boundaries from that map using an appropriate
edge detection technique (e.g. Canny or Sobel's edge detectors [89]). Similar clutter
scenario has been considered in [81], where the authors developed a few detectors for
the case of IIM, with a block-diagonal CM in the LRRS under test.

6.5 Extended target detector

The targets of interest, observed in HRR radar mode (with a meter or sub-meter range resolution), become extended in range. Because of the target migration and also the clutter correlation in range, the key assumption of [11, 12] on data independence in adjacent range cells is obviously not valid. Therefore, for the detection of range-extended targets with the range-walk the theory of subspace detectors [63] is adopted here. Assume the target vectorized signal $\mathbf{s}$ lies in the subspace of dimension R: $\boldsymbol{\Psi} = [\mathbf{a}(0), \ldots, \mathbf{a}(R-1)]$, so $\mathbf{s} = \boldsymbol{\Psi}\boldsymbol{\alpha}$, where $\boldsymbol{\alpha} = [\alpha_0, \ldots, \alpha_{R-1}]^T$. Since the target extension in range is considered, the subspace vectors correspond to the target steering vectors at different range cells k_0, but with the same velocity v_0 in (2.23). The reflection from the moving parts of the target, such as wheels, blades etc, is neglected.

Denote by $\mathbf{s}$ the signature of the extended target in the LRRS (instead of $\alpha\mathbf{a}$ for a point target). The quadratic form under H_1 then becomes $q_{i,j}^{(1)} = (\mathbf{y_i} - \mathbf{s_i})^H \mathbf{Q_{i,j}^{-1}} (\mathbf{y_j} - \mathbf{s_j})$, where $\mathbf{s_i}$ is the sub-vector of the target signal in the i-th range cell. With that modification, the estimation of $\hat{\sigma}_{\mathcal{K}}^{(H)}$ has the same form as above, i.e. (6.24).

The estimation of $\hat{\boldsymbol{\alpha}}$ can be found by maximizing the likelihood function w.r.t. each element of $\boldsymbol{\alpha}$ in the form:

$$\hat{\alpha}_r = \frac{\mathbf{a}^H(r) \left(\hat{\mathbf{M}}^{(1)}\right)^{-1} \left(\mathbf{y} - \sum_{j=0, j \neq r}^{R-1} \hat{\alpha}_j \mathbf{a}(j)\right)}{\mathbf{a}^H(r) \left(\hat{\mathbf{M}}^{(1)}\right)^{-1} \mathbf{a}(r)}. \tag{6.32}$$

Therefore, for detection of a target spread over R range cells, the detector under H_1 uses K estimation of $\hat{\sigma}_{\mathcal{K}}^{(1)}$ with the modification, described above, and R equations for $\hat{\alpha}_r$. Thus the estimations of parameters are the solutions of the system of $K+R$ equations with $K+R$ independent unknowns, to be solved iteratively. The detection rule for the range-extended target can be shown in the form (6.31) with the appropriate definition of $q_{i,j}^{(1)}$.

Note, that in general, the signal subspace is not known in advance. So, to make such a detector applicable, some assumption on the target extent should be made based on the prior knowledge of the scene or extracted from the data using some model order selection techniques, e.g. [90].

6.6 Covariance matrix estimation and adaptive detection

In the previous section, it was assumed that slow-time/range speckle CM $\mathbf{Q}$ is known *a priori*, which is generally not the case in real applications. A practical strategy to overcome this limitation is to substitute known CM with its estimation from the secondary data [21].

In Gaussian clutter, the sample CM is known to be the MLE of CM (e.g. [55]), and it is used in the corresponding adaptive detectors [64,65]. The aforementioned detectors consider CM estimation in a single range cell; in Gaussian clutter the extension to the LRRS is straightforward. In CG clutter, the ML estimation of slow-time CM is defined as the solution of the transcendental equation [85,87,91], which requires the knowledge of texture PDF. The distribution-free CM estimator, called approximate ML (AML) estimator [85,92], is obtained assuming clutter texture in each reference range cell is a deterministic unknown parameter. This estimator can be applied directly for the estimation of the slow-time speckle CM, required for the IIM detector. In case of DIM, range/slow-time CM can be derived in a similar manner only under the assumption of locally homogeneous environment. Herein inhomogeneous clutter in the reference cells is considered, which follows the model of Section 6.2, and a new algorithm for range/slow-time speckle CM estimation from that reference data is proposed.

Assume $L > KM$ independent and target free reference LRRSs with homogeneous speckle component are available. The received data in the l-th reference cell $\mathbf{z}(l) = [z_0(l), z_1(l), \ldots, z_{KM-1}(l)]^T$ can be arranged by the range cells as: $\mathbf{z}(l) = [\mathbf{z_0}^T(l), \mathbf{z_1}^T(l), \ldots, \mathbf{z_{K-1}}^T(l)]^T$. The speckle component of $\mathbf{z}(l)$ is a complex Gaussian KM vector $\mathbf{g}(l) \sim \mathcal{CN}(\mathbf{0}_{KM}, \mathbf{Q})$, and the texture is $\sigma_{\mathcal{K}}(l)$. The received data in the l-th reference LRRSs then can be modeled by: $\mathbf{z}(l) = \mathbf{W}(l)\mathbf{g}(l)$, where $\mathbf{W}(l) = \mathrm{diag}\,(\sigma_0(l), \ldots, \sigma_{K-1}(l)) \otimes \mathbf{I}_M$ represents the realizations of the texture in the reference LRRS l, constant over slow-time. The clutter in the reference LRRS l is complex Gaussian KM vector $\mathbf{z}(l)|_{\mathbf{W}(l)} \sim \mathcal{CN}(\mathbf{0}_{KM}, \mathbf{M}(l))$, conditional on the texture realization via:

$$\mathbf{M}(l) = E\{\mathbf{z}(l)\mathbf{z}^H(l)\} = \mathbf{W}(l)E\{\mathbf{g}(l)\mathbf{g}^H(l)\}\mathbf{W}(l) = \mathbf{W}(l)\mathbf{Q}\mathbf{W}(l). \qquad (6.33)$$

Given the structure of clutter CM in the l-th LRRS, the two-step maximization procedure of [85] is adopted for the range slow-time speckle CM estimation from the reference data set.

At the first step of maximization, the texture estimates $\hat{\sigma}_{\mathcal{K}}(l)$ are provided for all the reference LRRSs: $\forall l \in \mathcal{L}$, where $\mathcal{L} : l = 0, \ldots, L-1$. Then, speckle CM is estimated by:

$$\hat{\mathbf{Q}} = \frac{1}{L} \sum_{l=0}^{L-1} \hat{\mathbf{W}}^{-1}(l)\mathbf{z}(l)\mathbf{z}^H(l)\hat{\mathbf{W}}^{-1}(l), \qquad (6.34)$$

with $\hat{\mathbf{W}}(l) = \mathbf{W}(l)|_{\sigma_{\mathcal{K}}(l)=\hat{\sigma}_{\mathcal{K}}(l)}$.

At the second step, the speckle CM estimation $\hat{\mathbf{Q}}$ is fixed to obtain the MLE of $\sigma_k(l), \forall k \in \mathcal{K}, \forall l \in \mathcal{L}$. The estimation of $\sigma_k(l), \forall k \in \mathcal{K}$ in each LRRS l corresponds to the estimation of $\hat{\sigma}_k$ under H_0 and obtained via (6.25) iteratively. The involved

---

Algorithm 1 Range/slow-time covariance matrix estimation in CG clutter

---

1: Initialize: $\hat{\mathbf{Q}}(0), I_Q, I_\sigma, \sigma_{\mathcal{K}}(\mathcal{L})$

2: **for** $i_Q = 1, I_Q$ **do**   // Loop of CM estimation

3:    **for** $i_\sigma \leftarrow 1, I_\sigma$ **do**   // Loop of $\sigma_k(l)$ estimation

4:       $\hat{\sigma}_k(l) \leftarrow g_k^{(0)}\left(\hat{\sigma}_{j\in\mathcal{K},j\neq k}(l), \hat{\mathbf{Q}}(i_Q-1)\right), \forall k \in \mathcal{K}, \forall l \in \mathcal{L}$ // Eqn. (6.25)

5:    **end for**

6:    $\hat{\mathbf{W}}(l) \leftarrow \text{diag}\left(\hat{\sigma}_{\mathcal{K}}(l)\right) \otimes \mathbf{I}_M, \forall l \in \mathcal{L}$

7:    $\hat{\mathbf{Q}}(i_Q) \leftarrow \frac{1}{L}\sum_{l=0}^{L-1} \hat{\mathbf{W}}^{-1}(l)\mathbf{z}(l)\mathbf{z}^H(l)\hat{\mathbf{W}}^{-1}(l)$ // Update CM, eqn. (6.34)

8:    $\hat{\mathbf{Q}}(i_Q) \leftarrow \frac{\hat{\mathbf{Q}}(i_Q)}{\text{Tr}(\hat{\mathbf{Q}}(i_Q))}$

9: **end for**

10: $\hat{\mathbf{Q}} \leftarrow \hat{\mathbf{Q}}(i_Q)$ // Output

---

parameters $b_k^{(0)}(l)$ and $c_k^{(0)}(l)$ are the functions of the known data in the reference cell $\mathbf{z}(l)$ and unknown parameters $\hat{\sigma}_{j\in\mathcal{K},j\neq k}$ and $\hat{\mathbf{Q}}$, to be jointly estimated. In short, it can be written as:

$$\hat{\sigma}_k(l) = g_k^{(0)}\left(\hat{\sigma}_{j\in\mathcal{K},j\neq k}(l), \hat{\mathbf{Q}}\right). \tag{6.35}$$

So the algorithm for the range slow-time speckle CM estimation involves two nested loops. The inner loop updates the texture estimation in all the reference LRRSs by means of (6.35); and the outer loop updates the speckle CM by means of (6.34). The pseudo-code of the algorithm is listed in Algorithm 1.

A few comments are in order regarding the Algorithm 1. First, the algorithm should be initialized with some estimation of CM **Q**. If no prior knowledge about textures is available, the reasonable choice is the sample SCM:

$$\hat{\mathbf{Q}}_{\text{SCM}} = \frac{1}{L}\sum_{l=0}^{L-1} \mathbf{z}(l)\mathbf{z}^H(l), \tag{6.36}$$

however, other choices, such as identity matrix or random matrix, are possible [92]. Second, the number of iterations in the outer loop $I_{\mathbf{Q}}$ can be limited to a few [85], since the further improvement in CM estimation has a minor effect on detection performance. Third, the iterative procedure in the inner loop might be initialized with $\hat{\sigma}_{\mathcal{K}}(\mathcal{L})$ obtained at the previous step of the outer loop and then estimated in a few iterations I_σ. The latter relies on the fact that $\hat{\mathbf{Q}}$ does not vary significantly from one iteration to another. Note, that each loop can be stopped when the corresponding convergence criteria, such as [85,92], is satisfied. Forth, the iterative estimation (6.34) is normalized by $\text{Tr}(\hat{\mathbf{Q}})$ at each iteration for the identification reasons [85,92].

The adaptive detector has the form defined above, namely (6.31), where the known matrix **Q** is substituted with its estimation from the reference dataset $\hat{\mathbf{Q}}$.

Some criticism can be raised against the possibility to estimate the CM $\hat{\mathbf{Q}}$ in real applications, since the number of reference cells required to obtain its estimation might be large, in comparison to that in the conventional radars. Thus, assume the clutter is Gaussian, the loss in detection using estimated CM will follow the rule of Reed, Mallett and Brennan (RMB rule) [93], which says that to ensure 3 dB loss in detection performance due to CM estimation, $2KM$ independent LRRSs, or $2K^2M$ range cells, should be used for the estimation. The number of the reference cells is large, but translated in meters it is equivalent to a few hundred meters, which is comparable to the existing narrowband systems. For example, the standard surveillance radar transmits 20 pulses in a burst with the bandwidth $B = 5$ MHz, so $\delta_R = 30$ m. According to RMB rule, for 3-dB loss in detection, 40 reference range cells are required, which is equivalent to 1200 m. The same scene observed with $\delta_R = 0.3$ m (500 MHz BW) would result in 4000 reference cells. The condition for similar performance is $K^2M = 2000$, which can be satisfied in some scenarios (depending on $v_{\max}$). Further reduction of the reference data and computational complexity can be obtained using structured CM estimation techniques, e.g. [94, 95].

6.7 Simulation results and discussion

In this section, the performance of the proposed algorithms is assessed by numerical simulations. The parameters of the radar are fixed to: $f_c = 10$ GHz, $B = 1$ GHz ($\delta_R = 0.15$ m), $T_r = 1$ ms, $M = 32$. The maximum expected velocity of a target is set to: $|v_0| \leq v_{max} = 1.5v_a = c/(2f_cT_r) = 22.5$ m/s; for a point target detection we set $K = 6$ to satisfy (2.14). The constraint on the maximum velocity is set to reduce the computational time of the numerical simulations.

The texture components $\tau_{\mathcal{K}}^2$ follows Gamma distribution, so the clutter follows the K-distribution, a special case of CG; the shape parameter and the scale parameter are fixed to $\nu = 0.5$ and $\mu = 1$ accordingly. The speckle CM has the structure $\mathbf{Q} = \mathbf{D} \otimes \mathbf{S}$, so the speckle correlation in slow-time is defined by $M \times M$ matrix $\mathbf{S}$ and in range by $K \times K$ matrix $\mathbf{D}$.

For P_{FA} and P_D assessment, 10^6 and 10^3 Monte-Carlo trials are performed accordingly.

6.7.1 Detector for independent interference model

Convergence analysis and false alarm regulation First, the convergence of the proposed iterative amplitude estimation, involved in the decision test, is studied. Two amplitude estimators are considered: the estimator relying on the known PDF of texture (6.13) and the distribution-free estimator (6.19). The convergence is studied
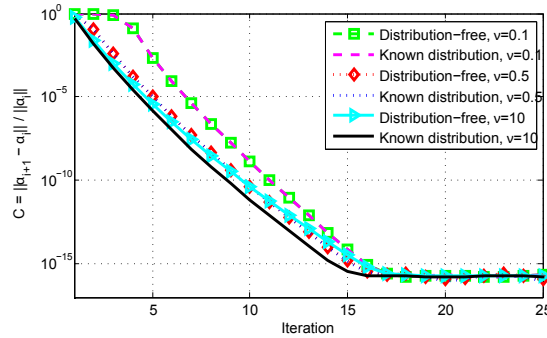
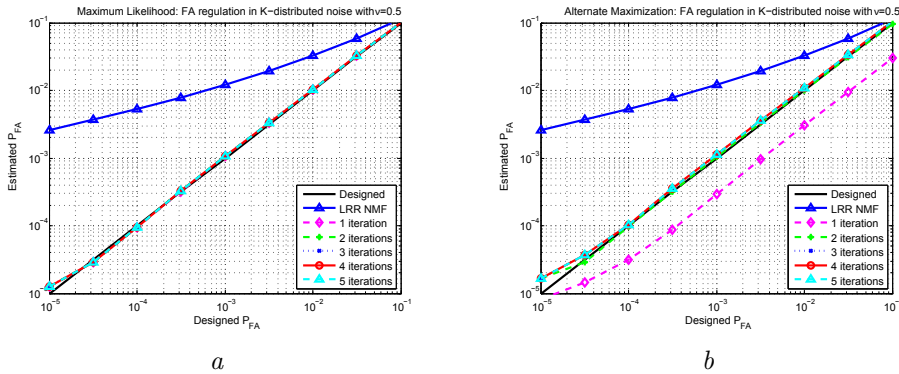Figure 6.4: Convergence of the amplitude estimators (6.13) and (6.19) vs clutter shape

a	b

Figure 6.5: False alarm regulation in K-distributed clutter, $\nu = 0.5$: a - Known distribution of texture, b - Distribution-free test

by numerical evaluation of the widely used criteria:

$$C(i) = \frac{|\hat{\alpha}_{i+1} - \hat{\alpha}_i|}{|\hat{\alpha}_i|}, \tag{6.37}$$

where $\hat{\alpha}_i$ stands for the estimation of α at i-th iteration with the corresponding estimator. The estimation of criteria $C(i)$ is shown in Fig. 6.4 for $\nu = \{0.1, 0.5, 10\}$, averaged over 10^3 trials with different velocities. The convergence is achieved in all the scenarios after about 15 iterations, when the criteria reaches the precision floor. Moreover, the convergence is linear for $\nu \geq 0.5$ and has a plateau region at the first few iterations in case of very spiky clutter. Also, the difference between distribution-free estimator and the one, optimized for the given clutter shape is minor and can be observed only for Gaussian-like clutter ($\nu \geq 10$).

Apart from the amplitude estimation, *a priori* known distribution of texture is in-
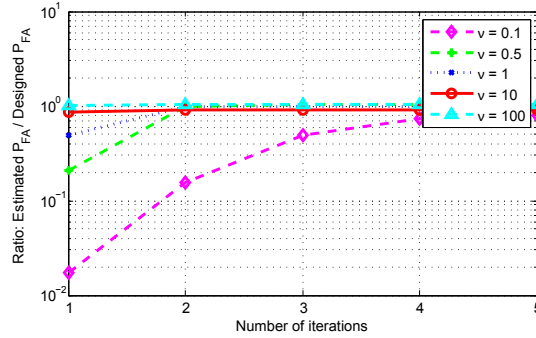
Figure 6.6: False alarm mismatch of the distribution-free test vs iteration number

volved in the detection test via function h_M (6.14). Therefore, it is interesting to study the convergence impact on the decision test directly. That can be done by comparing the false alarm regulation vs iteration of the test (6.14) and the distribution-free test (6.20). The results for $\nu = 0.5$ are shown in Fig. 6.5, with the threshold defined by $T = P_{FA}^{-\frac{M}{M-1}}$. This relation for the threshold is obtained by noticing that the detection test in (6.13), (6.14) for the case of a non-migrating target ($v_0 \approx 0$) can be simplified to the form (6.41) listed below, considering the asymptotic behavior of h_M [96]. For the case of a migrating target, an analytical expression for the probability of a false alarm is not available, however, the relation above fits accurately to the numerical simulations performed, independently on the target velocity. Simulation results, demonstrated in Fig. 6.5, show that the test, relying on the known clutter distribution (6.14) converges to the desired performance already after 1 iteration, while the distribution-free-test (6.20) requires 2 iterations in the studied case. For comparison, P_{FA} regulation of the test:

$$\frac{|\mathbf{a}^H \mathbf{Q}^{-1} \mathbf{y}|^2}{(\mathbf{a}^H \mathbf{Q}^{-1} \mathbf{a})(\mathbf{y}^H \mathbf{Q}^{-1} \mathbf{y})} \underset{H_0}{\overset{H_1}{\gtrless}} T_{\text{LRR-NMF}}. \tag{6.38}$$

is also shown in Fig. 6.5. The latter detector is derived under the locally-Gaussian assumption $\mathbf{Q} = \mathbf{I}_K \otimes \mathbf{S}$ and referred to by LRR NMF (normalized matched filter). Incorrect clutter model results in significant (of a few orders) P_{FA} degradation of the aforementioned detector.

It has been noted that the test with known clutter distribution performs CFAR detection for any values of clutter shape parameter after one iteration. Conversely, the distribution-free test requires different number of iterations to converge, depending on the clutter spikiness, as studies in Fig. 6.6 for $P_{FA} = 10^{-4}$. The plots show that for practical values of clutter shape parameter $\nu = 0.5 \div 10$, two iterations are sufficient
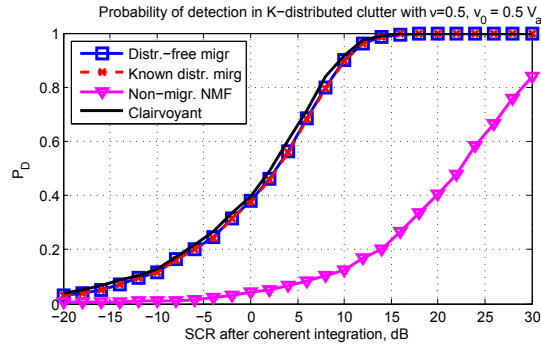
Figure 6.7: Detection probability of a migrating target in K-distributed clutter, $\nu = 0.5$, $v_0 = 7.5 m/s$, $P_{FA} = 10^{-6}$

to get CFAR behavior. In what follows 1 iteration is run for the performance analysis of the test with *a priori* known clutter distributions and 2 iterations are run for the distribution-free test.

In practice, the PDF of clutter is unknown, but it can be estimated from data in homogeneous environment, resulting in a faster convergence of the detector. If a reliable estimation of texture PDF cannot be retrieved from the data due to fast varying radar scene, such as urban environment, distribution-free detector seems more attractive. The distribution-free test also avoids calculation of functions $c_M(x)$ and $h_M(x)$ — the procedure being sometimes hard to implement

Detection performance The other important characteristic of a detector is the detection probability. Two crucial factors influence the detection performance: correct model of clutter and representative model of the target. Incorrect model of clutter results in a detector not satisfying CFAR property, as shown above. On the other hand, target migration is often ignored for detection, resulting in a simple detection rule. For example, detection of non-migrating targets in CG clutter is performed per range cell with the distribution-free test, known as normalized matched filter (NMF) or adaptive cosine estimator (ACE). This test is CFAR test. However, it has significant loss in detection performance, when applied for a migrating target, resulting from the target model mismatch. For example, consider a point target, moving with velocity $v_0 = 0.5 v_a = 7.5 m/s$, which migrates $v_0 M T_r = 0.24 m = 1.6 \delta_R$ during CPI. In Fig. 6.7, the detection performance of NMF applied to one range cell with narrowband target signature (NB NMF) is compared with two proposed techniques (known texture distribution and distribution-free) together with the clairvoyant detector. Clairvoyant detector is implemented as the matched filter detector, applied for the LRRS under test with the correct steering vector of the target and assuming

a priori known clutter CM in the LRRS (6.7). The latter implies predefined values of textures in the K range cells under test and therefore implemented by:

$$\frac{|\mathbf{a}^H\mathbf{M}^{-1}\mathbf{y}|^2}{(\mathbf{a}^H\mathbf{M}^{-1}\mathbf{a})} \overset{H_1}{\underset{H_0}{\gtrless}} T_{\text{clair}}. \tag{6.39}$$

The horizontal axis of Fig. 6.7 corresponds to SCR after coherent integration and whitening:

$$\text{SCR} = \frac{|\alpha|^2}{E\{\tau\}}\mathbf{a}^H\mathbf{Q}^{-1}\mathbf{a}. \tag{6.40}$$

This result clearly shows that not accounting for target migration results in severe loss in the detection performance. This loss increases for fast moving targets proportionally to the smearing of the target response due to migration and diminishes for slow-moving targets. In the limiting case of $v_0 = 0$ the distribution-free test for a migrating target (6.19), (6.20) at the range cell k_0 can be simplified to:

$$\frac{|\mathbf{a}_{\mathbf{k_0}}^H\mathbf{S}^{-1}\mathbf{y}_{\mathbf{k_0}}|^2}{\left(\mathbf{a}_{\mathbf{k_0}}^H\mathbf{S}^{-1}\mathbf{a}_{\mathbf{k_0}}\right)\left(\mathbf{y}_{\mathbf{k_0}}^H\mathbf{S}^{-1}\mathbf{y}_{\mathbf{k_0}}\right)} \overset{H_1}{\underset{H_0}{\gtrless}} T. \tag{6.41}$$

where $\mathbf{a}_{\mathbf{k_0}}$ is $K \times 1$ vector of ones, since no Doppler frequency shift is present for a stationary target. Therefore, the proposed distribution-free test for migrating target degenerated to the NMF, when target migration is negligible. If the test (6.41), considering no migration in the target model, is applied to other velocities with their narrowband signature, it is referred by NB NMF and was mentioned above.

An interesting phenomenon can be observed with a careful analysis of Fig. 6.2. There, a moving target of interest is shown to cross a number of range cells during CPI. The number of these range cells is proportional to the velocity of the target $MT_r v_0/\delta_R$, given the parameters of the radar are fixed. Intuitively, the faster the target, the more it migrates, the lower should be the probability to miss the target due to a possible clutter spike in one range cell, so the higher the probability of detection: target range-walk along non-Gaussian clutter thus can provide a new way to exploit clutter diversity. Such diversity on clutter is intrinsic for a migrating target and makes the detection probability in high resolution clutter velocity-dependent. A numerical study of this phenomenon is demonstrated in Fig. 6.8 for three different shape parameters of K-distribution. Note that by the model definition, the test for a target with $v = 0$ is equivalent to NMF applied for one range cell. In all the cases, the fast moving target is easier to detect than the stationary one: the improvement is significant for very spiky clutter - about 7 dB for $\nu = 0.5$, reasonable for moderately spiky clutter - about 4 dB for $\nu = 1$ and negligible for the Gaussian-like clutter - about 0.5 dB for $\nu = 10$. In the limiting case $\nu \to +\infty$, the clutter is Gaussian and
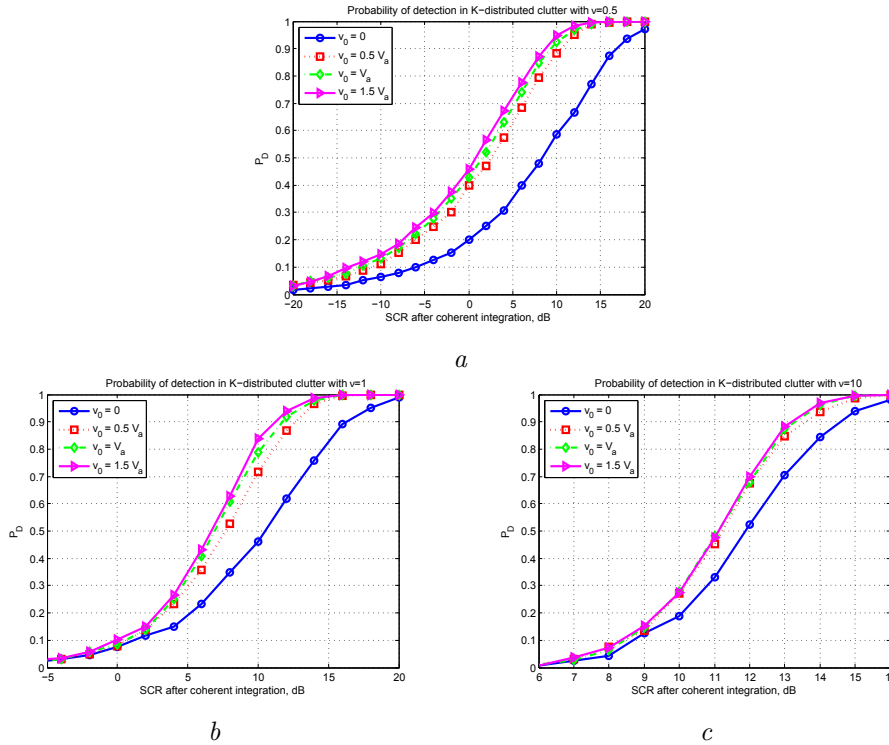
Figure 6.8: Detection probability of a migrating target with the distribution-free test for different velocities of the target, $P_{FA} = 10^{-6}$ and clutter shape parameter a - $\nu = 0.5$; b - $\nu = 1$; c - $\nu = 10$

the detector simplifies to (6.18), which does not depend on target velocity. Also, the detection improvement increases non-linearly with the target range-walk enlargement. The major improvement is observed, when the target migrates at least one range cell. Thus, 5 dB improvement in detection can be observed for $\nu = 0.5$ and 1.6 range cells migration ($v_0 = 0.5v_a$); additional range-walk of 1.6 range cells ($v_0 = v_a$) then brings only in 1 dB additional gain in detection performance; another increase in the target migration by 1.6 range cell ($v_0 = 1.5v_a$ with total migration of 4.8 range cells) then results in less than 1 dB gain. Clearly, the detection improvement gradually saturates with increasing the velocity. For $\nu \geq 1$ the difference between $v_0 = v_a$ and $v_0 = 1.5v_a$ is minor. The phenomenon is akin to range-extended target detection in non-Gaussian clutter, where the detection performance depends on the target extent [11, 12]. The major difference between the two approaches is that for a range migrating target, its signature is summed up coherently along the range walk, while the response of a range extended target is integrated incoherently along its extent.

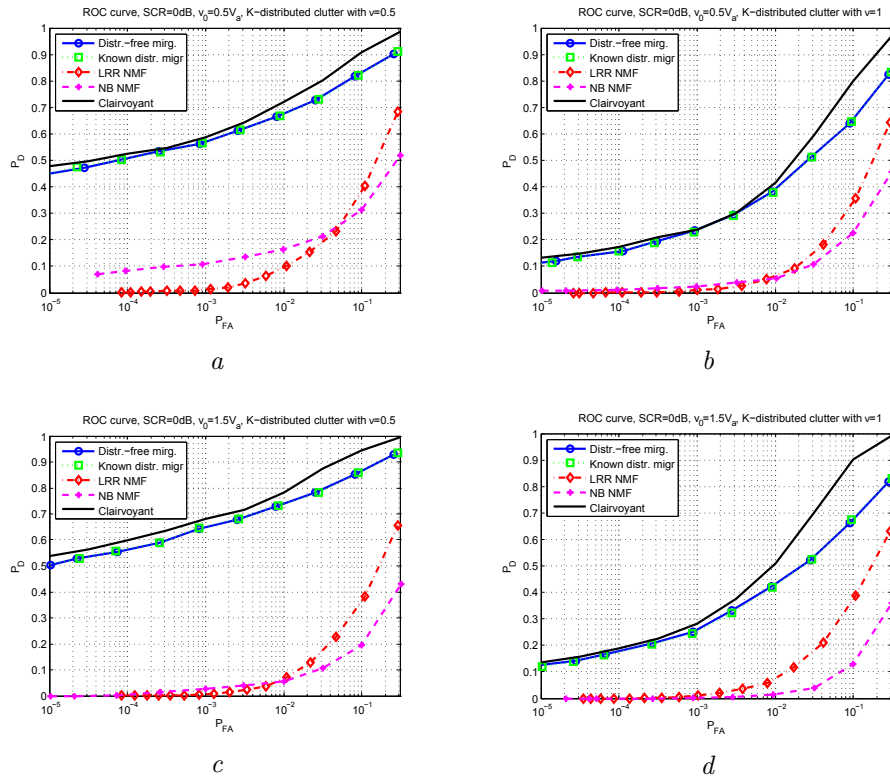To sum up, target range walk provides a novel way to exploit diversity on clutter.

Figure 6.9: ROC curves for a target with $SCR = 0$ dB after coherent integration in K-distributed clutter: a - $v_0 = 0.5v_a, \nu = 0.5$; b - $v_0 = 0.5v_a, \nu = 1$; c - $v_0 = 1.5v_a, \nu = 0.5$; d - $v_0 = 1.5v_a, \nu = 1$

The observed diversity gain is not linear and saturates as the number of the range cells increases: the major improvement is obtained by the first 3 range cells migration, and the effect fully saturates for a range-walk over 5 range cells.

An alternative way to represent the advantages of the proposed detectors over the existing techniques is to evaluate the ROC of them. The scenario for numerical evaluation of the ROC curves is similar to that considered above: a point target with $SCR = 0$ dB after coherent integration moving with velocity $v_0 = 0.5v_a = 7.5$ m/s or $v_0 = 1.5v_a = 22.5$ m/s is considered. The clutter follows K-distribution with shape parameters: $\nu = 0.5$ and $\nu = 1$. The performance comparison is performed for all the detectors mentioned above, namely: detector of migrating target with prior knowledge of texture PDF and distribution-free one, LRR NMF, NB NMF and the clairvoyant detector. Simulation results are shown in Fig. 6.9, each plot corresponds to a specific combination of ν and v_0. The results show significant improvement of the proposed techniques with respect to the conventional detectors (LRR NMF and NB NMF).
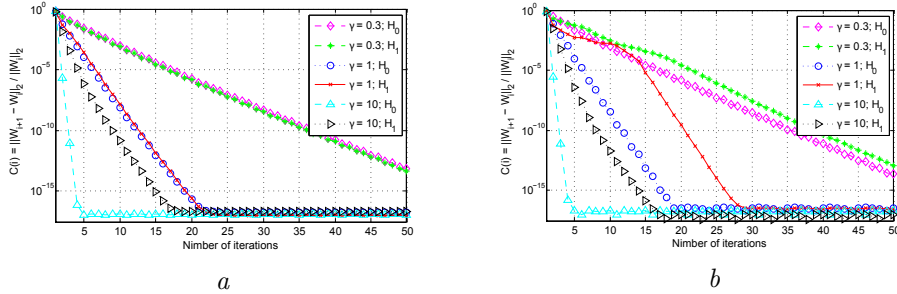
Figure 6.10: Convergence of DIM estimator (6.25) in K-distributed clutter: a - $\nu = 0.5$, b - $\nu = 0.1$

Note the different nature of performance degradation of these algorithms: LRR NMF suffers from the incorrect model of clutter and therefore loses CFAR property; on the other hand, NB NMF keeps CFAR property, but brings significant loss in detection because of target signature mismatch. The loss of the proposed algorithms compared to the clairvoyant detector is negligible. The comparison of the plots with equal clutter shape parameter allows to see the benefits of a fast moving target detection over slow one in spiky clutter, already mentioned above.

6.7.2 Detector for dependent interference model

Convergence analysis and false alarm regulation The convergence of the estimator (6.25) is analyzed by numerically evaluating the widely used criterion:

$$C(i) = \frac{||\hat{\mathbf{W}}_{i+1}^{(H)} - \hat{\mathbf{W}}_i^{(H)}||_2}{||\hat{\mathbf{W}}_i^{(h)}||_2}, \tag{6.42}$$

where $\hat{\mathbf{W}}_i^{(H)}$ stands for the matrix $\mathbf{W} = \mathrm{diag}\,(\sigma_0, \ldots, \sigma_{K-1}) \otimes \mathbf{I}_M$ built of the estimations $\hat{\sigma}_{\mathcal{K}}$ at i-th iteration under hypothesis H. In this simulation, uncorrelated over slow time clutter component is considered $\mathbf{S} = \mathbf{I}_M$; the range correlation is defined by the vector $\mathbf{d}_k = \exp(-\gamma k)$, which is the first column of symmetrical Toeplitz matrix $\mathbf{D}$. The case of $\gamma \to \infty$ corresponds to IIM; and $\gamma \to 0$ corresponds to completely correlated over range speckle.

Fig. 6.10 shows the convergence of the estimator (6.24) (averaged over 10^2 Monte-Carlo runs for 320 range-velocity cells each) under both hypotheses for the case of range-correlated speckle: $\gamma = 0.3$ and $\gamma = 1$; and uncorrelated over range speckle: $\gamma = 10$ (the correlation intervals $\tau_{cor} = \gamma^{-1}$ for the three scenarios are $\tau_{cor} = \{3.3; 1, 0.1\}$ range cells accordingly). Note that in most of the cases the estimator converges linearly to the precision floor, except of the very spiky clutter $\nu = 0.1$ under the hypothesis of target presence (H_1). The estimator converges more rapidly
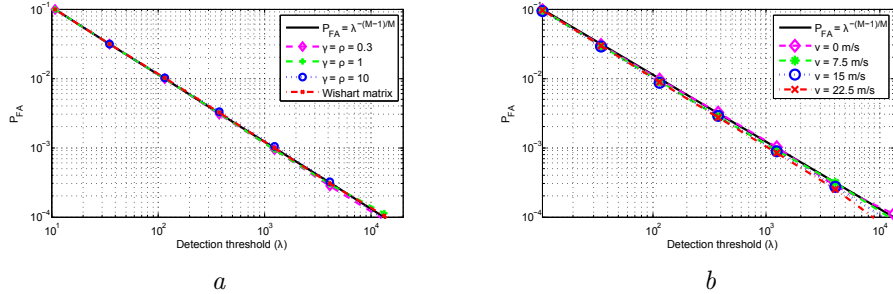
$$a \qquad\qquad\qquad\qquad b$$

Figure 6.11: False alarm regulation: a - vs speckle covariance matrix; b - vs target velocity.

in case of weakly correlated in range clutter; for negligible clutter spatial correlation, the convergence under H_0 is much faster than under H_1. The shape of clutter distribution affects the convergence only for very spiky clutter, K-distribution clutter with shape parameters between 0.5 and $+\infty$ has similar convergence rate (Fig. 6.10, a). Clutter slow-time correlation properties and target velocity have minor effect on the convergence.

To prove the CFAR-ness of the DIM detector, its ability to preserve constant P_{FA} for different target and clutter parameters is studied. The parameters of interest are the speckle CM $\mathbf{Q}$, clutter texture $\sigma_{\mathcal{K}}$ and the target velocity. The number of iterations is set to 20 to reach the convergence point for all the scenarios with $\gamma \geq 1$ and $\nu \geq 0.5$.

First, the CFAR behavior with respect to the speckle CM $\mathbf{Q}$ and the clutter texture is studied. The clutter with spatial (range) and temporal (slow-time) correlation is considered. The slow-time CM $\mathbf{S}$ is a symmetrical Toeplitz matrix defined by its first column $\mathbf{s}_m = \exp(-\rho m)$; the range CM $\mathbf{D}$ follows the above definition. For comparison, a random complex Wishart distributed matrix $\mathbf{Q} \sim \mathcal{CW}_{KM}(\mathbf{I}_{KM}, 2KM)$ is also examined. The texture components $\sigma_{\mathcal{K}}^2$ follows Gamma distribution with the shape parameter $\nu = 0.5$ and the scale parameter $\mu = 1$. The simulations results presented in Fig. 6.11 (a) show that the proposed detector ensures CFAR behavior w.r.t. the speckle CM and the clutter texture. The detection threshold is well approximated by $T = P_{FA}^{-\frac{M}{M-1}}$. This coincides with IIM detector.

Similarly, Fig. 6.11 (b) shows that the proposed detector ensures CFAR behavior with respect to the target velocity. In this simulation only spatially correlated clutter with $\gamma = 1$ and $\rho \to +\infty$ was considered. This shows that the proposed detector ensures CFAR-ness w.r.t. the speckle CM, the clutter texture, and the target velocity.

Detection performance The analysis of the detection performance as a function of target SCR (6.40) is shown in Fig. 6.12 for target velocities $v_0 = 0$ m/s and $v_0 =$
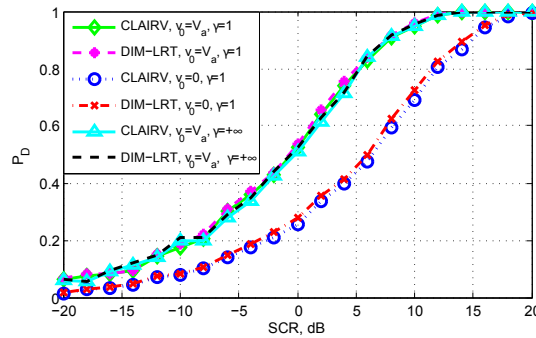
Figure 6.12: Detection probability of range migrating target in CG clutter with: $v = 0$ m/s and $v = 15$ m/s
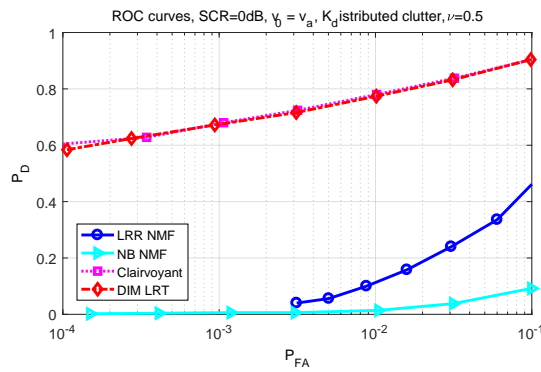

Figure 6.13: ROC curves of migrating target detector in CG clutter

$v_a = 15$ m/s and different clutter spatial correlation: $\gamma = 1$ and $\gamma \to +\infty$; $\mathbf{S} = \mathbf{I}_M$, $P_{FA} = 10^{-4}$. Comparison in Fig. 6.12 includes the proposed detector, referred hereinafter by DIM-LRT, and the clairvoyant detector, which assumes $\sigma_\mathcal{K}$ and so $\mathbf{M}$ are known *a priori*, and therefore it is a matched filter detector [49]. The loss of the proposed detector in comparison to the clairvoyant one is about 1 dB in each scenario.

The analysis shows that detection performance depends on the target velocity, similarly to the case of spatially uncorrelated clutter. The detection performance, as a function of SCR does not depend on clutter spatial correlation. That statement should be kept loose, since the SCR itself depends on both spatial and temporal correlation of clutter.

To conclude the analysis of a point target detection with a range-walk in spiky clutter with known speckle CM, the performance is studied in terms of ROC curves.

Table 6.1: Extended target models with $\Delta_R/\delta_R = 4$: discrete scatterers locations and percentage of the total energy

Model number	Cell number			
	1	2	3	4
1	1/4	1/4	1/4	1/4
2	1/2	1/4	1/4	0
3	3/4	1/4	0	0
4	1	0	0	0

The four detectors are examined, namely: LRR NMF - Normalized matched filter applied to a LRRS, which consider a locally Gaussian clutter model; NB NMF - Normalized matched filter applied per range cell, modeling no target migration occur during CPI; the proposed detector, referred to as DIM-LRT, and the clairvoyant detector described above. Simulation results in Fig. 6.13 show the advantages of applying CFAR detector for range migrating targets, similar to the case of IIM.

6.7.3 Extended target detector

Herein the performance of the proposed detector for range-extended migrating targets is analyzed. A target of interest with known extent $\Delta_R/\delta_R = 4$ is modeled by the discrete scatterer model with different spatial distribution [12], given in Table 6.1. For this scenario it is assumed that $|v_0| \leq v_a$, so $K = 8$ is selected in order to satisfy (2.14). Since the analytical expression of the P_{FA} is not available, the threshold providing $P_{FA} = 10^{-4}$ for $\Delta_R/\delta_R = 4$ is estimated via Monte-Carlo routine. This threshold is then used to evaluate numerically the detection performance for the target models given in Table 6.1. Range correlated clutter with: $\gamma = 1$ and $\rho \rightarrow +\infty$ is considered. The detection performance is evaluated for target velocities $v_0 = 0$ and $v_0 = v_a = 15$ m/s. Target SCR is defined as SCR $= \frac{\mathcal{E}}{E\{\tau\}} \mathbf{a}^H \mathbf{Q}^{-1} \mathbf{a}$, where $\mathcal{E} = \sum_{i=r}^{4} w_r |\alpha_r|^2$ and w_r are the weighting coefficients, given in Table 6.1.

The simulation results in Fig. 6.14, a show that non-coherent averaging along target extent allows detection improvement for a stationary target, which is a well-known phenomenon. The detection gain is less than that shown in [12] due to range-correlated clutter and different parameters of the waveform. The detection performance of a migrating extended target, on the other hand, is almost independent of the target extent, as shown in Fig. 6.14, b. That is due to the fact that averaging over the target and over clutter provides the same gain - due to diversity. That is why, being merged together, additional averaging only leads to saturation of the diversity effect, but not to additional gain. The correct interpretation of Fig. 6.14, b is the following: for a target, migrating sufficiently enough to exploit clutter diversity along
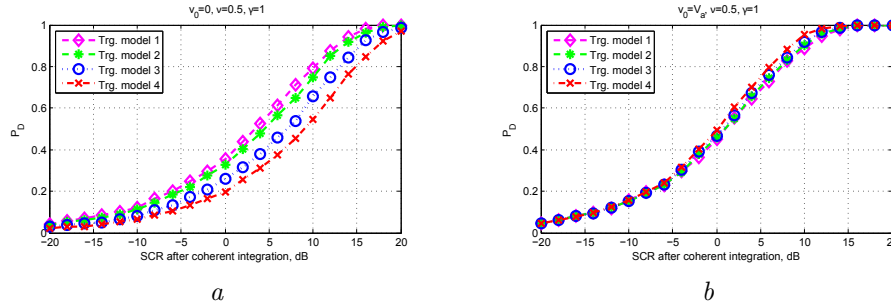
Figure 6.14: Detection performance for the extended target: a - stationary target: $v_0 = 0$ m/s; b - migrating target: $v_0 = 15$ m/s.

the range-walk, the detection performance depends only on the SCR of the extended target, defined above, but not on the shape of target power distribution over range.

With that result, the conclusion given in [6] can be extended: *to improve detection performance, radar range resolution should be selected such, that the target of interest is spread over 5-10 range cells as a result of its range extent and its range migration. So meter resolution should be enough for detection of typical air and ground targets.*

6.7.4   Adaptive detector of a point target

False alarm regulation   The adaptive detector should preserve the CFAR property w.r.t. $\mathbf{Q}, \sigma_{\mathcal{K}}$ and the target velocity. The aim of this subsection is to clarify the reason to use the DIM for deriving the adaptive detector instead of IIM. This is done by comparison of the P_{FA} regulation for two adaptive detectors, derived under the models, referred above. For the IIM detector, a single range cell SCM is estimated and the CM of the LRRS then has the block diagonal structure (6.28). In Fig. 6.15 the false alarm dependency on the (expected) target velocity is studied for two adaptive detectors. First, the DIM detector with the SCM from $L = 2KM$ reference LRRSs is analyzed and, second, the IIM detector with the diagonal blocks estimated from $L = 2M$ reference cells is considered. The results presented in Fig. 6.15 show that for the limited number of reference cells IIM does not hold the CFAR property w.r.t. the target velocity, while DIM detector does. This phenomenon has simple explanation: the signature of the migrating target has strong auto-correlation over range. The IIM detector over-amplify these components, as it assumes there is no clutter cross-correlation in adjacent range cells. On the other hand, for any real clutter and finite number of reference cells, some cross-correlation is present, and recognized by the IIM detector as a target component, which leads to the variation of the P_{FA} with target velocity.
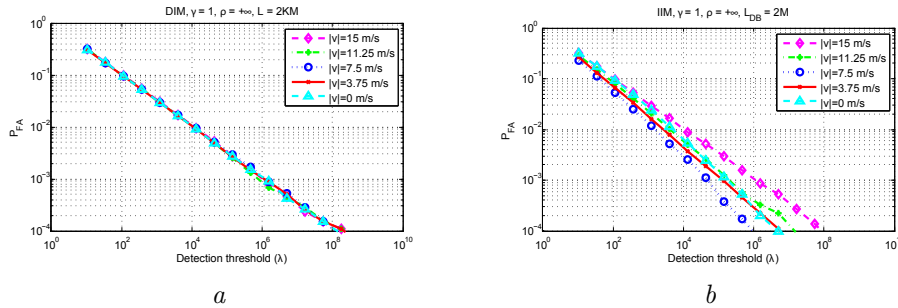
Figure 6.15: False alarm regulation of two adaptive detectors in spatially-correlated K-distributed clutter, $\nu = 0.5$, $\gamma = +1$, $\rho = +\infty$: a - Detector for the DIM; b - Detector for the IIM.
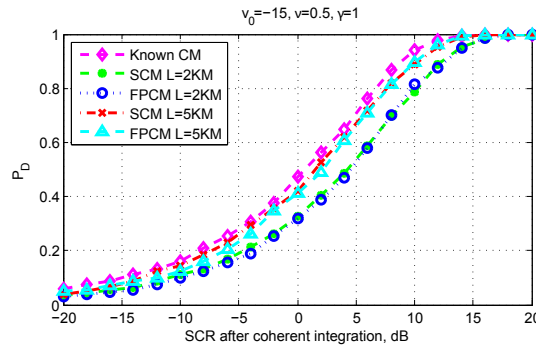

Figure 6.16: Detection probability of the adaptive detector for the range migrating target in CG clutter with $v = 15$ m/s

Detection performance The detection performance of the adaptive detector is analyzed in two scenarios: in the first case, the reference data contains only the speckle clutter component, so the MLE of CM is obtained with the SCM from this reference data (6.36). In the second case, the reference data follows the CG model, and the proposed in Algorithm 1 CM estimator, referred to as FPCM, is employed. There are $L = 2KM$ and $L = 5KM$ reference cells considered and 10^6 Monte-Carlo trials are performed in order to set the threshold satisfying $P_{FA} = 10^{-4}$ in each case. For the FPCM estimation the number of iterations is fixed to $I_\sigma = 5$ and $I_Q = 20$. Simulations results for the target moving with velocity $v_0 = 15$ m/s in range correlated clutter with $\gamma = 1$ are shown in Fig. 6.16. The detection loss for the case of $L = 2KM$ is about 3.5 dB and 4 dB for the SCM of the speckle and the proposed estimation of the CM accordingly; and about 0.9 and 1.5 dB for the case of the $L = 5KM$. Both cases agree well (within 1 dB) with the theoretical performance degradation of the adaptive detectors in a single range cell [79, 93].

6.8   Conclusion

In this chapter, a novel detector for range migrating targets in non-Gaussian clutter has been proposed and analyzed. As radar clutter, being observed by a high-resolution radar, does not follow Gaussian distribution anymore, the CG model has been considered, which allows modeling of clutter power variation along range. The detector for a range migrating target in CG clutter is then introduced showing superior performance (e.g., in the considered example the proposed detector outperformed the traditional one by 20 dB for target with 1.6 range cells migration during CPI) over the conventional detectors in non-Gaussian clutter. It is shown that target range walk is beneficial for detection, as it brings additional diversity on clutter, alike incoherent integration along the target extent. Therefore, fast moving targets are easier to detect with a high resolution radar, than slow targets with the same SCR. Performance assessment of the proposed detector shows that a few range cells migration during the coherent burst provides a few dB detection gain, depending on clutter spikiness. The diversity of clutter accumulates with the non-coherent integration of the target response along its extent. The best detection performance is achieved when the target is spread over 5-10 range cells as a result of its range extent and its range migration. So meter resolution is sufficient for detection of typical air and ground targets.

Chapter 7

Conclusion and future work

Modern surveillance radars are designed to detect moving targets of interest in a adverse environment, which can encompass strong unwanted reflections from ground or sea surface, clouds, precipitation, etc. Detection of weak and small moving targets in environmental clutter remains a challenging task for the existing radar systems. To address this challenge, future radars should adopt new waveforms and novel signal processing techniques for improved target discrimination from clutter.

One way to improve radar performance in a heavy environmental clutter is to exploit wideband high-resolution waveforms. A fine range resolution of such waveforms can improve visibility of small targets by decreasing the clutter level per range cell, reduces the effect of a multi-path and provides target classification capability by exploiting their high-resolution range profiles. Moreover, the detailed measurement of the target range provides an alternative solution for range-Doppler ambiguities and target fading, obtained with a single low-PRF burst of high-resolution pulses: such waveform allows resolving ambiguities by measuring target range displacement within the CPI and delivers multiple range samples along the target physical extent, which can be used to alleviate the target fading effect.

In this thesis, the feasibility of using a single burst of high-resolution pulses as a sounding signal in surveillance radars is investigated. The appropriate models of a moving target and clutter are provided for the high-resolution mode of the radar. The special processing for target detection in difficult scenarios, when either multiple targets are present in the vicinity of each other, or the scene is corrupted with heavy clutter, has been proposed. The performed research provides some basic insight for implementation of new radar architectures with the utilization of wideband waveforms.

7.1   Results and novelties

The research performed has led to the following novel results:

- *The unambiguous measurement of target range and velocity can be obtained in one burst if its time-bandwidth product is large enough.* It is demonstrated that in the noise-limited scenario radar scene can be reconstructed from a single-low PRF measurement with no velocity ambiguities. The ambiguous residuals of the targets present in the scene, called ambiguous sidelobes, can be efficiently suppressed with modern non-parametric high-resolution spectrum estimators. IAA (Iterative Adaptive Approach) and SPICE (Semi-Parametric Iterative Covariance-based Estimator) are proposed for unambiguous scene reconstruction. These estimators outperform the existing non-parametric estimators in typical scenarios. The performance of scene reconstruction is limited in presence of diffuse clutter, whose ambiguities cannot be completely suppressed with the proposed approach.

- *A dedicated detector has been proposed for detection of multiple closely spaced targets in the scene and its properties have been studied.* The problem of multiple targets detection in the observed low range resolution segment has been investigated. It has been demonstrated that conventional matched filter detector will suffer from multiple false detections at the ambiguous sidelobes of the real targets, while the pick-the-peak detector is not designed for detection of more than one target in the data set. A novel detector has been proposed, which uses RELAX spectrum estimator, and allows detecting multiple targets in the observed scene. It is implemented as a simple post-processing of the output of a conventional matched-filter detector and ensures bounded false alarm property.

- *A waveform with maximum coherent bandwidth should be employed for better clutter suppression.* The presented results demonstrated that the ability of a wideband radar to detect a target in the ambiguous response of diffuse ground clutter strongly depends on the clutter spectral characteristics, the radial velocity of the target and the coherently processed bandwidth. The performance of clutter suppression using target migration is highly efficient against clutter with a narrow Doppler spectrum, but it has limited improvement against clutter with wide Doppler spectrum. The most difficult regions to detect a target is the first ambiguity of clutter. The fast targets are easier to detect due to widening of their Doppler spectrum. To improve the performance of a wideband coherent radar against clutter, the waveform with the maximum available bandwidth should be employed.

- *Performance comparison of the proposed waveform with the conventional multi-burst one has been carried out.* The detailed analysis, carried out in Chapter 3, demonstrated that wideband waveform and associated signal processing is preferable in scenarios, when clutter level is low or it has narrow Doppler spectrum. In the scenarios with wide Doppler spectrum of clutter the conventional multi-burst waveform provides better performance.

- *An optimal detector of range-migrating targets, which performs two-dimensional clutter filtering: in Doppler frequency and in range, is proposed and its performance is evaluated.* In the high-resolution mode of the radar, the observed ground clutter can have large and rapid variation of power in range, well described by the compound-Gaussian model. A novel detector of range-migrating targets in non-homogeneous clutter has been proposed, which accounts for clutter power variation in range and clutter Doppler spectrum simultaneously. The added feature of the proposed detector to adapt to clutter variation in range allows exploiting clutter diversity in range, beneficial for detection of weak targets in spiky clutter. This gained diversity on clutter depends on the target velocity and makes the detection probability in spiky clutter velocity dependent: fast moving targets are easier to detect with a high-resolution radar than slow targets with the same SCR.

- *Diversity on target provide the same benefits as diversity on clutter.* Target diversity, obtained for an extended target by integration the response along its range extent can be alternatively achieved by integrating the response of a point-like target, migrating the same number of range cells in presence of non-Gaussian clutter. The radar range resolution should be selected such, that the target of interest, is spread over 5-10 range cells as a result of its range extent and its range migration. So meter resolution of the surveillance radar is sufficient for detection of typical air targets with a spatial diversity in one burst.

7.2   Recommendations for future research

- *Extension of wideband signal processing to multi-band signals.* One limitation of using wideband signals for surveillance comes from the wide frequency occupancy of such signals and, as a result, of higher chance to have an interfering signal in some part of the spectrum. The methods for estimating the interfering signal and adaptive filtering of the corrupted frequency band should be considered. The observed useful signal in multiple frequency sub-bands should be merged together to recover the high range resolution. The impact of such filtering on the unambiguous processing (distortion of the main lobe, increase

of the sidelobe level) has to be investigated.

- *Adaptive estimation of the target range extent from the measurements, combination of target detector with an extended object tracking.* The existing detectors of range extended targets relies on *a priori* knowledge of the target sizes. In practice, this information is unknown and therefore should be tuned by the operator. The methods for simultaneous estimation of a target extent and its detection from clutter are strongly required element for a fully adaptive radar detector. The estimation of the target extent is also required for accurate target tracking. So, merging of this information, extracted at detection and at tracking stages, can improve both the detection probability and the tracking accuracy.

- *Development of high-resolution polarimetric clutter maps and clutter map detectors for range-migrating targets.* The migrating target detector, proposed in Chapter 6, can be adapted to the high-resolution clutter maps, which describe the expected power of clutter in every observed range-angular cell, possibly for every polarization. The information, contained in such clutter maps can be used on its own for non-iterative estimation of the target amplitude or provide an initial guess for the iterative solution. Moreover, the obtained clutter map can demonstrate the areas over which the application of the proposed detector is beneficial, and those, where clutter can be assumed Gaussian and the matched filter detector will provide equal performance.

- *Experimental validation in other frequency bands* The results, presented in the thesis, should be validated on real data sets from different sensors, operating at different frequency bands (L, X, Ku, K, Ka).

- *Improved measurement of the target angle by exploiting its range extension.* Multiple range samples with the target and clutter diversity can be fused together to improve the accuracy of the target angular measurement. Alternatively, these responses can be processed jointly to discriminate between the presence of a single target in the beam and the scenario with multiple targets in the vicinity of each other. Both problems can be tackled assuming an extended target response in one high-resolution burst is available.

- *Efficient implementation.* Computational load of the proposed techniques has to be evaluated and their efficient implementation should be studies.

Appendices
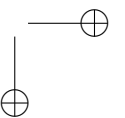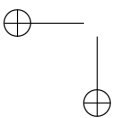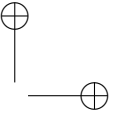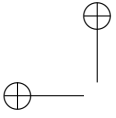
Appendix A

Description of radar equipment

The applicability of the proposed wideband signal processing is tested with the polarimetric agile radar (PARSAX), available at TU Delft [97].

A.1 PARSAX radar

PARSAX is a software defined radar with digital waveform generator of agile waveforms and programmable digital receiver, operating in S band [97, 98]. The main characteristics of the radar are summarized in Table A.1[1] and the antenna system of PARSAX is demonstrated in Fig. A.1. PARSAX is located on the rooftop of the EEMCS (EWI) building at TU-Delft, at a height of about 100 m.

Detailed measurements of the PARSAX radar demonstrated its possibility to operate with the bandwidth up to 100 MHz [99]. The frequency response of the whole PARSAX system at the intermediate frequency (IF) is demonstrated in Fig. A.2 [99]. Therefore, PARSAX provides nearly wideband ($B = 100$ MHz, $B/f_c \approx 3\%$) mode with the range resolution of 1.5 m.

A.2 Deramping processing of LFM signal

In its standard operational mode, PARSAX transmits bursts of linear frequency modulated (LFM) sweeps, also called chirps, and performed range compression via deramping processing.

---

[1]In the target model the lower frequency of the band f_c is considered. Thus, in its wideband mode ($B = 100$ MHz) PARSAX has $f_c = 3.265$ GHz.

Figure A.1: PARSAX antenna system
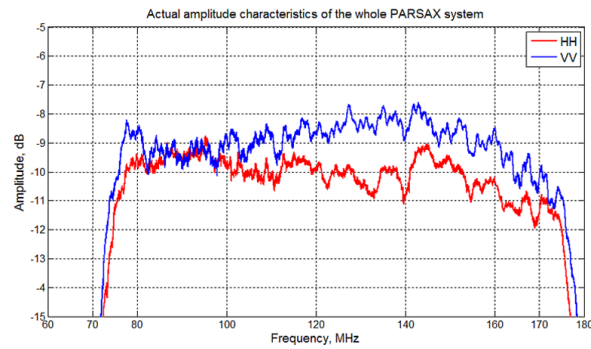
Figure A.2: Amplitude characteristic of the whole PARSAX system at intermediate frequency, from [99]

A LFM signal is characterized by its instantaneous frequency:

$$f(t) = f_c + \frac{B}{T_s}t = f_c + \beta t, \quad t \in [0, T_s], \tag{A.1}$$

where β defines the sweep rate and T_s is the sweep time. Accordingly, a transmitted sweep can be written as:

$$s_{\text{tx}}(t) = \exp\left(f_c t + \frac{\beta t^2}{2}\right). \tag{A.2}$$

The transmitted signal reflects from the target and arrives back to the radar as a

Table A.1: Parameters of PARSAX radar

Spectrum	Central frequency: 3.315 GHz;
	Modulation bandwidth: 2 - 100 MHz;
	Resolution: 75 - 1.5 m.
Antennas	Two parabolic reflectors:
	Rx: diameter=2.12 m, beam width=4.6 deg, gain=32.8 dB;
	Tx: diameter=4.28 m, beam width=1.8 deg, gain=40.0 dB;
	Isolation receiver-transmitter: HH=-100 dB, VV=-85 dB.
Transmitter	Solid state power amplifiers;
	100 Watt max per channel;
	80 dB attenuators (8 bits control bus).
Reciver	Dynamic range: better 70 dB (SFDR);
	Noise floor: approx. -93 dBm
	ADC at IF (125 MHz, sampling 400 MHz, 14 bits);
	4 channels FPGA-based digital processor.
Waveforms	Four channel arbitrary waveform generator
	(sampling up to 1.2 GHz, 16 bits);
	Sounding signals with BT-product up to 100.000 in real time;
	Standard mode: LFM with deramping processing.

delayed by $\tau(t)$ and attenuated copy of the transmitted wavefrom:

$$s_{\mathrm{rx}}(t) = \alpha \exp\left(f_c(t - \tau(t)) + \frac{\beta(t - \tau(t))^2}{2} \right). \tag{A.3}$$

The deramping, also called stretched processing, is implemented by mixing the received signal with the replica of the transmitted waveform and filtering out high-frequency component[1], schematically demonstrated in Fig. A.3. The obtained signal is called beat signal and it is given by:

$$s_{\mathrm{b}}(t) = \alpha \exp\left(\beta\tau(t)t + f_c t - \frac{\beta\tau(t)^2}{2} \right). \tag{A.4}$$

Assuming a constant radial motion of the target $\tau(t) = \tau_0 - \frac{2v_0}{c}t$ with $v_0 \ll c$, the mixed signal can be written as:

$$s_{\mathrm{b}}(t) \approx \alpha \exp\left((\beta\tau_0 + f_D)\, t \right) = \alpha \exp\left(f_b t \right), \tag{A.5}$$

---

[1]In the PARSAX radar, a superheterodyne receiver is employed, which mixes the signals at the intermediate frequency (IF). For simplicity this step is skipped with no effect on the final result.
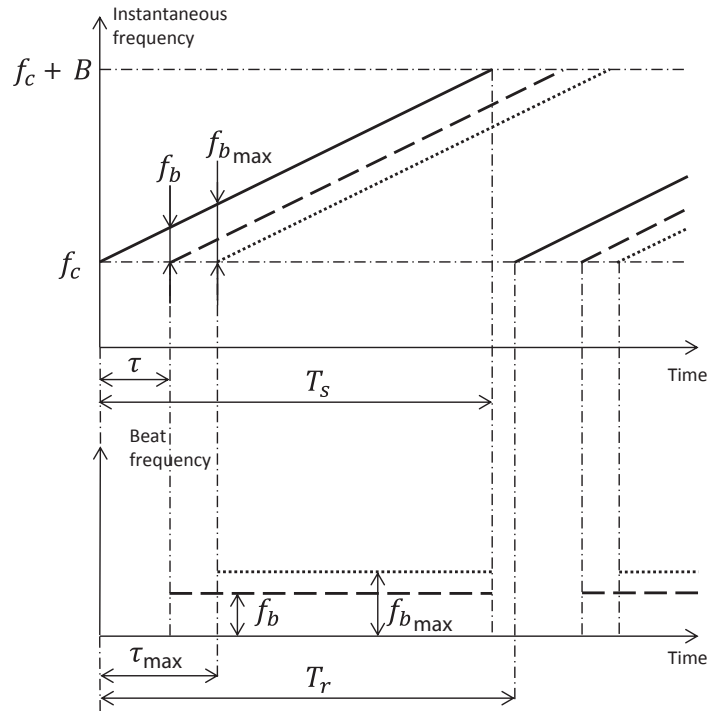
Figure A.3: Deramping processing of LFM waveform

where f_b is the beat frequency and $f_D = f_c \frac{2v_0}{c}$ is the Doppler frequency, originated from the target motion. Moreover, with the wideband waveform the approximation:

$$f_b = \beta\tau_0 + f_D \approx \beta\tau_0 \tag{A.6}$$

holds for the typical target velocities [53]. Range compression of the LFM waveform is therefore obtained as the FFT of the beat signal. To minimize the effect of the range sidelobes, Hamming window is applied in the standard mode, hence selection of other window is possible.

The maximum range, available with the deramping processing, is limited by the sampling frequency of beat signal f_{sb}:

$$R_{\max} = \frac{c\tau_{\max}}{2} = \frac{c}{2\beta}f_{b\max} = \frac{c}{2\beta}\frac{f_{sb}}{2}. \tag{A.7}$$

The range resolution is proportional to the frequency resolution of the beat signal. To preserve equal coherent gain for all targets at ranges up to $R_{\max}$, the beat fre-

A.2 Deramping processing of LFM signal   139

quency is estimated in the time interval $[\tau_{\max}, T_s]$, $\tau_{\max} = 2R_{\max}/c$, providing range resolution:

$$\delta_R = \frac{c}{2B} \frac{T_s - \tau_{\max}}{T_s}. \tag{A.8}$$

Note that every transmitted sweep is followed by small pause (20 μs) to minimize the transition process due to instantaneous frequency change by B.

In the wideband setting, PARSAX has the following parameters: $B = 100$ MHz, $T_s = 1$ ms, $T_r = 1.02$ ms, $f_s = 400/22 \approx 18.2$ MHz. According to the sampling criteria (A.7), the maximum range can be $R_{\max} = 13.6$ km. However, the radar provides only $N_s = 5100$ range samples per sweep, which represents with the nominal range resolution $R_{\max} = cN_s/(2B) = 7650$ m and gives $\tau_{\max} = 51$ μs. Substitution of $\tau_{\max}$ into (A.8) gives the range resolution of $\delta_R \approx 1.58$ m and, equivalently, the coherently processed bandwidth is $B \approx 95$ MHz.
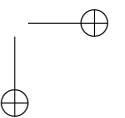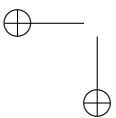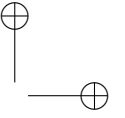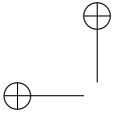
Appendix B

Wideband target signature

B.1 Target signature in fast-frequency/slow-time

From (2.8) and (2.9) if follows that the range compressed signal can be represented in fast-frequency /slow-time domain as:

$$s_{\text{ff,st}}(f,m) = \alpha S\left(f - f_c \frac{2v_0}{c}\right) S^*(f) e^{j2\pi f_c \frac{2v_0}{c} mT_r} e^{-j2\pi f\left(\tau_0 - \frac{2v_0}{c} mT_r\right)}. \tag{B.1}$$

The assumption of the Doppler tolerant pulses in the transmitted burst (2.11) is equivalent to considering $S(f - f_D) \approx S(f)$, which gives:

$$s_{\text{ff,st}}(f,m) = \alpha \left|S(f)\right|^2 e^{j2\pi f_c \frac{2v_0}{c} mT_r} e^{-j2\pi f\tau_0} e^{j2\pi f \frac{2v_0}{c} mT_r}. \tag{B.2}$$

Focusing on the LRRS of the range cells $k' = k_{\text{beg}}, \ldots, k_{\text{beg}} + K - 1$ is equivalent to shifting the range frequency of the signal by $e^{-j2\pi f k_{\text{beg}}/B}$ followed by its sampling in the frequency domain at the rate $\delta_f = c/(2K\delta_R) = B/K$. Then, the fast-frequency / slow-time representation of the LRRS with the target is:

$$T_{\text{ff,st}}(l,m) = \alpha \left|S\left(\frac{B}{K}l\right)\right|^2 e^{j2\pi f_D T_r m} e^{-j2\pi \frac{k_0}{K} l} e^{j2\pi \frac{v_0 T_r}{\delta_R K} lm}, \tag{B.3}$$

where $l = 0, \ldots, K - 1$ is the fast-frequency index.

Assuming a flat spectrum of the transmitted waveform over the frequency band (2.15) and normalization $u_{\text{p}}(0) = 1$, the target signature in the fast-frequency / slow-time domain becomes:

$$T_{\text{ff,st}}(l,m) = \frac{1}{K} e^{j2\pi f_D T_r m} e^{-j2\pi \frac{k_0}{K} l} e^{j2\pi \frac{v_0 T_r}{\delta_R K} lm}. \tag{B.4}$$

B.2   Target signature in fast-frequency/ slow-frequency

Given the target response (B.2) the fast-frequency/slow-frequency representation is obtained by applying DFT over the slow-time dimension:

$$s_{\text{ff,sf}}(f, f_d) = \sum_{m=0}^{M-1} s_{\text{ff,st}}(f, m) e^{-j2\pi f_d T_r m}$$

$$= \alpha \left| S(f) \right|^2 e^{-j2\pi f \tau_0} \sum_{m=0}^{M-1} e^{-j2\pi \left(f_d - f_D \left(1 + \frac{f}{f_c} \right) \right) T_r m} \tag{B.5}$$

where $f_D = f_c \frac{2v_0}{c}$.

Performing DFT over slow-time gives:

$$\sum_{m=0}^{M-1} e^{-j2\pi \left(f_d - f_D \left(1 + \frac{f}{f_c} \right) \right) T_r m} = \frac{1 - e^{-j2\pi \left(f_d - f_D \left(1 + \frac{f}{f_c} \right) \right) T_r M}}{1 - e^{-j2\pi \left(f_d - f_D \left(1 + \frac{f}{f_c} \right) \right) T_r}}$$

$$= \frac{e^{-j2\pi \left(f_d - f_D \left(1 + \frac{f}{f_c} \right) \right) \frac{M T_r}{2}}}{e^{-j2\pi \left(f_d - f_D \left(1 + \frac{f}{f_c} \right) \right) \frac{T_r}{2}}} \cdot \frac{\sin \left(2\pi \left(f_d - f_D \left(1 + \frac{f}{f_c} \right) \right) \frac{M T_r}{2} \right)}{\sin \left(2\pi \left(f_d - f_D \left(1 + \frac{f}{f_c} \right) \right) \frac{T_r}{2} \right)} \tag{B.6}$$

$$\approx M e^{-j2\pi \left(f_d - f_D \left(1 + \frac{f}{f_c} \right) \right) \frac{M-1}{2} T_r} \cdot \text{sinc} \left(\left(f_d - f_D \left(1 + \frac{f}{f_c} \right) \right) M T_r \right),$$

where the approximation $\frac{\sin(M\pi x)}{\sin(\pi x)} \approx M \frac{\sin(M\pi x)}{M\pi x} = M\text{sinc}(Mx)$ has been used assuming that f_d is unfolded Doppler frequency. Substitution (B.6) into (B.5) results in:

$$s_{\text{ff,sf}}(f, f_d) = \alpha M \left| S(f) \right|^2 e^{-j2\pi f \tau_0} e^{-j2\pi \left(f_d - f_D \left(1 + \frac{f}{f_c} \right) \right) \frac{M-1}{2} T_r}$$

$$\cdot \text{sinc} \left(\left(f_d - f_D \left(1 + \frac{f}{f_c} \right) \right) M T_r \right). \tag{B.7}$$

Assuming a flat spectrum of the transmitted pulse and sampling it in the fast-frequency domain similarly to (B.2) and considering normalization $u_{\text{p}}(0) = 1$ gives:

$$T_{\text{ff,sf}}(l, f_d) = \frac{M}{K} e^{-j2\pi \frac{k_0}{K} l} e^{-j2\pi \left(f_d - f_D \left(1 + \frac{B}{K f_c} l \right) \right) \frac{M-1}{2} T_r}$$

$$\cdot \text{sinc} \left(\left(f_d - f_D \left(1 + \frac{B}{K f_c} l \right) \right) M T_r \right). \tag{B.8}$$

B.3   Target signature in fast-time/slow-frequency

Starting from equation (B.7), the fast-time/slow-frequency target signature is obtained by applying inverse FT over fast-frequency:

$$s_{\text{ft,sf}}(f, f_d) = \alpha M \int |S(f)|^2 \, e^{-j2\pi\tau_0 f} e^{j2\pi\left(f_d - f_D\left(1 + \frac{f}{f_c}\right)\right)\frac{T_r}{2}}$$

$$\cdot e^{-j2\pi\left(f_d - f_D\left(1 + \frac{f}{f_c}\right)\right)\frac{MT_r}{2}} \operatorname{sinc}\left(\left(f_d - f_D\left(1 + \frac{f}{f_c}\right)\right)MT_r\right) e^{j2\pi tf} df$$

$$= \alpha M e^{j2\pi(f_d - f_D)\frac{T_r}{2}} \int |S(f)|^2 \, e^{-j2\pi\left(\tau_0 + \frac{f_D T_r}{2f_c}\right)f} \tag{B.9}$$

$$\cdot e^{-j2\pi\frac{1}{2}\left((f_d - f_D)MT_r - \frac{f_D MT_r}{f_c}f\right)} \operatorname{sinc}\left((f_d - f_D)MT_r - \frac{f_D MT_r}{f_c}f\right) e^{j2\pi tf} df.$$

To preform inverse FT, remind its properties:

$$F^{-1}\left(G(f)\right) = g(t);$$

$$F^{-1}\left(G(k_0 f + f_0)e^{-j2\pi f t_0}\right) = \frac{1}{|k_0|} g\left(\frac{t - t_0}{k_0}\right) e^{-j2\pi f_0 \frac{t - t_0}{k_0}};$$

$$F^{-1}\left(G(f)H(f)\right) = g(t) * h(t); \tag{B.10}$$

$$F^{-1}\left(\operatorname{sinc}(f)e^{-j2\pi\frac{f}{2}}\right) = \Pi_{[0,1]}(t),$$

where $g(t)*h(t)$ denotes convolution of functions $g(t)$ and $h(t)$ and $\Pi_{[t_1,t_2]}(t)$ is defined in (2.20). Applying these properties to (B.9) and using $\frac{f_D}{f_c} = \frac{2v_0}{c}$, one can obtain:

$$s_{\text{ft,sf}}(f, f_d) = \alpha \left|\frac{f_c}{f_D T_r}\right| e^{j2\pi(f_d - f_D)\frac{T_r}{2}} \cdot u_{\text{p}}(t)$$

$$*\Pi_{[0,1]}\left(\frac{t - \left(\tau_0 + \frac{f_D T_r}{2f_c}\right)}{-\frac{f_D MT_r}{f_c}}\right) e^{-j2\pi(f_d - f_D)MT_r\left(\frac{t - \left(\tau_0 + \frac{f_D T_r}{2f_c}\right)}{-\frac{f_D MT_r}{f_c}}\right)} \tag{B.11}$$

$$= \alpha \left|\frac{f_c}{f_D T_r}\right| u_{\text{p}}(t) * \Pi_{[\tau_0 + \frac{2}{c}\frac{v_0 T_r}{2}, \tau_0 + \frac{2}{c}\frac{v_0 T_r}{2} - \frac{2}{c}v_0 MT_r]}(t)$$

$$\cdot e^{j2\pi(f_d - f_D)\left(\frac{f_c}{f_D}\left(t - \left(\tau_0 + \frac{2}{c}\frac{v_0 T_r}{2}\right)\right) + \frac{T_r}{2}\right)},$$

assuming $v_0 < 0$ (and so target range is increasing function of time) to set the limits of $\Pi_{[t_1,t_2]}(t)$. In case $v_0 > 0$ the limits should be flipped. The term $\frac{f_c}{f_D T_r} = \frac{B\delta_R}{v_0 T_r}$ expresses the magnitude of the target response in the range/Doppler domain. Sampling the target signature in the fast-time withing the LRRS of interest as $k = tB - k_{\text{beg}}$ and assuming $u_{\text{p}}(k) \approx \delta(k)$ and negligible range-walk of a target withing one PRI compared to the range resolution (and thus the term $\frac{2}{cB}\frac{v_0 T_r}{2} < \delta_R$ is neglected) gives

the target signature:

$$T_{\mathrm{ft,sf}}(k, f_d) \approx \left| \frac{\delta_R}{v_0 T_r} \right| \Pi_{[k_0, k_0 - \frac{v_0 M T_r}{\delta_R}]}(k)\, e^{j2\pi(f_d - f_D)\left(\frac{f_c}{B f_D}(k - k_0) + \frac{T_r}{2}\right)}. \qquad (\text{B.12})$$

Note that if the signal is sampled in the range domain, the limits of the function $\Pi_{[t_1, t_2]}(t)$ should be rounded to the nearest integers.

Appendix C

Clutter suppression with wideband coherent waveform

This appendix demonstrates how the parameters of the wideband waveform affect the ability of clutter suppression using range migration.

The analysis in performed in fast-time (range) k / slow (Doppler) frequency f_d domain. In this case the response of a moving target with velocity v_0 and range cell at the beginning of CPI k_0 can be expressed as (see Appendix B.3):

$$S_{\mathrm{ft,sf}}(k, f_d; k_0, v_0) \approx \alpha \left| \frac{f_c}{f_D B T_r} \right| \Pi_{[k_0, k_0 - \frac{v_0 M T_r}{\delta_R}]}(k) \, e^{j\psi(k, f_d; k_0, v_0)}, \qquad (C.1)$$

where $f_D = f_c \frac{2v_0}{c}$, or $\frac{\delta_R}{v_0 T_r} = \frac{f_c}{f_D B T_r}$, and

$$\psi(k, f_d; k_0, v_0) = 2\pi \left(f_d - f_D \right) \left(\frac{f_c}{B f_D} \left(k - k_0 \right) + \frac{T_r}{2} \right). \qquad (C.2)$$

Since radar clutter is usually characterized by its PSD in the Doppler domain, the analysis of clutter suppression with the wideband waveform is performed in the range/Doppler frequency domain. Rewrite the target signature in terms of folded Doppler frequency, which can be directly measured with the considered waveform. Define the Doppler cell sampled at the nominal Doppler resolution of the waveform $\delta_{f_D} = F_r/M$ by $d = \left[M\mathrm{frac}\left(\frac{f_d}{F_r} \right) \right]$, where $d = -M/2 + 1, \ldots, M/2$. From (2.18) and discussion afterwards the Doppler spectrum of the target (with $v_0 < 0$) is spread from $d_l = \left[M\mathrm{frac}\left(f_d F_r \left(1 + \frac{B}{f_c} \right) \right) \right]$ to $d_u = [M\mathrm{frac}\left(f_d F_r \right)]$. For the target competing with the clutter ambiguity, it can be assumed that its whole Doppler spectrum lies in the same Doppler ambiguity with index n, and then $d_l = \left[M\mathrm{frac}\left(f_d F_r \right) + \frac{M v_0 T_r}{\delta_R} \right]$.
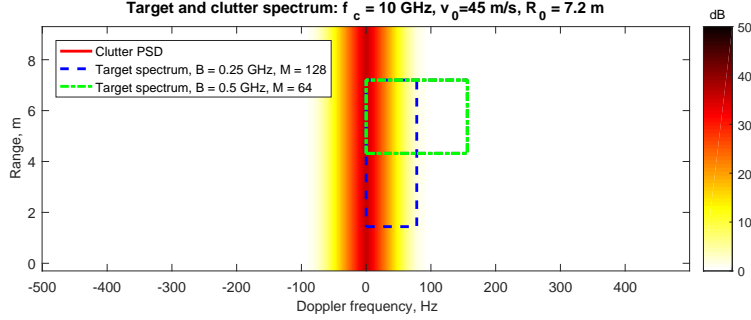
Figure C.1: Clutter and target range-Doppler spectrum for two waveforms with equal time-bandwidth product ($f_c = 10$ GHz): (blue) - $B = 0.25$ GHz, $M = 128$; (green) - $B = 0.5$ GHz, $M = 64$.

Considering that the magnitude of the target response is small outside its range and Doppler spread (approximating $u_{\mathrm{p}}^*(k) \approx \delta(k)$), the target response in fast-time (range) / folded Doppler domain is expressed by:

$$S_{\mathrm{ft,fD}}(k, d; k_0, v_0) \approx \begin{cases} \frac{\alpha}{|f_D|} \frac{f_c}{BT_r} e^{j\psi'(k,d;k_0,v_0)}, k \in \left[k_0, k_0 - \frac{v_0 M T_r}{\delta_R}\right] \cap d \in [d_l, d_u]; \\ 0, k \notin \left[k_0, k_0 - \frac{v_0 M T_r}{\delta_R}\right] \cup d \notin [d_l, d_u], \end{cases}$$

(C.3)

with $\psi'(k, d; k_0, v_0)$ being the counterpart of (C.2) for the sampled Doppler frequency. The applicability of this approximation can be checked in Fig. 2.2, b.

The target signature in the range/Doppler domain, allows SCNR (3.7) representation after clutter filtering in the form [2, 49]:

$$\begin{aligned} \mathrm{SCNR}\,(k_0, v_0) &\approx \sum_{k=k_0}^{k_0 - \frac{v_0 M T_r}{\delta_R}} \sum_{d=d_l}^{d_u} \frac{|S_{\mathrm{ft,fD}}(k, d; k_0, v_0)|^2}{P_{\mathrm{cl}}(k, d\delta_{f_D}) + P_{\mathrm{n}}(k, d\delta_{f_D})} \\ &= \frac{|\alpha|^2}{|f_D|^2} \sum_{k=k_0}^{k_0 - \frac{v_0 M T_r}{\delta_R}} \sum_{d=d_u + \frac{M v_0 T_r}{\delta_R}}^{d_u} \frac{1}{P_{\mathrm{cl}}(d\delta_{f_D}) + P_{\mathrm{n}}}, \end{aligned}$$

(C.4)

where the clutter dependence on the range cell k and the noise dependence on the range and Doppler frequency have been omitted under the assumption on their homogeneity: $P_{\mathrm{cl}}(k, f_d) = P_{\mathrm{cl}}(f_d), \forall k = 0, \ldots, K - 1$ and $P_{\mathrm{n}}(k, f_d) = P_{\mathrm{n}}, \forall k = 0, \ldots, K - 1, \forall f_d \in [-F_r/2, F_r/2]$. Skipping the dependence of SCNR on k_0 for the

same reason, the SCNR loss at velocity v_0 can be expressed as:

$$\mathrm{L}\left(v_0\right) \approx \left(\sum_{d=d_u+\frac{Mv_0T_r}{\delta_R}}^{d_u} \frac{1}{P_{\mathrm{cl}}(d\delta_{f_D}) + P_{\mathrm{n}}}\right) \bigg/ \left(\sum_{d=d_u+\frac{Mv_0T_r}{\delta_R}}^{d_u} \frac{1}{P_{\mathrm{n}}}\right)$$

$$= \sum_{d=d_u+\frac{Mv_0T_r}{\delta_R}}^{d_u} \frac{1}{\mathrm{CNR}(d\delta_{f_D}) + 1}.$$

(C.5)

The analysis of (C.5) demonstrates that the SCNR loss depends on the target migration $v_0 M T_r / \delta_R$, PSD of competing clutter and Doppler resolution of the waveform δ_{f_D}. It can be noted, that larger bandwidth of the transmitted waveform provides wider Doppler spectrum of the target, over which clutter spectrum is averaged in (C.5), as the green line in Fig. C.1 shows. Increasing the CPI of the waveform, on the other hand, results in larger range migration of the target, demonstrated with the blue line in Fig. C.1, but with no enlargement of its Doppler spectrum (hence it is sampled with more dense Doppler resolution δ_{f_D}). As the result, the loss factor at velocity ambiguity can be improved only with the increase of the bandwidth in (C.5). Therefore, the efficiency of clutter ambiguity suppression with the wideband waveform is determined by the bandwidth of the transmitted signal.
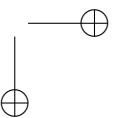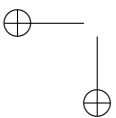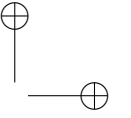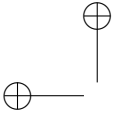
Appendix D

Detector of a range migrating target in spiky clutter

D.1 Convergence analysis

In this appendix, we derive the sufficient condition for the convergence of the iterative estimation of $\sigma_{\mathcal{K}}^H$. We consider the case $H = 0$ for simplicity and skip the subindex (H) in notations for simplicity; the analysis under H_1 can be performed in a similar manner. Since $\sigma_k > 0, \forall k \in \mathcal{K}$, we use for our analysis an equivalent form of (6.24):

$$\left(\frac{1}{\sigma_k}\right)^2 + \left(\frac{1}{\sigma_k}\right) \sum_{j=0,j\neq k}^{K-1} \frac{\Re\left(q_{k,j}\right)}{q_{k,k}} \frac{1}{\sigma_j} - \frac{M}{q_{k,k}} = 0, \tag{D.1}$$

and find the unique positive solution of the quadratic equation by:

$$\sigma_k^{-1} = g(\sigma_k^{-1}) = \frac{1}{2}\left(-b_k + \sqrt{D_k}\right), \tag{D.2}$$

where $b_k = \sum_{j=0,j\neq k}^{K-1} \frac{\Re(q_{k,j})}{q_{k,k}} \frac{1}{\sigma_j}$ and $D_k = \left(\sum_{j=0,j\neq k}^{K-1} \frac{\Re(q_{k,j})}{q_{k,k}} \frac{1}{\sigma_j}\right)^2 + \frac{4M}{q_{k,k}}$. The K equations defined by (D.2) can be written in a form of fixed point matrix equation:

$$\sigma_{\mathcal{K}}^{-1} = \mathbf{G}(\sigma_{\mathcal{K}}^{-1}). \tag{D.3}$$

The system of K equitation for $g(\sigma_k^{-1})$ converges at least linearly if $||\mathbf{J_G}\left(\sigma_{\mathcal{K}}^{-1}\right)|| < 1$, where $\mathbf{J_G}\left(\sigma_{\mathcal{K}}^{-1}\right)$ is the Jacobian matrix of the first partial derivatives of $\mathbf{G}$ evaluated at $\sigma_{\mathcal{K}}^{-1}$ and $|| \cdot ||$ is any induced matrix norm [100].

The first partial derivatives of (D.2) have the form:

$$\frac{\partial g\left(\sigma_k^{-1}\right)}{\partial\left(\sigma_k^{-1}\right)} = 0; \tag{D.4}$$

$$\frac{\partial g\left(\sigma_k^{-1}\right)}{\partial\left(\sigma_j^{-1}\right)} = -\frac{\Re\left(q_{k,j}\right)}{q_{k,k}}\left(\frac{-b_k+\sqrt{D_k}}{2\sqrt{D_k}}\right) \tag{D.5}$$

and by selecting the infinite matrix norm, we can write:

$$\begin{aligned}
||\mathbf{J_G}\left(\sigma_{\mathcal{K}}^{-1}\right)||_\infty &= \max_k \sum_{j=0,j\neq k}^{K-1} \left|\frac{\Re\left(q_{k,j}\right)}{q_{k,k}}\left(\frac{-b_k+\sqrt{D_k}}{2\sqrt{D_k}}\right)\right| \\
&\leq \max_k \sum_{j=0,j\neq k}^{K-1} \left|\frac{\Re\left(q_{k,j}\right)}{q_{k,k}}\right|,
\end{aligned} \tag{D.6}$$

where we used the fact that (D.1) has two real roots of different sign. The sufficient, but not necessary condition for convergence can be given:

$$\sum_{j=0,j\neq k}^{K-1} \left|\frac{\Re\left(q_{k,j}\right)}{q_{k,k}}\right| < 1, \quad \forall k \in \mathcal{K}, \tag{D.7}$$

which is the function of the data and CM $\mathbf{Q}$, but not the function of the initialization or current estimation $\sigma_{\mathcal{K}}$. So, if the estimation converges for a particular realization of the data, it does so with any initialization of $\sigma_{\mathcal{K}} \in \mathbb{R}_{>0}$.

Under H_0, the same can be written in terms of the speckle component:

$$\sum_{j=0,j\neq k}^{K-1} \frac{\sigma_j\left|\Re\left(\mathbf{g_k}^H\mathbf{Q_{k,j}}^{-1}\mathbf{g_j}\right)\right|}{\sigma_k\mathbf{g_k}^H\mathbf{Q_{k,k}}^{-1}\mathbf{g_k}} < 1, \quad \forall k \in \mathcal{K}. \tag{D.8}$$

By denoting $r_{k,j} = \frac{\mathbf{g_k}^H\mathbf{Q_{k,j}}^{-1}\mathbf{g_j}}{\mathbf{g_k}^H\mathbf{Q_{k,k}}^{-1}\mathbf{g_k}}$ the speckle range correlation coefficient, it becomes

$$\sum_{j=0,j\neq k}^{K-1} \frac{\sigma_j}{\sigma_k}\left|\Re\left(r_{k,j}\right)\right| < 1, \quad \forall k \in \mathcal{K}. \tag{D.9}$$

Thus, the iterative algorithm converges linearly to the unique solution if for any range cell k the clutter correlation with all the other range cells j, weighted by the ratio of the square root of power in that range cells is bounded. The latter has very simple physical interpretation: if the clutter is correlated in range, its power cannot fluctuate very rapidly with the range.

Remark: in our numerous numerical simulations and real data analysis, we never met a situation when the algorithm did not converge, even if the condition (D.9) for the particular realization was not satisfied.

D.2   Approximate solution

In this appendix, we solve (6.25) by expanding it in Taylor series around the approximate solution $\breve{\sigma}_k^{(H)}$:

$$
f(\sigma_k^{(H)}) = \left(\sigma_k^{(H)}\right)^2 + b_k^{(H)}\sigma_k^{(H)} + c_k^{(H)}
$$
$$
\approx f(\breve{\sigma}_k^{(H)}) + \left.\frac{\partial f(\sigma_k^{(H)})}{\partial \sigma_k^{(H)}}\right|_{\sigma_k^{(H)}=\breve{\sigma}_k^{(H)}} \left(\sigma_k^{(H)} - \breve{\sigma}_k^{(H)}\right),
$$

(D.10)

and select for the initial approximation the root of $f(\sigma_k^{(H)})$ in case of IIM, i.e.: $\breve{\sigma}_k^{(H)} = \sqrt{-c_k^{(H)}}$. The solution of $f(\sigma_k^{(H)}) = 0$ is:

$$
\hat{\sigma}_k^{(H)} \approx \frac{-2c_k^{(H)}}{2\sqrt{-c_k^{(H)}} + b_k^{(H)}}.
$$

(D.11)

The latter estimation of $\hat{\sigma}_k^{(H)}$ is still iterative since the coefficients depend on the other unknowns, but it can be calculated more efficiently than the original equation for $\hat{\sigma}_k^{(H)}$, especially under H_0 since $c_k^{(0)}$ does not vary with iterations. The proposed fast estimation especially applicable for the speckle CM estimation (6.35) with moderate range correlation.

D.3   Detector of a target crossing a clutter boundary

It is assumed that clutter inhomogeneity can be modeled in terms of SIRVs and two non-overlapping regions of clutter are present in the LRRS under test. To design the detector for this scenario, it is assumed that the transition between these two regions is known, so the range cells in the LRRS under test can be divided into two non-overlapping sets: $\mathcal{K}_0$ and $\mathcal{K}_1$, satisfying $\mathcal{K}_0 \cap \mathcal{K}_1 = \{\}$, $\mathcal{K}_0 \cup \mathcal{K}_1 = \mathcal{K}$, $\mathrm{card}(\mathcal{K}_0) = N$ and $\mathrm{card}(\mathcal{K}_1) = K - N$, with $1 < N < K$. Herein $\cap$ stands for the sets intersection, $\cup$ for the sets union, $\mathrm{card}(\cdot)$ for the cardinality of the set and $\{\}$ for the empty set. Denote unknown clutter power in each group by scalars $\tilde{\sigma}_0$ and $\tilde{\sigma}_1$ and perform the procedure similar to the above. The estimations of $\hat{\tilde{\sigma}}_0$ and $\hat{\tilde{\sigma}}_1$ are the positive roots of the system of two equations:

$$
\begin{cases}
\left(\tilde{\sigma}_{\mathcal{K}_0}^{(H)}\right)^2 - \tilde{\sigma}_{\mathcal{K}_0}^{(H)} \dfrac{\Re\left(\tilde{q}_{0,1}^{(H)}\right)}{NM\sigma_{\mathcal{K}_1}^{(H)}} - \dfrac{\tilde{q}_{0,0}^{(H)}}{NM} = 0; \\[2ex]
\left(\tilde{\sigma}_{\mathcal{K}_1}^{(H)}\right)^2 - \tilde{\sigma}_{\mathcal{K}_1}^{(H)} \dfrac{\Re\left(\tilde{q}_{1,0}^{(H)}\right)}{(K-N)M\sigma_{\mathcal{K}_0}^{(H)}} - \dfrac{\tilde{q}_{1,1}^{(H)}}{(K-N)M} = 0,
\end{cases}
$$

(D.12)

where $\tilde{q}_{p,s}^{(H)} = \sum_{i \in \mathcal{K}_p} \sum_{j \in \mathcal{K}_s} q_{i,j}^{(H)}$. The estimation of $\hat{\alpha}$ is found similarly from (6.27) with $\hat{\mathbf{M}}^{(1)} = \mathbf{M}\big|_{\sigma_\mathcal{K} = \hat{\sigma}_\mathcal{K}^{(1)}}$. The detection test is:

$$\Lambda(\mathbf{y}) = \prod_{i=0}^{1} \left(\frac{\hat{\sigma}_{\mathcal{K}_i}^{(0)}}{\hat{\sigma}_{\mathcal{K}_i}^{(1)}} \right)^{2M \mathrm{card}(\mathcal{K}_i)} \underset{H_0}{\overset{H_1}{\gtrless}} T. \qquad (D.13)$$

The proposed solution is computationally more efficient than (6.31) since it only requires to solve the system of 2 equations instead of K under each hypothesis. However, clutter spatial distribution should be known *a priori* to set the boundaries between different regions, which makes the detector less adaptive to the scene. In practice, these boundaries are unknown and therefore have to be estimated from the clutter map with an appropriate edge detection technique (e.g. Canny or Sobel's edge detectors [89]).

Bibliography

[1] M. Skolnik, *Radar Handbook, Third Edition*. McGraw-Hill Education, 2008.

[2] F. Le Chevalier, *Principles of Radar and Sonar Signal Processing*. Artech House, 2002.

[3] M. A. Richards, J. A. Scheer, W. A. Holm, and W. L. Melvin, *Principles of Modern Radar*. SciTech Pub., 2010.

[4] P. J. Prinsen, "Elimination of blind velocities of MTI radar by modulating the interpulse period," *IEEE Transactions on Aerospace and Electronic Systems*, no. 5, pp. 714–724, 1973.

[5] L. Y. Astanin and A. A. Kostylev, *Ultrawideband Radar Measurements: Analysis and Processing*. IET, 1997.

[6] J. D. Taylor, *Advanced Ultrawideband Radar: Signals, Targets, and Applications*. CRC Press, 2016.

[7] J. Xu, J. Yu, Y.-N. Peng, and X.-G. Xia, "Radon-Fourier transform for radar target detection (II): blind speed sidelobe suppression," *IEEE Transactions on Aerospace and Electronic Systems*, vol. 47, no. 4, pp. 2473–2489, 2011.

[8] F. Deudon, S. Bidon, O. Besson, and J.-Y. Tourneret, "Velocity dealiased spectral estimators of range migrating targets using a single low-PRF wideband waveform," *IEEE Transactions on Aerospace and Electronic Systems*, vol. 49, no. 1, pp. 244–265, 2013.

[9] S. Bidon, J.-Y. Tourneret, L. Savy, and F. Le Chevalier, "Bayesian sparse estimation of migrating targets for wideband radar," *IEEE Transactions on Aerospace and Electronic Systems*, vol. 50, no. 2, pp. 871–886, 2014.

[10] E. Conte, A. De Maio, and G. Ricci, "GLRT-based adaptive detection algorithms for range-spread targets," *IEEE Transactions on Signal Processing*, vol. 49, no. 7, pp. 1336–1348, 2001.

[11] K. Gerlach, "Spatially distributed target detection in non-Gaussian clutter," *IEEE Transactions on Aerospace and Electronic Systems*, vol. 35, no. 3, pp. 926–934, 1999.

[12] E. Conte, A. d. Maio, and G. Ricci, "CFAR detection of distributed targets in non-Gaussian disturbance," *IEEE Transactions on Aerospace and Electronic Systems*, vol. 38, no. 2, pp. 612–621, 2002.

[13] F. Dai, H. Liu, P. Shui, and S. Wu, "Adaptive detection of wideband radar range spread targets with range walking in clutter," *IEEE Transactions on Aerospace and Electronic Systems*, vol. 48, no. 3, pp. 2052–2064, 2012.

[14] J. Xu, J. Yu, Y.-N. Peng, and X.-G. Xia, "Radon-Fourier transform for radar target detection (I): generalized Doppler filter bank," *IEEE Transactions on Aerospace and Electronic Systems*, vol. 47, no. 2, pp. 1186–1202, 2011.

[15] T. Yardibi, J. Li, P. Stoica, M. Xue, and A. B. Baggeroer, "Source localization and sensing: a nonparametric iterative adaptive approach based on weighted least squares," *IEEE Transactions on Aerospace and Electronic Systems*, vol. 46, no. 1, pp. 425–443, 2010.

[16] W. Roberts, P. Stoica, J. Li, T. Yardibi, F. Sadjadi *et al.*, "Iterative adaptive approaches to MIMO radar imaging," *IEEE Journal of Selected Topics in Signal Processing*, vol. 4, no. 1, pp. 5–20, 2010.

[17] P. Stoica, P. Babu, and J. Li, "SPICE: a sparse covariance-based estimation method for array processing," *IEEE Transactions on Signal Processing*, vol. 59, no. 2, pp. 629–638, 2011.

[18] P. Stoica, D. Zachariah, and J. Li, "Weighted SPICE: a unifying approach for hyperparameter-free sparse estimation," *Digital Signal Processing*, vol. 33, pp. 1–12, 2014.

[19] S. Bidon, O. Besson, J.-Y. Tourneret, and F. Le Chevalier, "Bayesian sparse estimation of migrating targets in autoregressive noise for wideband radar," in *2014 IEEE Radar Conference.* IEEE, 2014, pp. 0579–0584.

[20] J. B. Billingsley, "Exponential decay in windblown radar ground clutter doppler spectra: multifrequency measurements and model," DTIC Document, Tech. Rep., 1996.

[21] A. De Maio and M. Greco, *Modern Radar Detection Theory.* SciTech Pub., 2016.

[22] K. J. Sangston and A. Farina, "Coherent radar detection in Compound-gaussian clutter: Clairvoyant detectors," *IEEE Aerospace and Electronic Systems Magazine*, vol. 31, no. 11, pp. 42–63, 2016.

[23] K. J. Sangston, F. Gini, M. Greco, and A. Farina, "Structures for radar detection in compound-Gaussian clutter," *IEEE Transactions on Aerospace and Electronic Systems*, vol. 35, no. 2, pp. 445–458, 1999.

[24] O. A. Krasnov, L. P. Ligthart, Z. Li, P. Lys, and F. Van der Zwan, "The PARSAX — full polarimetric fmcw radar with dual-orthogonal signals," in *2008 European Radar Conference*, 2008.

[25] G. Babur, "Processing of dual-orthogonal CW polarimetric radar signals," Ph.D. dissertation, TU Delft, Delft University of Technology, 2009.

[26] D. R. Wehner, *High-resolution radar*. Artech House, 1995.

[27] F. Nathanson, P. Reilly, and M. Cohen, *Radar design principles*. Scitech publishing, 1999.

[28] J. Li and P. Stoica, "Efficient mixed-spectrum estimation with applications to target feature extraction," *IEEE transactions on signal processing*, vol. 44, no. 2, pp. 281–295, 1996.

[29] X. Chen, J. Guan, N. Liu, and Y. He, "Maneuvering target detection via Radon-fractional fourier transform-based long-time coherent integration," *IEEE Transactions on Signal Processing*, vol. 62, no. 4, pp. 939–953, 2014.

[30] X. Li, L. Kong, G. Cui, and W. Yi, "Clean-based coherent integration method for high-speed multi-targets detection," *IET Radar, Sonar & Navigation*, vol. 10, no. 9, pp. 1671–1682, 2016.

[31] F. Uysal and N. Goodman, "The effect of moving target on range-Doppler map and backprojection algorithm for focusing," in *Radar Conference (RadarConf)*. IEEE, 2016, pp. 1–5.

[32] Q. Li, E. J. Rothwell, K.-M. Chen, and D. P. Nyquist, "Scattering center analysis of radar targets using fitting scheme and genetic algorithm," *IEEE Transactions on Antennas and Propagation*, vol. 44, no. 2, pp. 198–207, 1996.

[33] R. V. Ostrovitianov and F. A. Basalov, *Statistical theory of extended radar targets*. Artech House Publishers, 1985, translation from the Russian of 'Statisticheskaya teoriya radiolokatsii protyazhennyh tselei'.

[34] S. Watts, "Radar detection prediction in K-distributed sea clutter and thermal noise," *IEEE Transactions on Aerospace Electronic Systems*, vol. 23, pp. 40–45, 1987.

[35] A. Farina, F. Gini, M. Greco, and L. Verrazzani, "High resolution sea clutter data: statistical analysis of recorded live data," in *IEE Proceedings - Radar, Sonar and Navigation*, vol. 144, no. 3.   IET, 1997, pp. 121–130.

[36] N. Pulsone and R. Raghavan, "Analysis of an adaptive CFAR detector in non-Gaussian interference," *IEEE Transactions on Aerospace and Electronic Systems*, vol. 35, no. 3, pp. 903–916, 1999.

[37] M. Greco and F. Gini, "Statistical analysis of high-resolution SAR ground clutter data," *IEEE Transactions on Geoscience and Remote Sensing*, vol. 45, no. 3, pp. 566–575, 2007.

[38] E. Jakeman and P. Pusey, "Significance of K distributions in scattering experiments," *Physical Review Letters*, vol. 40, no. 9, p. 546, 1978.

[39] G. Trunk, "Radar properties of non-Rayleigh sea clutter," *IEEE Transactions on Aerospace and Electronic Systems*, no. 2, pp. 196–204, 1972.

[40] K. D. Ward, S. Watts, and R. J. Tough, *Sea Clutter: Scattering, the K-Distribution and Radar Performance*.   IET, 2006.

[41] F. Deudon, F. Le Chevalier, S. Bidon, O. Besson, and L. Savy, "A migrating target indicator for wideband radar," in *Sensor Array and Multichannel Signal Processing Workshop (SAM), 2010 IEEE*.   IEEE, 2010, pp. 249–252.

[42] F. Le Chevalier, O. Krasnov, F. Deudon, and S. Bidon, "Clutter suppression for moving targets detection with wideband radar," in *19th European Signal Processing Conference*.   IEEE, 2011, pp. 427–430.

[43] W. Fishbein, S. W. Graveline, and O. E. Rittenbach, "Clutter attenuation analysis," Army electronics command fort Monmouth NJ, Tech. Rep., 1967.

[44] E. J. Barlow, "Doppler radar," *Proceedings of the IRE*, vol. 37, no. 4, pp. 340–355, 1949.

[45] P. Lombardo, M. Greco, F. Gini, A. Farina, and B. Billingsley, "Impact of clutter spectra on radar performance prediction," *IEEE Transactions on Aerospace and Electronic Systems*, vol. 37, no. 3, pp. 1022–1038, 2001.

[46] M. Greco, F. Gini, A. Farina, and J. Billingsley, "Validation of windblown radar ground clutter spectral shape," *IEEE Transactions on Aerospace and Electronic Systems*, vol. 37, no. 2, pp. 538–548, 2001.

BIBLIOGRAPHY   157

[47] P. Lombardo and J. Billingsley, "A new model for the Doppler spectrum of windblown radar ground clutter," in *IEEE Radar Conference*. IEEE, 1999, pp. 142–147.

[48] R. Klemm, *Principles of space-time adaptive processing*. IET, 2002.

[49] S. M. Kay, *Fundamentals of Statistical Signal Processing, Vol. II: Detection Theory*. Prentice Hall, 1998.

[50] P. Stoica, P. Babu, and J. Li, "New method of sparse parameter estimation in separable models and its use for spectral analysis of irregularly sampled data," *IEEE Transactions on Signal Processing*, vol. 59, no. 1, pp. 35–47, 2011.

[51] F. Le Chevalier, "Target detection method and device for wideband unambiguous pulse Doppler radar," 1999, US Patent 5,977,905.

[52] S. Bidon, L. Savy, and F. Deudon, "Fast coherent integration for migrating targets with velocity ambiguity," in *2011 IEEE Radar Conference (RADAR)*. IEEE, 2011, pp. 027–032.

[53] S. Bidon, F. Deudon, O. Krasnov, and F. Le Chevalier, "Coherent integration for wideband LFMCW applied to PARSAX experimental data," in *2011 European Radar Conference (EuRAD)*, Oct 2011, pp. 257–260.

[54] J. Yu, J. Xu, Y.-N. Peng, and X.-G. Xia, "Radon-Fourier transform for radar target detection (III): optimality and fast implementations," *IEEE Transactions on Aerospace and Electronic Systems*, vol. 48, no. 2, pp. 991–1004, 2012.

[55] J. R. Guerci, *Space-time Adaptive Processing for Radar*. Artech House, 2014.

[56] J. Li and P. Stoica, "An adaptive filtering approach to spectral estimation and SAR imaging," *IEEE Transactions on Signal Processing*, vol. 44, no. 6, pp. 1469–1484, 1996.

[57] S. Bidon, M. Lasserre, and F. Le Chevalier, "Bayesian sparse estimation of radar targets in the compressed sensing framework," in *Compressive Sensing of Earth Observations*, C.-h. Chen, Ed. CRC Press, 2017, ch. 7.

[58] M. Lasserre, S. Bidon, and F. Le Chevalier, "New sparse-promoting prior for the estimation of a radar scene with weak and strong targets." *IEEE Transactions on Signal Processing*, vol. 64, no. 17, pp. 4634–4643, 2016.

[59] ——, "Velocity ambiguity mitigation of off-grid range migrating targets via Bayesian sparse recovery," in *Statistical Signal Processing Workshop (SSP), 2016 IEEE*. IEEE, 2016, pp. 1–5.

[60] Z. Yang, X. Li, H. Wang, and W. Jiang, "Adaptive clutter suppression based on iterative adaptive approach for airborne radar," *Signal Processing*, vol. 93, no. 12, pp. 3567–3577, 2013.

[61] C. R. Rojas, D. Katselis, and H. Hjalmarsson, "A note on the SPICE method," *IEEE transactions on signal processing*, vol. 61, no. 18, pp. 4545–4551, 2013.

[62] P. B. Tuuk and S. L. Marple, "Compressed sensing radar amid noise and clutter using interference covariance information," *IEEE Transactions on Aerospace and Electronic Systems*, vol. 50, no. 2, pp. 887–897, 2014.

[63] S. Kraut, L. L. Scharf, and L. T. McWhorter, "Adaptive subspace detectors," *IEEE Transactions on Signal Processing*, vol. 49, no. 1, pp. 1–16, 2001.

[64] E. Kelly, "An adaptive detection algorithm," *IEEE Transactions on Aerospace and Electronic Systems*, vol. 22, no. 2, pp. 115–127, 1986.

[65] F. Robey, D. Fuhrmann, E. Kelly, and R. Nitzberg, "A CFAR adaptive matched filter detector," *IEEE Transactions on Aerospace and Electronic Systems*, vol. 28, no. 1, pp. 208–216, 1992.

[66] J. Liu, Z.-J. Zhang, Y. Yang, and H. Liu, "A CFAR adaptive subspace detector for first-order or second-order Gaussian signals based on a single observation," *IEEE Transactions on Signal Processing*, vol. 59, no. 11, pp. 5126–5140, 2011.

[67] O. Besson, E. Chaumette, and F. Vincent, "Adaptive detection of a Gaussian signal in Gaussian noise," in *Computational Advances in Multi-Sensor Adaptive Processing (CAMSAP), 2015 IEEE 6th International Workshop on.* IEEE, 2015, pp. 117–120.

[68] P. Stoica and Y. Selen, "Model-order selection: a review of information criterion rules," *IEEE Signal Processing Magazine*, vol. 21, no. 4, pp. 36–47, 2004.

[69] M. Wax and T. Kailath, "Detection of signals by information theoretic criteria," *IEEE Transactions on Acoustics, Speech, and Signal Processing*, vol. 33, no. 2, pp. 387–392, 1985.

[70] Y. Sakamoto, M. Ishiguro, and G. Kitagawa, "Akaike information criterion statistics," *Dordrecht, The Netherlands: D. Reidel*, vol. 81, 1986.

[71] J. Li, X. Zhu, P. Stoica, and M. Rangaswamy, "High resolution angle-Doppler imaging for MTI radar," *IEEE Transactions on Aerospace and Electronic Systems*, vol. 46, no. 3, pp. 1544–1556, 2010.

[72] J. Tsao and B. D. Steinberg, "Reduction of sidelobe and speckle artifacts in microwave imaging: the clean technique," *IEEE Transactions on Antennas and Propagation*, vol. 36, no. 4, pp. 543–556, 1988.

[73] Z.-S. Liu and J. Li, "Implementation of the RELAX algorithm," *IEEE Transactions on aerospace and electronic systems*, vol. 34, no. 2, pp. 657–664, 1998.

[74] R. Ravid and N. Levanon, "Maximum-likelihood CFAR for Weibull background," in *IEE Proceedings F (Radar and Signal Processing)*, vol. 139, no. 3. IET, 1992, pp. 256–264.

[75] G. Goldstein, "False-alarm regulation in log-normal and Weibull clutter," *IEEE Transactions on Aerospace and Electronic Systems*, no. 1, pp. 84–92, 1973.

[76] K. J. Sangston and K. R. Gerlach, "Non-Gaussian noise models and coherent detection of radar targets," Naval research lab Washington DC, Tech. Rep., 1992.

[77] E. Conte, M. Longo, and M. Lops, "Modelling and simulation of non-Rayleigh radar clutter," in *IEE Proceedings - Radar and Signal Processing*, vol. 138, no. 2. IET, 1991, pp. 121–130.

[78] E. Conte and M. Longo, "Characterisation of radar clutter as a spherically invariant random process," *IEE Proceedings - Communications, Radar and Signal Processing*, vol. 134, no. 2, pp. 191–197, 1987.

[79] F. Pascal, P. Forster, J.-P. Ovarlez, and P. Larzabal, "Performance analysis of covariance matrix estimates in impulsive noise," *IEEE Transactions on Signal Processing*, vol. 56, no. 6, pp. 2206–2217, 2008.

[80] F. Gini and A. Farina, "Matched subspace CFAR detection of hovering helicopters," *IEEE Transactions on Aerospace and Electronic Systems*, vol. 35, no. 4, pp. 1293–1305, 1999.

[81] H. S. Kim, "Adaptive target detection in radar imaging," Ph.D. dissertation, University of Michigan, 2001.

[82] F. L. Posner, "Texture and speckle in high resolution synthetic aperture radar clutter," *IEEE Transactions on Geoscience and Remote Sensing*, vol. 31, no. 1, pp. 192–203, 1993.

[83] R. Couillet, M. S. Greco, J.-P. Ovarlez, and F. Pascal, "RMT for whitening space correlation and applications to radar detection," in *6th International Workshop on Computational Advances in Multi-Sensor Adaptive Processing (CAMSAP)*. IEEE, 2015, pp. 149–152.

[84] A. Aubry, A. De Maio, G. Foglia, C. Hao, and D. Orlando, "Radar detection and range estimation using oversampled data," *IEEE Transactions on Aerospace and Electronic Systems*, vol. 51, no. 2, pp. 1039–1052, 2015.

[85] F. Gini and M. Greco, "Covariance matrix estimation for CFAR detection in correlated heavy tailed clutter," *Signal Processing*, vol. 82, no. 12, pp. 1847–1859, 2002.

[86] S. M. Kay, *Fundamentals of Statistical Signal Processing, Vol. I: Estimation Theory.* Prentice Hall, 1993.

[87] Y. Chitour and F. Pascal, "Exact maximum likelihood estimates for SIRV covariance matrix: Existence and algorithm analysis," *IEEE Transactions on Signal Processing*, vol. 56, no. 10, pp. 4563–4573, 2008.

[88] I. S. Gradshteyn and I. M. Ryzhik, *Tables of Integrals, Series, and Products.* Academic press, 2000.

[89] A. K. Jain, *Fundamentals of Digital Image Processing.* Prentice-Hall, Inc., 1989.

[90] N. Bon, A. Khenchaf, and R. Garello, "GLRT subspace detection for range and Doppler distributed targets," *IEEE Transactions on Aaerospace and Electronic Systems*, vol. 44, no. 2, 2008.

[91] E. Ollila, D. E. Tyler, V. Koivunen, and H. V. Poor, "Complex elliptically symmetric distributions: survey, new results and applications," *IEEE Transactions on Signal Processing*, vol. 60, no. 11, pp. 5597–5625, 2012.

[92] F. Pascal, Y. Chitour, J.-P. Ovarlez, P. Forster, and P. Larzabal, "Covariance structure maximum-likelihood estimates in compound Gaussian noise: Existence and algorithm analysis," *IEEE Transactions on Signal Processing*, vol. 56, no. 1, pp. 34–48, 2008.

[93] I. S. Reed, J. D. Mallett, and L. E. Brennan, "Rapid convergence rate in adaptive arrays," *IEEE Transactions on Aerospace and Electronic Systems*, no. 6, pp. 853–863, 1974.

[94] K. Gerlach and M. J. Steiner, "Fast converging adaptive detection of Doppler-shifted, range-distributed targets," *IEEE Transactions on Signal Processing*, vol. 48, no. 9, pp. 2686–2690, 2000.

[95] T. F. Ayoub and A. R. Haimovich, "Modified GLRT signal detection algorithm," *IEEE Transactions on Aerospace and Electronic Systems*, vol. 36, no. 3, pp. 810–818, 2000.

[96] E. Conte, M. Lops, and G. Ricci, "Asymptotically optimum radar detection in compound-gaussian clutter," *IEEE Transactions on Aerospace and Electronic Systems*, vol. 31, no. 2, pp. 617–625, 1995.

[97] "PARSAX: S-band polarimetric Doppler radar," http://radar.ewi.tudelft.nl/ Facilities/parsax.php, 2019 (accessed January 17, 2019).

[98] O. A. Krasnov, L. P. Ligthart, Z. Li, G. Babur, Z. Wang, and F. van der Zwan, "PARSAX: High-resolution doppler-polarimetric FMCW radar with dual-orthogonal signals," in *Microwave Radar and Wireless Communications (MIKON), 2010 18th International Conference on.* IEEE, 2010, pp. 1–5.

[99] O. Krasnov, L. Ligthart, Z. Li, G. Babur, Z. Wang, and F. v. d. Zwan, "PARSAX: Waveform-agile polarimetric radar," *Slides from the workshop "Waveform-Agile Radar: Signals, Algorithms, and Systems" hold at EUMW 2010, Paris, unpublished.*

[100] J. V. Lambers and A. C. Sumner, *Explorations in Numerical Analysis.* World Scientific, 2017.
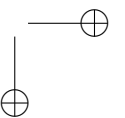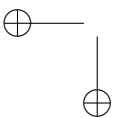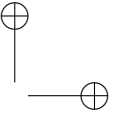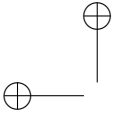
Acknowledgments

Although a PhD study aims at the advancement of professional and scientific skills, it always comes together with personal development. The people surrounding you during this long journey – from the first look at the scientific project description to the last corrections of this book – direct you on this way by fruitful discussions, crucial comments and small remarks. I am grateful to all of them for helping me in this long way.

First of all, I would like to thank my daily supervisor Prof.ir. François Le Chevalier for his continuous support over these years. I am very grateful to him for introducing me to this challenging topic of wideband radars, sharing his expertise and always providing me with appropriate advice and guidance. His enthusiasm about every single dB gain has been encouraging me to continue the research during all these years. I will miss our scientific discussions, which expanded far beyond the scope of this thesis — from the radar basics to the most advanced technologies, or from a small technical issue to the global role of the modern radars in the world.

Second, Im deeply indebted to my promoter Prof.dr. Alexander Yarovoy for the opportunity to perform, and, especially, for the occasion to finalize this research. His advice at the difficult stages of my research and his assistance in summarizing the results into this thesis are very appreciated. I would like to thank both François and Alexander for their "take your time" attitude, which gave me the freedom to make my own mistakes and discoveries. Their influence on my scientific and personal development over these years is difficult to overestimate.

I am grateful to my senior colleagues Dr.ir. Hans Driessen, Dr. Oleg Krasnov and Dr. Faruk Uysal for the fruitful scientific discussions and crucial comment on my research. I very much appreciate the help of Dr. Bert-Jan Kooij on translating the abstract of this thesis. Special thanks go Prof.dr. Stéphanie Bidon from ISAE-SUPAERO, Toulouse, France, for the insightful comments, which helped to improve the thesis. I would like to acknowledge the assistance of Fred van der Zwan and Etienne Goossens in collecting and processing experimental radar data. I also express my gratitude to Minke van der Put, Minaksie Ramsoekh and Esther de Klerk for their

About the author

Nikita Petrov was born in Gatchina, Russia on March 10, 1990. In 2012, he received a degree in Radio-Electronic Systems Engineering from "Baltic State Technical University "Voenmeh" named after D.F.Ustinov", Saint Petersburg, Russia.

In 2011-2012 he worked as an electronic engineer at the State Research Center "Elektropribor", Saint Petersburg, Russia. Then, in August 2012 he joined the Scientific Technical Centre "Leninetz", Saint Petersburg, Russia for the research on advanced signal processing for airborne radars.

From April 2013 he has been working on his PhD degree in the Microwave Sensing, Signals and Systems (MS3) group at Delft University of Technology. The subject of his research was the application of wideband high-resolution waveforms to modern surveillance radars.

At present, he stays with the same group and conducts the research on the advanced signal processing techniques for automotive radars. His main research interests include high-resolution radars, modern radar technologies, and radar signal processing.
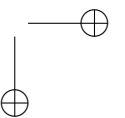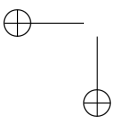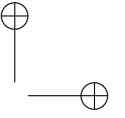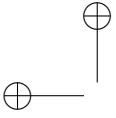
Author's publications

Journal Papers

1. N. Petrov, F. Le Chevalier, and A. G. Yarovoy, "Detection of range migrating targets in compound-Gaussian clutter," *IEEE Transactions on Aerospace and Electronic Systems*, vol. 54, no. 1, pp. 37—50, 2018.

2. F. Le Chevalier and N. Petrov, "Diversity considerations in wideband radar detection of migrating targets in clutter," *Science China Information Sciences*, vol. 62, no. 4, 2019.

3. F. Le Chevalier and N. Petrov, "Détection des cibles mobiles par radar large bande non-ambigu [Detection of moving targets with a wideband unambiguous radar]," *Revue de l'Electricite et de l'Electronique*, no. 5, 2017.

Conference Papers

4. N. Petrov, F. Le Chevalier, N. Bogdanović, and A. Yarovoy, "Range migrating target detection in correlated compound-Gaussian clutter," in *25th European Signal Processing Conference (EUSIPCO)*. IEEE, 2017, pp. 2216—2220 .

5. F. Le Chevalier and N. Petrov, "Benefits of space-time diversity for radar," in *Workshop "Geolocation and navigation in space and time"*, URSI, France, March 28-29, 2018, pp. 1-9, 2018.

6. N. Petrov, F. Le Chevalier, and A. Yarovoy, "Unambiguous detection of migrating targets with wideband radar in Gaussian clutter," in *CIE International Conference on Radar (RADAR)*. IEEE, 2016, pp. 1—5.

7. N. Petrov, F. Le Chevalier, and A. Yarovoy, "'Performance prediction of wideband unambiguous target detection in diffuse ground clutter," in *European Radar Conference (EuRAD)*. IEEE, 2016, pp. 97—100 .

8. N. Petrov and F. Le Chevalier, "Iterative adaptive approach for unambiguous wideband radar target detection," in *European Radar Conference (EuRAD)*. IEEE, 2015, pp. 45 — 48 .

9. N. Petrov and F. Le Chevalier, "Wideband spectrum estimators for unambiguous target detection," in *16th International Radar Symposium (IRS)*. IEEE, 2015, pp. 676—681 .

10. N. Petrov and F. Le Chevalier, "Fast implementation of iterative adaptive approach for wideband unambiguous radar detection," in *23rd European Signal Processing Conference (EUSIPCO)*. IEEE, 2015, pp. 1207—1211 .

11. N. Petrov and F. Le Chevalier, "Capon post-processing for wideband target detection," in *International Radar Conference*. IEEE, 2014, pp. 1–6.

12. N. Petrov, F. Le Chevalier, and A. Yarovoy, "Adaptive Detection of Range Migrating Target in non-Gaussian Clutter" accepted at *International Radar Conference (RADAR)*, 2019.